Two-Higgs-doublet model with soft *CP* violation confronting electric dipole moments and colliders

Kingman Cheung,[1,2,3,*] Adil Jueid,[3,†] Ying-nan Mao,[1,‡] and Stefano Moretti[4,§]

[1]*Physics Division, National Center for Theoretical Sciences, Hsinchu 300, Taiwan*
[2]*Department of Physics, National Tsing Hua University, Hsinchu 300, Taiwan*
[3]*Division of Quantum Phases and Devices, School of Physics, Konkuk University, Seoul 143-701, Republic of Korea*
[4]*School of Physics and Astronomy, University of Southampton, Southampton SO17 1BJ, United Kingdom*

(Received 29 April 2020; accepted 18 September 2020; published 23 October 2020)

We analyze *CP*-violating effects in both electric dipole moment (EDM) measurements and future analyses at the Large Hadron Collider (LHC) assuming a two-Higgs-doublet model (2HDM) with "soft" *CP* violation. Our analysis of EDMs and current LHC constraints shows that, in the case of Type II and Type III 2HDMs, an $\mathcal{O}(0.1)$ *CP*-violating phase in the Yukawa interaction between H_1 (the 125 GeV Higgs boson) and fermions is still allowed. For these scenarios, we study *CP*-violating effects in the neutron EDM and $t\bar{t}H_1$ production at the LHC. Our analysis shows that such an $\mathcal{O}(0.1)$ *CP*-violating phase can be easily confirmed or excluded by future neutron EDM tests, with LHC data providing a complementary cross-check.

DOI: 10.1103/PhysRevD.102.075029

I. INTRODUCTION

CP violation was first discovered in 1964 through the $K_L \to \pi\pi$ rare decay channel [1]. Later, more *CP*-violation effects were discovered in the *K*-, *B*-, and *D*-meson sectors [2,3], and all of the discovered effects are consistent with the explanation given by the Kobayashi-Maskawa (KM) mechanism [4]. However, the KM mechanism itself cannot generate a large enough matter-antimatter asymmetry in the Universe. Therefore, new *CP*-violation sources beyond the KM mechanism are needed to explain the latter [5–7].

Experimentally, all of the discovered effects of *CP* violation until now have appeared in flavor physics measurements, yet they can also be tested through other methods. These can generally be divided into two different categories: (a) indirect tests, which can merely probe the existence of *CP* violation but cannot confirm the source(s) behind it; (b) direct tests, which can directly lead us to the actual *CP*-violation interaction(s).

For indirect tests, there is a typical example that one most often uses: the electric dipole moment (EDM) measurements [8–13]. The reason is that the EDM effective interaction of a fermion is

$$\mathcal{L}_{\rm EDM} = -\frac{\rm i}{2} d_f \bar{f} \sigma^{\mu\nu} \gamma^5 f F_{\mu\nu}, \tag{1}$$

where d_f is the EDM of such a fermion f, which leads to P and CP violation simultaneously [9]. It is a pure quantum effect, i.e., it emerges at loop level and, in the Standard Model (SM), the electron and neutron EDMs are predicted to be extremely small [9],

$$|d_e^{\rm SM}| \sim 10^{-38}\ e\cdot{\rm cm}, \qquad |d_n^{\rm SM}| \sim 10^{-32}\ e\cdot{\rm cm}, \tag{2}$$

because they are generated at the four- or three-loop level, respectively. Thus, since the SM predictions for these are still far below the recent experimental limits [14–17]

$$|d_e| < 1.1\times 10^{-29}\ e\cdot{\rm cm}, \qquad |d_n| < 1.8\times 10^{-26}\ e\cdot{\rm cm}, \tag{3}$$

both given at the 90% confidence level (C.L.),[1] these EDMs provide a fertile ground to test the possibility of *CP* violation due to new physics. In fact, in some beyond-the-SM (BSM) scenarios the EDMs of the electron and

*cheung@phys.nthu.edu.tw
†adiljueid@konkuk.ac.kr
‡ynmao@cts.nthu.edu.tw
§s.moretti@soton.ac.uk

[1]An earlier result [15,16] is $|d_n| < 3.0\times 10^{-26}\ e\cdot{\rm cm}$, while a more recent measurement by the nEDM group [17] set the stricter constraint $|d_n| < 1.8\times 10^{-26}\ e\cdot{\rm cm}$, both at 90% C.L. At 95% C.L., the latest constraint is then $|d_n| < 2.2\times 10^{-26}\ e\cdot{\rm cm}$.

neutron can be generated already at the one- or two-loop level, and thus these constructs may already be strictly constrained or excluded. In measurements of d_e and d_n, however, even if we discover that either or both EDMs are far above the SM predictions, we cannot determine the exact interaction that constitutes such a CP violation.

For direct tests, there are several typical channels to test CP violation at colliders. For instance, measuring the final-state distributions from top pair [18–31] or τ pair [32–40] production enables one to test CP-violating effects entering the interactions of the fermions with one or more Higgs bosons. The discovery of the 125 GeV Higgs boson [41–43] made such experiments feasible. Indeed, if more (pseudo)scalar or new vector states are discovered, one could also try to measure the couplings among (old and new) scalars and vectors themselves to probe CP violation entirely from the bosonic sector [44–46]. At high-energy colliders, the discovery of some CP-violation effects could lead us directly to the CP-violating interaction(s), essentially because herein one can produce final states that can be studied at a differential level, thanks to the ability of the detectors to reconstruct their (at times, full) kinematics, which can then be mapped to both cross section and charge/spin asymmetry observables.

Theoretically, new CP violation can appear in many new physics models, such as those with an extended Higgs sector [47–52]. Among these, here we choose to deal with the well-known two-Higgs-doublet model (2HDM) [51], which we use as a prototypical source of CP violation entertaining both direct and indirect tests of it. In the 2HDM, another Higgs doublet brings four additional scalar degrees of freedom, two of which are neutral. Thus, there are a total of three neutral (pseudo)scalars. In the CP-conserving case, two of these are scalars and one is a pseudoscalar. For some parameter choices the pseudoscalar can mix with the scalar(s), and then CP violation happens. Specifically, the 2HDM with a Z_2 symmetry is used here in order to avoid large flavor-changing neutral currents (FCNCs), yet such a symmetry must be softly broken if one wants CP violation to arise in this scenario [51].

The CP-violation effects in the 2HDM were widely studied in recent years. People carefully calculated the EDMs in the 2HDM and discussed their further phenomenology [53–66]. Usually, the domain contributions come from the two-loop Barr-Zee-type diagrams [53], and complex Yukawa interactions provide the CP-violation sources. In particular, for the electron EDM, a cancellation between different contributions may appear in some region [67–74], and thus a relative large CP phase $\sim\mathcal{O}(0.1)$ in the Yukawa interactions will still be allowed. Such a CP phase is helpful to explain the matter-antimatter asymmetry in the Universe [69,74–77]. However, such cancellation usually does not appear in the same region for the neutron EDM, and thus future measurements of the neutron EDM will be helpful for testing the CP phases, which will be discussed in detail below. The collider studies for CP violation were usually performed model independently, but the results can be simply applied for the 2HDM. We will therefore study the effects of such a CP-violating 2HDM on the electron and neutron EDMs as well as processes entering the Large Hadron Collider (LHC), specifically those involving the production of a top-antitop pair in association with the 125 GeV Higgs boson.

This paper is organized as follows. In Sec. II we review the construction of the 2HDM with so-called "soft" CP violation with the four standard types of Yukawa interactions. Then, in Sec. III we discuss the current constraints from the electron and neutron EDMs, show the reason why we eventually choose to only phenomenologically pursue the Type II and Type III 2HDMs for our collider analysis, and discuss the importance of future neutron EDM tests. In Sec. IV we discuss the current constraints from collider experiments on these two realizations of a 2HDM. In Sec. V we discuss LHC phenomenology studies on CP-violation effects in the $t\bar{t}H_1$ associated production process. Finally, we summarize and conclude in Sec. VI. There are also several appendices which we use to collect technical details.

II. MODEL SETUP

In this section we briefly review the 2HDM with a softly broken Z_2 symmetry and how CP violation arises in such a model. We mainly follow the conventions in Refs. [78–80]. The Lagrangian of the scalar sector can be written as

$$\mathcal{L} = \sum_{i=1,2} (D_\mu \phi_i)^\dagger (D^\mu \phi_i) - V(\phi_1, \phi_2). \tag{4}$$

Under a Z_2 transformation, we can have $\phi_1 \to \phi_1$, $\phi_2 \to -\phi_2$, and thus, in the scalar potential, all terms must contain even numbers of ϕ_i. However, if the Z_2 symmetry is softly broken, a term $\propto \phi_1^\dagger \phi_2$ is allowed, and thus the scalar potential becomes

$$\begin{aligned} V(\phi_1, \phi_2) = &-\frac{1}{2}[m_1^2 \phi_1^\dagger \phi_1 + m_2^2 \phi_2^\dagger \phi_2 + (m_{12}^2 \phi_1^\dagger \phi_2 + \text{H.c.})] \\ &+ \frac{1}{2}[\lambda_1 (\phi_1^\dagger \phi_1)^2 + \lambda_2 (\phi_2^\dagger \phi_2)^2] \\ &+ \lambda_3 (\phi_1^\dagger \phi_1)(\phi_2^\dagger \phi_2) + \lambda_4 (\phi_1^\dagger \phi_2)(\phi_2^\dagger \phi_1) \\ &+ \left[\frac{\lambda_5}{2}(\phi_1^\dagger \phi_2)^2 + \text{H.c.}\right]. \end{aligned} \tag{5}$$

Here $\phi_{1,2}$ are SU(2) scalar doublets, which are defined as

$$\phi_1 \equiv \begin{pmatrix} \varphi_1^+ \\ \frac{v_1 + \eta_1 + i\chi_1}{\sqrt{2}} \end{pmatrix}, \qquad \phi_2 \equiv \begin{pmatrix} \varphi_2^+ \\ \frac{v_2 + \eta_2 + i\chi_2}{\sqrt{2}} \end{pmatrix}. \tag{6}$$

The parameters $m_{1,2}^2$ and $\lambda_{1,2,3,4}$ must be real, while m_{12}^2 and λ_5 can be complex. Further, $v_{1,2}$ are the vacuum expectation values of the scalar doublets with the relation $\sqrt{|v_1|^2+|v_2|^2}=246$ GeV. The ratio v_2/v_1 may also be complex,[2] and we define $t_\beta \equiv |v_2/v_1|$ as usual.[3]

As shown in Ref. [51], *CP* violation in the scalar sector requires a nonzero m_{12}^2. For the three possible complex parameters m_{12}^2, λ_5, and v_2/v_1, we can always perform a field rotation to ensure that at least one of them is real. In this paper, we choose v_2/v_1 to be real (thus, both $v_{1,2}$ are real) like in Refs. [78–80], and we have the relation

$$\mathrm{Im}(m_{12}^2) = v_1 v_2 \mathrm{Im}(\lambda_5) \tag{7}$$

following the minimization conditions for the scalar potential. If $\mathrm{Im}(m_{12}^2)$ and $\mathrm{Im}(\lambda_5)$ are nonzero, *CP* violation occurs in the scalar sector.

We diagonalize the charged components as

$$\begin{pmatrix} G^+ \\ H^+ \end{pmatrix} = \begin{pmatrix} c_\beta & s_\beta \\ -s_\beta & c_\beta \end{pmatrix} \begin{pmatrix} \varphi_1^+ \\ \varphi_2^+ \end{pmatrix}, \tag{8}$$

where H^+ is the charged Higgs boson and G^+ is the charged Goldstone. Similarly, for the *CP*-odd neutral components,

$$\begin{pmatrix} G^0 \\ A \end{pmatrix} = \begin{pmatrix} c_\beta & s_\beta \\ -s_\beta & c_\beta \end{pmatrix} \begin{pmatrix} \chi_1 \\ \chi_2 \end{pmatrix}, \tag{9}$$

where A is the physical *CP*-odd degree of freedom and G^0 is the neutral Goldstone. In the *CP*-conserved case, A is a pseudoscalar boson, while in the *CP*-violating case A has further mixing with the *CP*-even degrees of freedom as

$$\begin{pmatrix} H_1 \\ H_2 \\ H_3 \end{pmatrix} = R \begin{pmatrix} \eta_1 \\ \eta_2 \\ A \end{pmatrix}. \tag{10}$$

Here $H_{1,2,3}$ are mass eigenstates and we choose H_1 as the lightest one with mass $m_1 = 125$ GeV, so that it is the observed SM-like Higgs boson. The rotation matrix R can be parametrized as

$$R = \begin{pmatrix} 1 & & \\ & c_{\alpha_3} & s_{\alpha_3} \\ & -s_{\alpha_3} & c_{\alpha_3} \end{pmatrix} \begin{pmatrix} c_{\alpha_2} & & s_{\alpha_2} \\ & 1 & \\ -s_{\alpha_2} & & c_{\alpha_2} \end{pmatrix} \times \begin{pmatrix} c_{\beta+\alpha_1} & s_{\beta+\alpha_1} & \\ -s_{\beta+\alpha_1} & c_{\beta+\alpha_1} & \\ & & 1 \end{pmatrix}. \tag{11}$$

When $\alpha_{1,2} \to 0$, H_1 becomes the SM Higgs boson. If $m_{1,2}$, $\alpha_{1,2,3}$, and β are known, m_3 can be expressed as [62,65,80]

$$m_3^2 = \frac{(m_1^2 - m_2^2 s_{\alpha_3}^2) c_{2\beta+\alpha_1}/c_{\alpha_3}^2 - m_2^2 s_{2\beta+\alpha_1} t_{\alpha_3}}{c_{2\beta+\alpha_1} s_{\alpha_2} - s_{2\beta+\alpha_1} t_{\alpha_3}}. \tag{12}$$

In the mass eigenstates, the couplings between neutral scalars and gauge bosons can be parametrized via

$$\mathcal{L} \supset \sum_{1\le i\le 3} c_{V,i} H_i \left(\frac{2m_W^2}{v} W^{+,\mu} W_\mu^- + \frac{m_Z^2}{v} Z^\mu Z_\mu \right) + \sum_{i=1}^{3} \frac{c_{ij} g}{2 c_{\theta_W}} Z_\mu (H_i \partial^\mu H_j - H_j \partial^\mu H_i). \tag{13}$$

The coefficients are then

$$c_{V,1} = c_{23} = c_{\alpha_1} c_{\alpha_2}, \tag{14}$$

$$c_{V,2} = -c_{13} = -c_{\alpha_3} s_{\alpha_1} - c_{\alpha_1} s_{\alpha_2} s_{\alpha_3}, \tag{15}$$

$$c_{V,3} = c_{12} = s_{\alpha_1} s_{\alpha_3} - c_{\alpha_1} c_{\alpha_3} s_{\alpha_2}. \tag{16}$$

Next we turn to the Yukawa sector. Due to the Z_2 symmetry, a fermion bilinear can couple to only one scalar doublet, with the form $\bar{Q}_L \phi_i D_R$, $\bar{Q}_L \tilde{\phi}_i U_R$, or $\bar{L}_L \phi_i \ell_R$, and thus it is helpful to avoid the FCNC problem [51]. Here $\tilde{\phi}_i \equiv i\sigma_2 \phi_i^*$ and left-handed fermion doublets are defined as $Q_{i,L} \equiv (U_i, D_i)_L^T$ and $L_L \equiv (\nu_i, \ell_i)_L^T$, for the ith generation. Since the scalar potential contains a $\phi_1 \leftrightarrow \phi_2$ exchange symmetry, we can set the convention in which $\bar{Q}_L U_R$ always couples to ϕ_2 so that there are four standard types of Yukawa couplings [51,80]:

$$\mathcal{L} \supset \begin{cases} -Y_U \bar{Q}_L \tilde{\phi}_2 U_R - Y_D \bar{Q}_L \phi_2 D_R - Y_\ell \bar{L}_L \phi_2 \ell_R + \mathrm{H.c.} & \text{(Type I)}, \\ -Y_U \bar{Q}_L \tilde{\phi}_2 U_R - Y_D \bar{Q}_L \phi_1 D_R - Y_\ell \bar{L}_L \phi_1 \ell_R + \mathrm{H.c.} & \text{(Type II)}, \\ -Y_U \bar{Q}_L \tilde{\phi}_2 U_R - Y_D \bar{Q}_L \phi_2 D_R - Y_\ell \bar{L}_L \phi_1 \ell_R + \mathrm{H.c.} & \text{(Type III)}, \\ -Y_U \bar{Q}_L \tilde{\phi}_2 U_R - Y_D \bar{Q}_L \phi_1 D_R - Y_\ell \bar{L}_L \phi_2 \ell_R + \mathrm{H.c.} & \text{(Type IV)}. \end{cases} \tag{17}$$

[2]We can always fix v_1 to be real through a gauge transformation, and v_2 may be complex at the same time.

[3]In this paper, we denote $s_\alpha \equiv \sin\alpha$, $c_\alpha \equiv \cos\alpha$, and $t_\alpha \equiv \tan\alpha$.

The fermion mass matrix is $M_f = Y_f v c_\beta/\sqrt{2}$ if the fermion couples to ϕ_1 and $M_f = Y_f v s_\beta/\sqrt{2}$ if it couples to ϕ_2. We parametrize the Yukawa couplings of mass eigenstates as

$$\mathcal{L} \supset -\sum_{i,f} \frac{m_f}{v}(c_{f,i} H_i \bar{f}_L f_R + \text{H.c.}). \tag{18}$$

For CP-violating models, $c_{f,i}$ are complex numbers and we list them in Appendix A for all four types of Yukawa interactions. In all of these models, $\text{Im}(c_{f,1}) \propto s_{\alpha_2}$, and thus α_2 is an important mixing angle that measures the CP-violating phase in the Yukawa couplings of H_1.

III. CURRENT EDM CONSTRAINTS AND FUTURE TESTS

In this section, we analyze the EDM constraints of the electron and neutron for the four types of 2HDMs in some detail. The $b \to s\gamma$ decay requires the charged Higgs mass to be $m_{H^\pm} \gtrsim 600$ GeV for all four types of Yukawa couplings when $t_\beta \sim 1$ [81–84]. If t_β gets larger, the constraints will become weaker for Type I and III Yukawa couplings. The oblique parameters [85,86] will then favor the case $m_{H_{2,3}} \gtrsim 500$ GeV [87–90].[4] With such choices for the scalar masses, the vacuum stability condition favors $\mu^2 \equiv \text{Re}(m_{12}^2)/s_{2\beta} \lesssim (450\,\text{GeV})^2$ [79]. Notice that μ^2 will modify the charged Higgs couplings a little, but it is not numerically important to the EDM calculation, so we fix it at $\mu^2 = (450\ \text{GeV})^2$ in the rest of this work. More discussions about the scalar couplings can be found in Appendix B.

An electron EDM measurement places a very strict constraint on the complex Yukawa couplings in most models. As a rough estimation, if we consider CP violation only in the 125 GeV Higgs interaction with the top quark, the typical constraint is $\arg(c_{t,1}) \lesssim 10^{-3}$ [73]. However, some models (including the 2HDM) allow for the accidental cancellation among various contributions, so that larger $\arg(c_{t,1})$ may still be allowed [67–74]. In such cases, neutron EDM constraints will also become important, as shown in the analysis later in this section.

A. Electron EDM

A recent electron EDM measurement was performed using the ThO molecule [14]. The exact constrained quantity is

$$|d_e^{\text{eff}}| \equiv |d_e + kC| < 1.1 \times 10^{-29}\ e \cdot \text{cm}. \tag{19}$$

The second term measures the contribution from CP-violating electron-nucleon interactions via

$$\mathcal{L} \supset C(\bar{N}N)(\bar{e}i\gamma^5 e), \tag{20}$$

where the coefficient C is almost the same for the proton and neutron. Here, $k \approx 1.6 \times 10^{-15}$ GeV^2 $e \cdot$ cm, which was obtained for ThO [91,92]; however, for most other materials with heavy atoms, this quantity appears to be of the same order [9,93]. The contribution from electron-nucleon interactions is usually subleading, though it can also become important.

The typical Feynman diagrams contributing to the electron EDM in the 2HDM are listed in Fig. 1. Figures 1(a)–1(e) are Barr-Zee-type diagrams [53] with the top quark t, $W^\pm$ boson, or charged Higgs $H^\pm$ in the upper loop, while Figs. 1(f) and 1(g) are non-Barr-Zee-type diagrams. These seven diagrams contribute directly to d_e. Figure 1(h) shows the contribution through the electron-quark interaction, while Fig. 1(i) shows the contribution through the electron-gluon interaction. The contributions can be divided into eight parts, as summarized in Table I.

The analytical expressions in the Feynman–'t Hooft gauge are listed below. For simplicity, we denote

$$\delta_0 \equiv \frac{\sqrt{2} m_e G_F \alpha_{\text{em}}}{(4\pi)^3} = 3.1 \times 10^{-14}\ \text{GeV} = 6.1 \times 10^{-28}\ e \cdot \text{cm} \tag{21}$$

from now on. For the fermion-loop contribution in which the top quark is dominant, we have [53–59,63,66,67]

$$\frac{d_e^{t,\gamma,H_i}}{e} = \frac{32}{3}\delta_0 [f(z_{tH_i})\text{Re}(c_{t,i})\text{Im}(c_{e,i}) + g(z_{tH_i})\text{Re}(c_{e,i})\text{Im}(c_{t,i})], \tag{22}$$

$$\frac{d_e^{t,Z,H_i}}{e} = -\frac{(1-\frac{8s_{\theta_W}^2}{3})(-1+4s_{\theta_W}^2)}{s_{\theta_W}^2 c_{\theta_W}^2}\delta_0 \times [F(z_{tH_i}, z_{tZ})\text{Re}(c_{t,i})\text{Im}(c_{e,i}) + G(z_{tH_i}, z_{tZ})\text{Re}(c_{e,i})\text{Im}(c_{t,i})]. \tag{23}$$

Here $z_{ij} \equiv m_i^2/m_j^2$ and θ_W is the weak mixing angle with $s_{\theta_W}^2 = 0.23$. The loop integration functions here and below are all listed in Appendix C. For the electron EDM calculation, the Z-mediated contribution is accidentally suppressed by $-1/2 + 2s_{\theta_W}^2 \sim -0.04$. For the W-loop contribution, we have [53–55,57–59,63,66]

$$\frac{d_e^{W,\gamma,H_i}}{e} = -\delta_0 \left[12 f(z_{WH_i}) + 23 g(z_{WH_i}) + 3h(z_{WH_i}) + \frac{2}{z_{WH_i}}(f(z_{WH_i}) - g(z_{WH_i}))\right] c_{V,i}\text{Im}(c_{e,i}), \tag{24}$$

[4]When H_1 is SM-like, the oblique parameter constraints are sensitive mainly to the mass splitting between the charged and neutral scalars. They are not sensitive to the mixing parameters in Eq. (11).

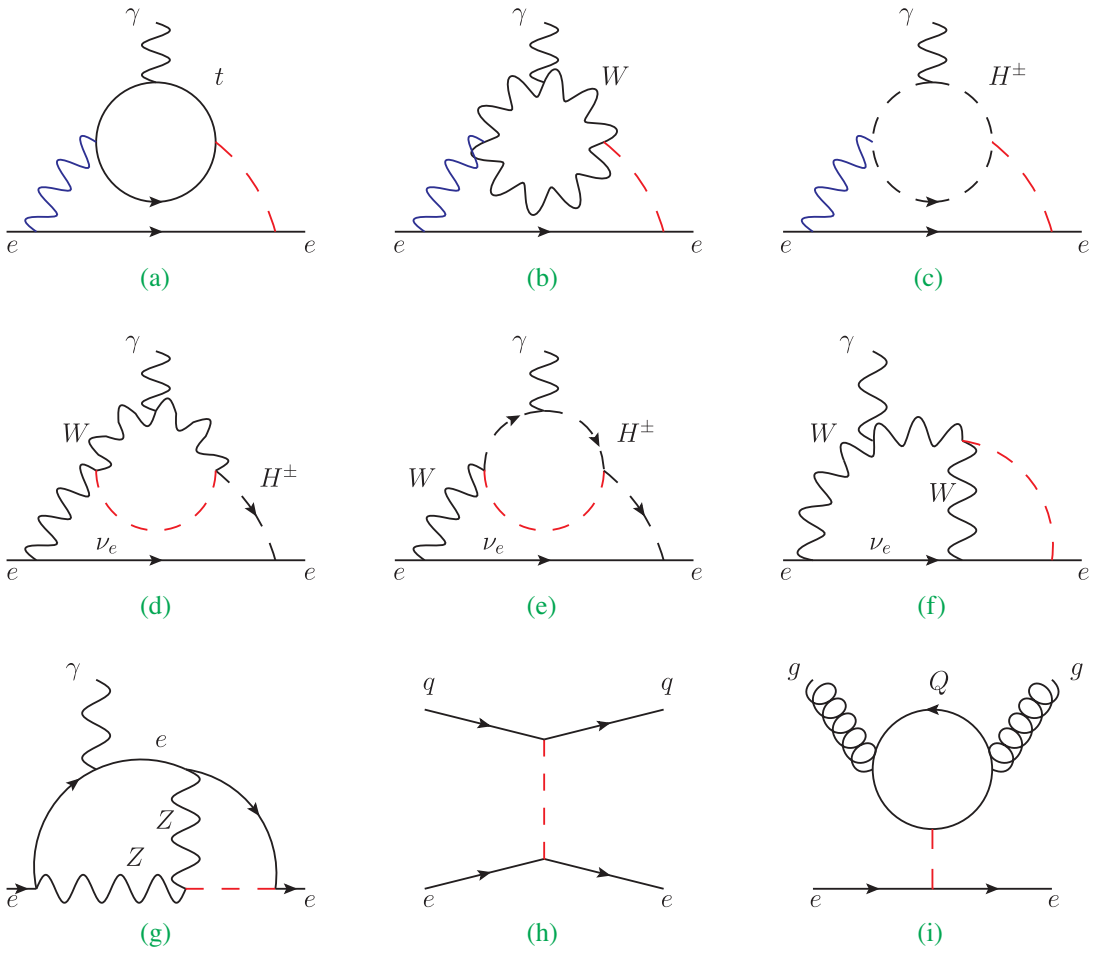

FIG. 1. Typical Feynman diagrams contributing to the electron EDM in the 2HDM. The blue lines can be γ or Z, while red lines are neutral Higgses $H_{1,2,3}$. Diagrams (a)–(g) will contribute to d_e directly, while diagrams (h)–(i) will contribute to the electron-nucleon interaction term.

TABLE I. Different contributions to the electron EDM and the corresponding Feynman diagrams.

	Diagram	Contribution	*CP*-violation vertex
$d_e^{t,\gamma/Z,H_i}$	(a)	Fermion (top) loop	$H_i\bar{e}e$, $H_i\bar{t}t$
$d_e^{W,\gamma/Z,H_i}$	(b)	W loop	$H_i\bar{e}e$
$d_e^{H^\pm,\gamma/Z,H_i}$	(c)	Charged Higgs $H^\pm$ loop	$H_i\bar{e}e$
$d_e^{W,H^\pm,H_i}$	(d) and (e)	$W^\pm - H^\pm$ loop	$H^\pm W^\mp H_i$
δd_e^W	(f)	non-Barr-Zee W loop	$H_i\bar{e}e$
δd_e^Z	(g)	non-Barr-Zee Z loop	$H_i\bar{e}e$
$d_{e,q,i}^{\text{int}}$	(h)	Electron-quark interaction	$H_i\bar{e}e$
$d_{e,g,i}^{\text{int}}$	(i)	Electron-gluon interaction	$H_i\bar{e}e$

$$\frac{d_e^{W,Z,H_i}}{e} = \frac{-1+4s_{\theta_W}^2}{s_{\theta_W}^2}\delta_0\left[\frac{5-t_{\theta_W}^2}{2}F(z_{WH_i},c_{\theta_W}^2) + \frac{7-3t_{\theta_W}^2}{2}G(z_{WH_i},c_{\theta_W}^2) + \frac{3}{4}h(z_{WH_i}) + \frac{3}{4}g(z_{WH_i}) + \frac{1-t_{\theta_W}^2}{4z_{WH_i}}(F(z_{WH_i},c_{\theta_W}^2) - G(z_{WH_i},c_{\theta_W}^2))\right] \times c_{V,i}\text{Im}(c_{e,i}). \quad (25)$$

This contribution will cross zero around $m_i \sim 500$ GeV because of the cancellation between W and Goldstone contributions and, in the heavy-m_i limit, the pure Goldstone diagram has the behavior $\sim \ln(m_i^2/m_W^2)$. The charged-Higgs-loop contributions are [57]

$$\frac{d_e^{H^\pm,\gamma,H_i}}{e} = -\left(\frac{2\delta_0 v^2}{m_\pm^2}\right)[f(z_{\pm,i}) - g(z_{\pm,i})]c_{\pm,i}\mathrm{Im}(c_{e,i}), \quad (26)$$

$$\frac{d_e^{H^\pm,Z,H_i}}{e} = \frac{-1+4s_{\theta_W}^2}{s_{2\theta_W}t_{2\theta_W}}\left(\frac{2\delta_0 v^2}{m_\pm^2}\right) \times [F(z_{\pm,i}, z_{\pm,Z}) - G(z_{\pm,i}, z_{\pm,Z})]c_{\pm,i}\mathrm{Im}(c_{e,i}). \quad (27)$$

Hereafter, "±" is used to denote the charged Higgs boson, while $c_{\pm,i}$ is the coupling constant between the charged and neutral scalars entering via $\mathcal{L} \supset -c_{\pm,i} v H_i H^+ H^-$. The $W^\pm - H^\pm$-associated loop yields [57]

$$\frac{d_e^{W,H^\pm,H_i}}{e} = -\frac{\delta_0}{2s_{\theta_W}^2}\left[\frac{H_i^a(z_{WH_i}) - H_i^a(z_{\pm,i})}{z_{\pm,W}-1}c_{V,i} - \frac{H_i^b(z_{WH_i}) - H_i^b(z_{\pm,i})}{z_{\pm,W}-1}c_{\pm,i}\right]\mathrm{Im}(c_{e,i}). \quad (28)$$

The first term corresponds to Fig. 1(d), while the second term corresponds to Fig. 1(e). The non-Barr-Zee-type diagrams give [55,63][5]

$$\frac{d_e^{W,H_i}}{e} = -\frac{\delta_0}{s_{\theta_W}^2}(D_{W,i}^a + D_{W,i}^b + D_{W,i}^c + D_{W,i}^d + D_{W,i}^e) \times c_{V,i}\mathrm{Im}(c_{e,i}), \quad (29)$$

$$\frac{d_e^{Z,H_i}}{e} = -4\delta_0 t_{\theta_W}^2(D_{Z,i}^a + D_{Z,i}^b + D_{Z,i}^c)c_{V,i}\mathrm{Im}(c_{e,i}). \quad (30)$$

The analytical expressions are too lengthy to present here, so we list all of them in Appendix C. One-loop contributions to d_e are highly suppressed by m_e^3 and thus we ignore them [70,94]. The interaction-induced effective EDM terms are [92,95–97]

$$d_{e,q,i}^{\mathrm{int}} = \frac{\sqrt{2}m_e G_F k}{m_i^2}\mathrm{Im}(c_{e,i})[\mathrm{Re}(c_{u,i})\langle m_u\bar{u}u\rangle + \mathrm{Re}(c_{d,i})(\langle m_d\bar{d}d\rangle + \langle m_s\bar{s}s\rangle)], \quad (31)$$

$$d_{e,g,i}^{\mathrm{int}} = -\frac{\sqrt{2}m_e G_F k}{3m_i^2}\mathrm{Im}(c_{e,i})[2\mathrm{Re}(c_{u,i}) + \mathrm{Re}(c_{d,i})] \times \left\langle\frac{\alpha_s}{4\pi}G_{\mu\nu}G^{\mu\nu}\right\rangle. \quad (32)$$

[5]We have checked the results in Refs. [55] and [63]. In the heavy-m_i limit, the loop functions should be logarithm enhanced as in Ref. [55] (just like the pure Goldstone contribution in Ref. [54]). However, the results in Ref. [63] have improper power enhancement, and thus this behavior cannot be physical. So we used the result from Ref. [55] for validation.

TABLE II. Nucleon matrix elements in the three-flavor scheme at the hadron scale ∼1 GeV. The lattice calculations of quark matrix elements are a bit different from different groups, as summarized in Ref. [103], and the results in this table are quoted from Ref. [101] which are close to the averaged values. The gluon matrix element was derived based on Ref. [98].

$\langle m_u\bar{u}u\rangle$	$\langle m_d\bar{d}d\rangle$	$\langle m_s\bar{s}s\rangle$	$\langle\frac{\alpha_s}{4\pi}G_{\mu\nu}G^{\mu\nu}\rangle$
14.5 MeV	31.4 MeV	40.2 MeV	−183 MeV

The nucleon matrix elements $\langle\mathcal{O}\rangle \equiv \langle N|\mathcal{O}|N\rangle$ and their values are similar for the proton and neutron. Thus, we choose the average values of the proton and neutron considering three active quarks (u, d, s) at the hadron scale ∼1 GeV [97–103], as listed in Table II. Summing all parts together, the effective electron EDM is

$$\begin{aligned} d_e^{\mathrm{eff}} &= d_e + d_e^{\mathrm{int}} \\ &= d_e^{t,\gamma,H_i} + d_e^{t,Z,H_i} + d_e^{W,\gamma,H_i} + d_e^{W,Z,H_i} + d_e^{H^\pm,\gamma,H_i} \\ &\quad + d_e^{H^\pm,Z,H_i} + d_e^{W,H^\pm,H_i} + \delta d_e^W + \delta d_e^Z + d_{e,q,i}^{\mathrm{int}} + d_{e,g,i}^{\mathrm{int}}. \end{aligned} \quad (33)$$

For each part above, $d_e^j \propto m_e$ and thus it is suppressed by the small electron mass. We can extract $C_e^j \equiv d_e^j/(-m_e)$, which is independent of the fermion mass. This coefficient is not useful in the electron EDM calculation, but it will be helpful in order to map the corresponding part into the quark EDM, which is important in the neutron EDM calculation below.

B. Neutron EDM

The neutron EDM calculation is more complex as it involves more contributions and QCD effects. As shown in Fig. 2, there are three types of operators contributing to the neutron EDM: the quark EDM operator $\mathcal{O}_q$, quark color EDM (CEDM) operator $\tilde{\mathcal{O}}_q$, and Weinberg operator $\mathcal{O}_g$.[6] They are chosen as follows [9,58]:

$$\mathcal{O}_q = -\frac{\mathrm{i}}{2}eQ_q m_q\bar{q}\sigma^{\mu\nu}\gamma_5 q F_{\mu\nu}, \quad (34)$$

$$\tilde{\mathcal{O}}_q = -\frac{\mathrm{i}}{2}g_s m_q\bar{q}\sigma^{\mu\nu}t^a\gamma_5 q G_{\mu\nu}^a, \quad (35)$$

$$\mathcal{O}_g = -\frac{1}{3}g_s f^{abc}G_{\mu\rho}^a G_\nu^{b,\rho}\tilde{G}^{c,\mu\nu}, \quad (36)$$

[6]In the 2HDM with Z_2 symmetry there is no CP violation entering the $tbH^\pm$ vertex, and thus we do not need to consider the diagram with a charged Higgs boson inside the loop for the Weinberg operator [56].

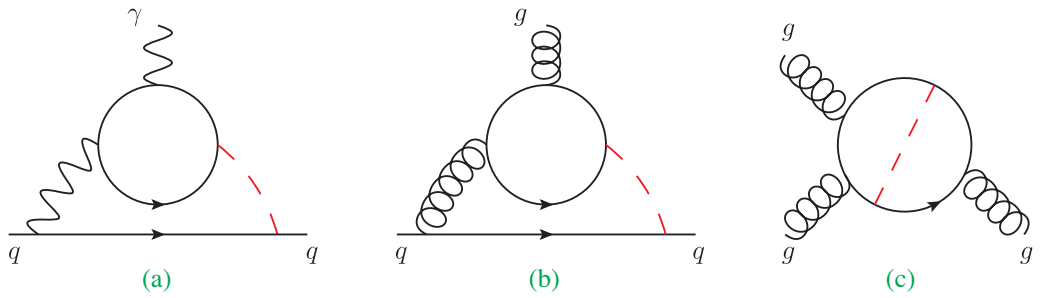

FIG. 2. Various contributions to the neutron EDM: quark EDM, quark CEDM, and Weinberg operator.

where g_s is the QCD coupling constant, t^a is a generator of the QCD group, and f^{abc} denotes the QCD structure constant. At a scale μ,

$$\mathcal{L} \supset \sum_{q=u,d} (C_q(\mu)\mathcal{O}_q(\mu) + \tilde{C}_q(\mu)\tilde{\mathcal{O}}_q(\mu)) + C_g(\mu)\mathcal{O}_g(\mu) \tag{37}$$

and

$$d_q(\mu)/e \equiv Q_q m_q(\mu) C_q(\mu), \qquad \tilde{d}_q(\mu) \equiv m_q(\mu)\tilde{C}_q(\mu). \tag{38}$$

For convenience we also redefine $w(\mu) \equiv g_s(\mu)C_g(\mu)$. Notice that these EDMs should first be calculated at the weak scale $\mu_W \sim m_t$.

The calculation methods of C_u and C_d are the same as those for d_e through Figs. 1(a)–1(g). For the quark EDM, we perform the calculation at the weak scale $\mu_W \approx m_t$ and list the results of the C_q^j evaluation [57] as follows:

$$(C_q^{t/W/H^\pm,\gamma,H_i}, \quad \delta C_q^Z) = (\bar{C}_e^{t/W/H^\pm,\gamma,H_i}, \qquad \delta\bar{C}_e^Z), \tag{39}$$

$$C_d^{t/W/H^\pm,Z,H_i} = \frac{-\frac{1}{2} + \frac{2s^2_{\theta_W}}{3}}{-\frac{1}{2} + 2s^2_{\theta_W}} \cdot \frac{-1}{Q_d} \bar{C}_e^{t/W/H^\pm,Z,H_i}, \tag{40}$$

$$C_u^{t/W/H^\pm,Z,H_i} = \frac{\frac{1}{2} - \frac{4s^2_{\theta_W}}{3}}{-\frac{1}{2} + 2s^2_{\theta_W}} \cdot \frac{-1}{Q_u} \bar{C}_e^{t/W/H^\pm,Z,H_i}, \tag{41}$$

$$(C_u^{W,H^\pm,H_i}, \quad \delta C_u^W) = (\frac{1}{Q_u}\bar{C}_e^{W,H^\pm,H_i}, \quad \frac{1}{Q_u}\delta\bar{C}_e^W), \tag{42}$$

$$(C_d^{W,H^\pm,H_i}, \quad \delta C_d^W) = (\frac{-1}{Q_d}\bar{C}_e^{W,H^\pm,H_i}, \quad \frac{-1}{Q_d}\delta\bar{C}_e^W). \tag{43}$$

Here, each $\bar{C}_e^j$ means C_e^j with the replacement $c_{e,i} \to c_{q,i}$ in the Yukawa couplings. The contributions including the Z boson in the Bar-Zee diagram become important in the quark EDM calculation, because there is no accidental suppression like that in the electron EDM calculation. For the CEDM terms, only Barr-Zee diagrams with a top loop contribute. The result at the weak scale $\mu_W \sim m_t$ is then [57,58]

$$\tilde{C}_q(\mu_W) = -\frac{2\sqrt{2}\alpha_s(\mu_W)G_F}{(4\pi)^3}\sum_{i=1}^{3}[f(z_{tH_i})\mathrm{Re}(c_{U,i})\mathrm{Im}(c_{q,i}) + g(z_{tH_i})\mathrm{Re}(c_{q,i})\mathrm{Im}(c_{U,i})]. \tag{44}$$

The coefficient of the Weinberg operator at the weak scale is [9,58]

$$C_g(\mu_W) = \frac{\sqrt{2}\alpha_s(\mu_W)G_F}{4(4\pi)^3}\sum_{i=1}^{3} W(z_{tH_i})\mathrm{Re}(c_{U,i})\mathrm{Im}(c_{U,i}), \tag{45}$$

and the loop integration $W(z)$ is listed in Appendix C.

To calculate the EDM of the neutron, we must consider the renormalization group equation (RGE) running effects to evolve these to the hadron scale $\mu_H \sim 1$ GeV. The one-loop running gives [58,104–107]

$$\begin{pmatrix} C_q(\mu_H) \\ \tilde{C}_q(\mu_H) \\ C_g(\mu_H) \end{pmatrix} = \begin{pmatrix} 0.42 & -0.38 & -0.07 \\ & 0.47 & 0.15 \\ & & 0.20 \end{pmatrix} \begin{pmatrix} C_q(\mu_W) \\ \tilde{C}_q(\mu_W) \\ C_g(\mu_W) \end{pmatrix}. \tag{46}$$

There is no quark-mass dependence in C_q or $\tilde{C}_q$ and the evolution of C_g is equivalent to $w(\mu_H) = 0.41w(\mu_W)$. According to Eq. (38), we only need the quark mass parameters at $\mu_H \sim 1$ GeV in the final calculation. The one-loop running mass effect is [2]

$$m_q(1\ \mathrm{GeV})/m_q(2\ \mathrm{GeV}) = 1.38 \tag{47}$$

and, with the lattice results at 2 GeV [2,108,109], we have

$$m_u(1\ \mathrm{GeV}) \simeq 3.0\ \mathrm{MeV}, \qquad m_d(1\ \mathrm{GeV}) \simeq 6.5\ \mathrm{MeV}. \tag{48}$$

The hadron scale estimation was performed based on QCD sum rules [9,58,110–112],[7]

$$\frac{d_n}{e} \simeq (22\ \mathrm{MeV})w(\mu_H) + 0.65\frac{d_d(\mu_H)}{e} - 0.16\frac{d_u(\mu_H)}{e} + 0.48\tilde{d}_d(\mu_H) + 0.24\tilde{d}_u(\mu_H), \quad (49)$$

with an uncertainty of about 50%. The light-quark condensation is chosen as $\langle\bar{q}q\rangle(1\,\mathrm{GeV}) = -(254\,\mathrm{MeV})^3$ [114], which is a bit larger than that from Refs. [9,110].[8] Combining all of the results above, we have

$$\frac{d_n}{e} = m_d(\mu_H)(0.27Q_dC_d(\mu_W) + 0.31\tilde{C}_d(\mu_W)) + m_u(\mu_H)(-0.07Q_uC_u(\mu_W) + 0.16\tilde{C}_u(\mu_W)) + (9.6\,\mathrm{MeV})w(\mu_W). \quad (50)$$

C. Numerical analysis for the 2HDMs

In this subsection we analyze the 2HDM with soft *CP* violation, including all four types of Yukawa interactions. For the electron EDM, the Type I and IV models give the same results, and the Type II and III models give the same results.[9] In the calculation of the electron EDM, the diagrams in Figs. 1(a) and 1(b) usually contribute dominantly.

For Type I and IV models, numerical results show that there is no cancellation among various contributions to the electron EDM, and thus the *CP*-violating phase is strictly constrained. The reason is that in these two models, both $\sum_i(d_e^{t,\gamma/Z,H_i})$ and $\sum_i(d_e^{W,\gamma/Z,H_i})$ have the behavior $\propto -s_{2\alpha_2}/t_\beta$, and thus d_e cannot get close to zero when keeping the *CP*-violation phases. This behavior is consistent with the results in which only the contribution from H_1 is considered [73], because in most cases the H_1 contribution is dominant compared with the heavy scalars if t_β is not too large, such as $\lesssim$10.

We take $m_{2,3} \sim 500$ GeV and $m_\pm \sim 600$ GeV as a benchmark point and find

$$d_e^{\mathrm{I,IV}} \simeq -6.7\times10^{-27}\left(\frac{s_{2\alpha_2}}{t_\beta}\right)\ e\cdot\mathrm{cm} \quad (51)$$

in the region $t_\beta \lesssim 10$ and $s_{2\alpha_2} \ll 1$. This result is not sensitive to $\alpha_{1,3}$ and gives[10] $|s_{\alpha_2}/t_\beta| \lesssim 8.2\times10^{-4}$, which means the *CP* phase $|\arg(c_{f,1})| \lesssim 8.2\times10^{-4}$ for $f = \ell_i, U_i$. This is extremely small and would not be able to produce interesting *CP*-violating effects, so in the rest of this work we do not discuss these two 2HDM realizations further.

For Type II and III models, in contrast, numerical results show significant cancellation behavior for some parameter regions in the electron EDM calculation and thus α_2 is allowed to reach $\mathcal{O}(0.1)$. The reason is that different terms depend differently on t_β. As shown above, we can divide $d_e^{t,\gamma/Z,H_i}$ into two parts as $d_{e,(a)}^{t,\gamma/Z,H_i} \propto \mathrm{Re}(c_{t,i})\mathrm{Im}(c_{e,i})$ and $d_{e,(b)}^{t,\gamma/Z,H_i} \propto \mathrm{Re}(c_{e,i})\mathrm{Im}(c_{t,i})$. Then, based on the behavior $\sum_i(d_e^{W,\gamma/Z,H_i} + d_{e,(a)}^{t,\gamma/Z,H_i}) \propto s_{2\alpha_2}t_\beta$ and $\sum_i(d_{e,(b)}^{t,\gamma/Z,H_i}) \propto -s_{2\alpha_2}/t_\beta$, we confirm that there is always some region in which different contributions to the electron EDM almost cancel with each other, and thus a large $|\alpha_2| \sim \mathcal{O}(0.1)$ can be allowed. Other contributions may mildly shift the exact location where cancellation happens, but they do not modify the cancellation behavior. For these two models, we can discuss two different scenarios: (a) the heavy neutral scalars $H_{2,3}$ are close in mass and α_3 can be changed in a wide range; (b) H_2 and H_3 have a large mass splitting, and thus α_3 must be close to 0 or $\pi/2$.

We first consider Scenario (a). In this scenario the cancellation behavior is not sensitive to α_3 in a wide region (for example, $0.2 \lesssim \alpha_3 \lesssim 1.4$) because the $H_{2,3}$ are close in mass, and thus the dependences on α_3 from H_2 and H_3 contributions almost cancel each other. Thus, we choose $\alpha_3 = 0.8$, $m_2 = 500$ GeV, and $m_\pm = 600$ GeV as a benchmark point. We focus on the lower t_β region, which can generate a relatively large *CP*-violation phase in $ht\bar{t}$ vertex.[11] In the region with $\alpha_1 \sim 0$ and $t_\beta \sim 1$, we have

$$d_e^{\mathrm{II,III}} \simeq 3.4\times10^{-27}s_{2\alpha2}\left(t_\beta - \frac{0.904}{t_\beta}\right)\ e\cdot\mathrm{cm}, \quad (52)$$

which means the cancellation appears around $t_\beta \simeq 0.95$ or, equivalently, $\beta \simeq 0.76$. Different from the Type I and IV models, a large mixing angle $|\alpha_2| \sim \mathcal{O}(0.1)$ [and hence a *CP* phase $|\arg(c_{f,1})| \sim \mathcal{O}(0.1)$ for $f = \ell_i, U_i$] can be allowed due to the cancellation. We show the cancellation behavior of the electron EDM in the $\beta - \alpha_1$ plane in Fig. 3

[7]The contributions from the quark EDM are consistent with a recent lattice calculation with better uncertainty [103], while the lattice calculations of the contributions from the quark CEDM and Weinberg operator are still ongoing [113].

[8]Reference [114] presented the lattice result $\langle\bar{q}q\rangle(2\,\mathrm{GeV}) = -(283\,\mathrm{MeV})^3$ and also showed the RGE running effect as $d\langle m_q\bar{q}q\rangle(\mu)/d\ln\mu \propto m_q^4$, which is negligible for u and d quarks. Thus, we have $\langle\bar{q}q\rangle(1\,\mathrm{GeV})/\langle\bar{q}q\rangle(2\,\mathrm{GeV}) = m_q(2\,\mathrm{GeV})/m_q(1\,\mathrm{GeV}) = 0.73$.

[9]During the calculation of Fig. 1(a), we considered only the top quark in the upper loop and ignored the small contributions from other fermions. Such an approximation is good enough when t_β is not too large, such as $\lesssim$10. In cases with a larger t_β, contributions from the bottom quark or τ in the loop will become important.

[10]$\alpha_2 \simeq \pi/2$ is not allowed by other experiments, and thus we only consider the case $\alpha_2 \ll 1$.

[11]As pointed in Ref. [67], another cancellation region is around $t_\beta \simeq$ (10–20). However, $\arg(c_{t,1}) \propto t_\beta^{-1}$, and thus it is suppressed and difficult to test at colliders in this scenario. Thus, we will not discuss the large-t_β scenario in this paper.

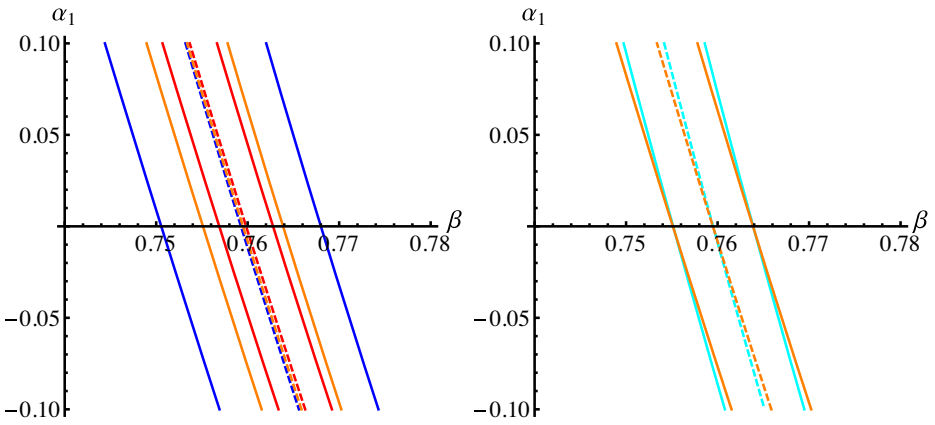

FIG. 3. Cancellation behavior between β and α_1 in Scenario (a) of Type II and Type III 2HDMs. As an example, the fixed parameters are listed in Table III. The solid lines are the boundaries with $|d_e| = 1.1 \times 10^{-29}\ e \cdot \mathrm{cm}$ and the regions between solid lines are allowed by the ACME experiment, while the dashed lines are for $d_e = 0$. In the left panel we show a Type II model. The blue, orange, and red lines are shown for $\alpha_2 = 0.05, 0.1, 0.15$, respectively. In the right panel we fix $\alpha_2 = 0.1$ and show a comparison between the Type II and Type III models. The orange lines are for the Type II model, while the cyan lines are for the Type III model.

for Type II and III models. The electron EDM sets a strict constraint which behaves as a strong correlation between β and α_1. Numerical analysis shows that, with fixed heavy scalar masses, the location where the cancellation happens is not sensitive to α_2, which is consistent with the result in Eq. (52), but the width of the allowed region is almost proportional to $1/s_{2\alpha_2}$. We show this behavior for the Type II model in the left panel of Fig. 3, where the blue, orange and red lines correspond to $\alpha_2 = 0.05$, 0.1, 0.15, respectively. The cancellation behavior in the Type III model is similar to that in the Type II model because the Barr-Zee diagram with a bottom-quark loop is negligible and thus the only difference comes from the electron-nucleon interaction part. In the right panel of Fig. 3, with fixed $\alpha_2 = 0.1$, we show a comparison of results for the Type II model (orange lines) and Type III model (cyan lines), and we find that they are almost the same. When $m_{2,3}$ increases the location where the cancellation happens will also change slowly, and we show the corresponding results in Fig. 4. When m_2 increases from 500 to 900 GeV, the cancellation location also moves slowly from about $\beta \simeq 0.76$ to $\beta \simeq 0.84$. The width of the allowed region is almost independent of the heavy scalar masses, as it is only sensitive to α_2. The cancellation behavior leads to the conclusion that there is always a narrow region that is allowed by the electron EDM measurement, and thus we cannot set a definite constraint on the *CP*-violation mixing angle α_2 only through the electron EDM, such as in the ACME experiment.

In contrast, the neutron EDM calculation does not involve such a cancellation behavior in the same region as the electron one, and thus it can be used to set direct constraints on the *CP*-violating mixing angle α_2. In the parameter region allowed by the electron EDM constraints, the CEDM of the d quark contributes dominantly to the neutron EDM. Numerical analysis shows that the neutron EDM $d_n \propto s_{2\alpha_2}$ and it is not sensitive to $\alpha_{1,3}$. We calculate

TABLE III. Fixed parameters of Scenario (a) to discuss the cancellation behavior. With these parameters and $\beta, \alpha_{1,2}$, we can calculate m_3 through Eq. (12), and calculate the couplings through the equations in Appendices A and B.

m_1	m_2	$m_\pm$	μ^2	α_3
125 GeV	500 GeV	600 GeV	$(450\ \mathrm{GeV})^2$	0.8

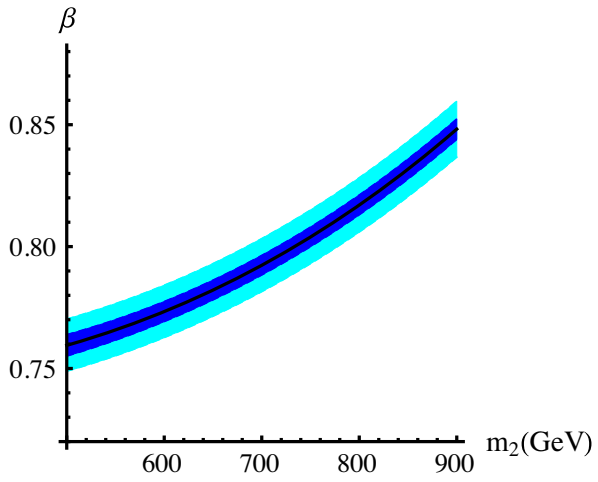

FIG. 4. Mass dependence in the cancellation region in the Type II model. Choosing $m_\pm - m_2 = 100$ GeV, $\alpha_3 = 0.8$, $\alpha_2 = 0.1$, $\alpha_1 = 0$, and $\mu^2 = (450\ \mathrm{GeV})^2$ as an example, the black line shows the value of β satisfying $d_e = 0$, while the dark blue region satisfies $|d_e| < 1.1 \times 10^{-29}\ e \cdot \mathrm{cm}$, which is allowed by the ACME experiment at 90% C.L. If we set $|\alpha_1| < 0.1$, the light blue region is allowed. Results for the Type III model are almost the same and thus we do not show them.

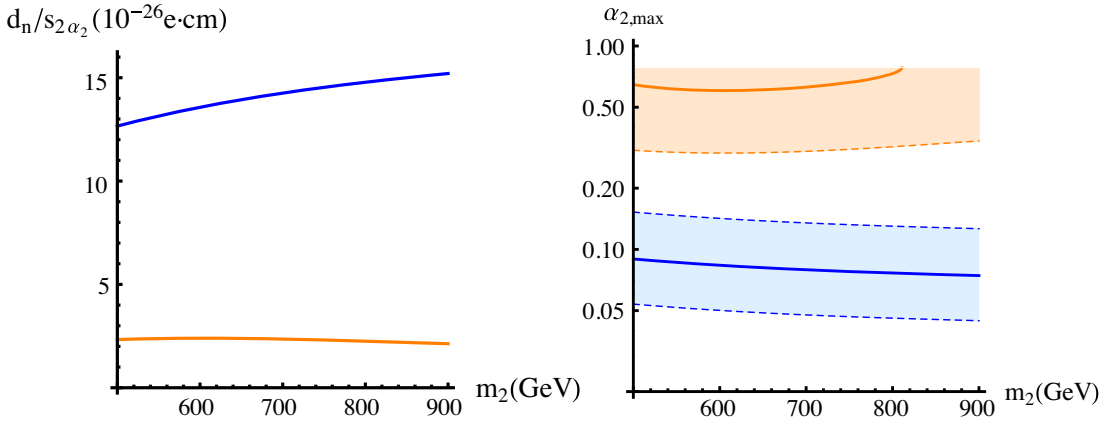

FIG. 5. Left: $d_n/s_{2\alpha_2}$ dependence on m_2 in the Type II (blue) and Type III (orange) models using the central value estimation of Eq. (50) in the parameter region allowed by the ACME experiment. We choose $\alpha_1 = 0$ and $\alpha_3 = 0.8$ as an example, but the modification due to these two angles is at less than the percent level, which is far smaller than the uncertainty in the theoretical estimation (about the 50% level). Right: the limit on α_2 in the Type II (blue) and III (orange) models. The solid lines are obtained through the estimation of the central value and the dashed lines are the boundaries considering the theoretical uncertainty. If theoretical uncertainties are taken into account, we cannot set any limit on α_2 in the Type III model through neutron EDM measurements.

its dependence on m_2 in the Type II and III models using the central value estimated in Eq. (50) and show the results in the left panel of Fig. 5. In the Type II model, α_2 is constrained by the neutron EDM (the latest result is $|d_n| < 2.2 \times 10^{-26}\ e \cdot \text{cm}$ at 95% C.L. [17]). Using the central value estimation in Eq. (50), $|\alpha_2| \lesssim (0.073\text{–}0.088)$ if m_2 changes in the range (500–900) GeV, as shown in the right panel of Fig. 5. Considering the uncertainty in the neutron EDM estimation [110], a larger $|\alpha_2| \sim 0.15$ can also be allowed.[12] In the Type III model, there is almost no constraint on α_2 from the neutron EDM.[13] This is because in the Type III model $\text{Re}(c_{u,i})\text{Im}(c_{d,i}) = -\text{Re}(c_{d,i})\text{Im}(c_{u,i})$, which is different from the relation in the Type II model. This leads to an accidental partial cancellation between the two terms [see Eq. (44)] in the d-quark CEDM contribution, which dominates the neutron EDM calculation.

Next we discuss Scenario (b), in which a large mass splitting exists in $m_{2,3}$, corresponding to the cases in which α_3 is close to either $\pi/2$ or 0. From Eq. (12) we can find two solutions for t_{α_3}:

$$t_{\alpha_3^\pm} = \frac{(m_3^2 - m_2^2) \pm \sqrt{(m_3^2 - m_2^2)^2 s_{2\beta+\alpha_1}^2 - 4(m_3^2 - m_1^2)(m_2^2 - m_1^2) s_{\alpha_2}^2 c_{2\beta+\alpha_1}^2}}{2(m_2^2 - m_1^2) s_{\alpha_2} c_{2\beta+\alpha_1}}. \tag{53}$$

In the large-mass-splitting scenario, α_3^+ is close to $\pi/2$ and α_3^- is close to 0. In the α_3^+ case, H_2 is a CP-mixed state in which the pseudoscalar component is dominant, while H_3 is almost a pure scalar. Conversely, in the α_3^- case H_3 is a CP-mixed state, while H_2 is almost a pure scalar. In this scenario, the large mass splitting between $H_{2,3}$ leads to a significant $H_3 \to H_2 Z$ decay, because the coupling is just $c_{V,1}$, which is not suppressed by mixing angles. Numerical analysis shows a similar cancellation behavior as in Scenario (a) in both ($\alpha_3^\pm$) cases. We show the results of the Type II model in the upper two panels of Fig. 6. Similar to Scenario (a), the cancellation behavior in the Type III model is almost the same as that in the Type II model and we show a comparison in the lower two panels of Fig. 6.

The behavior of the neutron EDM is also similar to that of Scenario (a). In the regions allowed by the electron EDM constraint, d_n is only sensitive to α_2 and is almost independent of α_1. With the benchmark points in Table IV, and using the indices II/III and $+/-$ to denote Type II/III models and $\alpha^{+/-}$ cases, we have

[12]As discussed above, here we do not consider the region α_2 close to $\pi/2$ since it corresponds to the case in which H_1 is dominated by the pseudoscalar component, which can be excluded by other experiments. See the next section for more details.

[13]If we consider only the central value of the neutron EDM estimation (50), the constraint is about $|s_{2\alpha_2}| \lesssim 0.9$, meaning that $\alpha_{2,\max}$ is already close to $\pi/4$. However, if the large theoretical uncertainty in the neutron EDM estimation is also taken into account, we cannot exclude any value for $|s_{2\alpha_2}| \leq 1$, which means no constraint on $|\alpha_2|$ can be set in the Type III model.

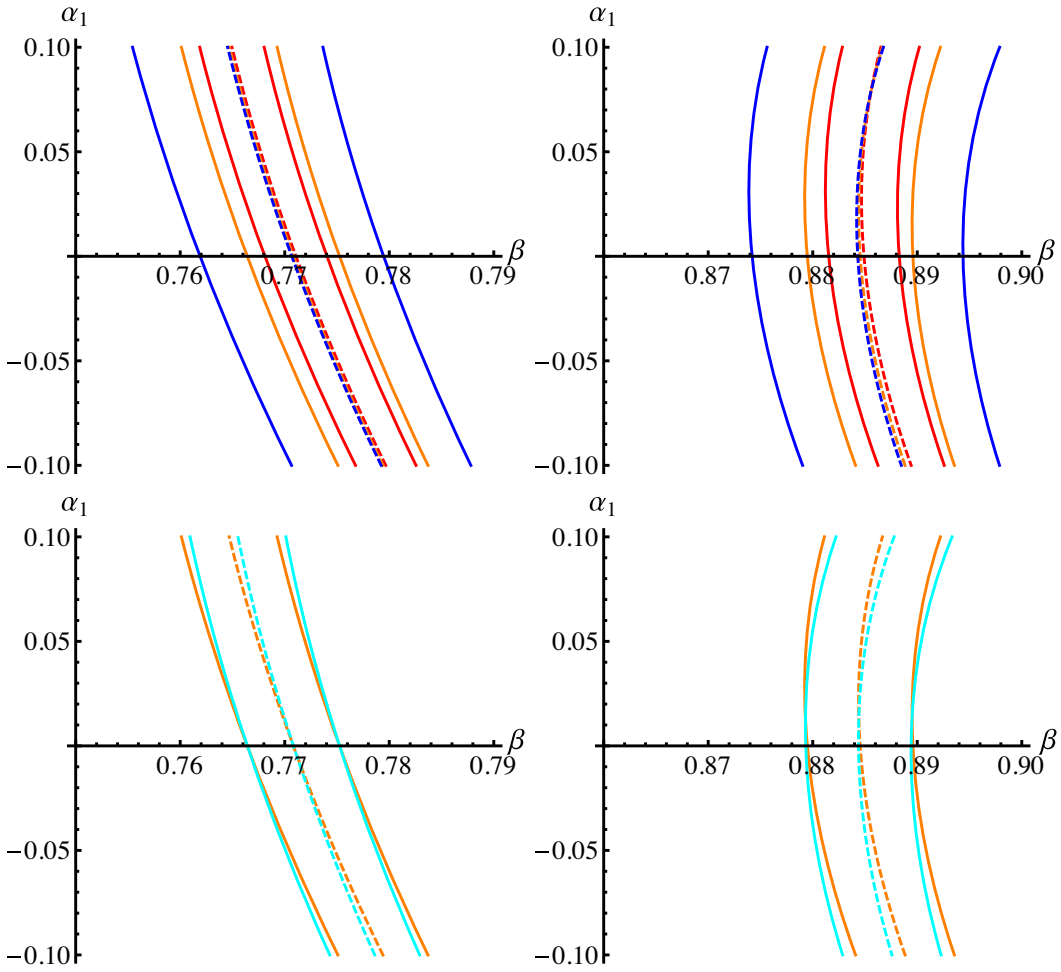

FIG. 6. Similar to Scenario (a), the electron EDM sets a strict constraint which behaves as a strong correlation between β and α_1. As an example, the fixed parameters are listed in Table IV. We show the cancellation behavior of the Type II model in the upper two panels and a comparison between the Type II and III models in the lower two panels. The color notation is the same as in Fig. 3. The left two panels correspond to the case α_3^+, while the right two panels correspond to the case α_3^-. We have approximately $\alpha_3^+ \simeq \pi/2 - 1.5 \times 10^{-2}\alpha_2$ and $\alpha_3^- \simeq -0.52\alpha_2$.

$$d_n^{\mathrm{II},+}/s_{2\alpha_2} \simeq 1.4 \times 10^{-25}\ e \cdot \mathrm{cm}, \tag{54}$$

$$d_n^{\mathrm{II},-}/s_{2\alpha_2} \simeq 1.3 \times 10^{-25}\ e \cdot \mathrm{cm}, \tag{55}$$

$$d_n^{\mathrm{III},+}/s_{2\alpha_2} \simeq 2.4 \times 10^{-26}\ e \cdot \mathrm{cm}, \tag{56}$$

$$d_n^{\mathrm{III},-}/s_{2\alpha_2} \simeq 1.9 \times 10^{-26}\ e \cdot \mathrm{cm} \tag{57}$$

TABLE IV. Fixed parameters of Scenario (b) to discuss the cancellation behavior. With these parameters and $\beta, \alpha_{1,2}$, we can calculate $\alpha_3^{\pm}$ through Eq. (53), and calculate the couplings through the equations in Appendices A and B.

m_1	m_2	m_3	$m_{\pm}$	μ^2
125 GeV	500 GeV	650 GeV	700 GeV	$(450\ \mathrm{GeV})^2$

based on the central value estimation in Eq. (50). Thus, we can obtain the upper limit on α_2 in the Type II model as

$$\alpha_2 \lesssim \begin{cases} 0.079 & (\alpha_3^+ \text{case}), \\ 0.085 & (\alpha_3^- \text{case}). \end{cases} \tag{58}$$

There is no constraint on α_2 from the neutron EDM in the Type III model for the same reason as discussed above for Scenario (a).

In both Scenarios (a) and (b), the cancellation can appear around the region $t_\beta \simeq 1$, and thus both α_2 and $\arg(c_{t,1})$ can reach $\mathcal{O}(0.1)$, which leads us to the phenomenological studies of *CP* violation in $t\bar{t}H_1$ production in Sec. V. For this process, both scenarios have similar behaviors. In the future, if we go deeper into the phenomenology of heavy scalars, differences between these two scenarios will arise.

For example, there will be $H_3 \to ZH_2$ decay in Scenario (b), but such a process cannot appear in Scenario (a).

D. Future neutron EDM tests

Several groups are currently planning new measurements of the neutron EDM, to an accuracy of $\mathcal{O}(10^{-27}\ e\cdot\text{cm})$ or even better [10,13,115–119]. Such an order-of-magnitude improvement in accuracy would be very helpful to perform further tests on the Type II and III 2HDM scenarios considered here.

If no anomaly is discovered in future neutron EDM measurements, the upper limit on d_n would improve to about $10^{-27}\ e\cdot\text{cm}$, and there would be more stringent limits on α_2 in both Type II and III models, as shown in Fig. 7 for Scenario (a). With future neutron EDM measurements, α_2 can be constrained to $\mathcal{O}(10^{-2})$ in the Type III model and to $\mathcal{O}(10^{-3})$ in the Type II model. Similar constraints can be placed in Scenario (b). In the current analysis, the expected limit on α_2 still contains large uncertainties (see the colored bands in Fig. 7) due to the theoretical uncertainties in the estimation of the neutron EDM from sum rules [110]. Future theoretical estimations of the neutron EDM from lattice experiments are expected to have better accuracy [$\sim\mathcal{O}(10\%)$] [103,113], and thus it will be more effective at obtaining future limits on α_2 with smaller uncertainties.[14]

In contrast, if $\alpha_2 \sim \mathcal{O}(0.1)$, there will be significant BSM evidence in future neutron EDM measurements. In the models that contain a similar cancellation mechanism in the electron EDM, the neutron EDM experiments may be used to find the first evidence of a new CP-violation source or set the strictest limit directly on the CP-violating phase α_2.

E. Summary of EDM tests

In the previous subsections we discussed the electron and neutron EDM tests in the 2HDM with soft CP violation. There is no cancellation mechanism in the Type I and IV models and thus the electron EDM can set strict constraints on the CP-violation angle as $|\arg(c_{f,1})| \simeq |s_{\alpha_2}/t_\beta| \lesssim 8.2\times10^{-4}$. However, this value is too small to give any observable CP effects in other experiments, and thus we decided not to further discuss these two 2HDM realizations. In contrast, cancellations among various contributions to the electron EDM can occur in the Type II and III models. Here, we still face stringent constraints but these will induce a strong correlation between β and α_1. However, we cannot set constraints directly on the CP-violation mixing angle α_2. The behavior is the same in the Type II and III models. In fact, it is also the same in both Scenario (a) (in which $m_{2,3}$ are close to each other) and Scenario (b) (in which $m_{2,3}$ have a large splitting). A cancellation generally happens around $t_\beta \sim 1$, with the exact location depending weakly on the masses of the heavy (pseudo)scalars.

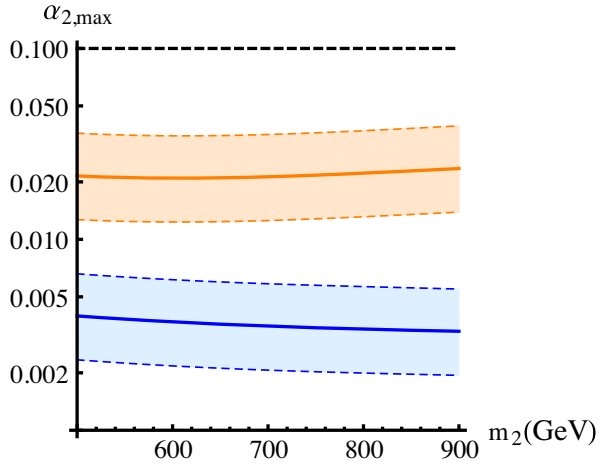

FIG. 7. Upper limit on α_2 in the Type II and III models when the future limit decreases to $|d_n| < 10^{-27}\ e\cdot\text{cm}$. The color scheme is the same as above: blue for the Type II model and orange for the Type III model. The solid lines are obtained using the central value estimation and, if we consider the current theoretical uncertainty estimation of Ref. [110], the boundaries of the limits on α_2 are the dashed lines.

Current measurements of the neutron EDM can set an upper limit on $|\alpha_2| \simeq (0.073\text{–}0.088)$ in the Type II model, depending on different scenarios and masses, if we take the central value of the neutron EDM estimation. Such limits can be weakened to about 0.15 if we consider the theoretical uncertainty. But one cannot set limits on α_2 in the Type III model, because the CEDM of the d quark in this model is suppressed by a partial cancellation. However, α_2 in the Type III model is constrained by collider tests, which will be discussed in the next section.

Finally, we showed the importance of future neutron EDM measurements in our models relying on the cancellation mechanism in the electron EDM. For $\alpha_2 \sim \mathcal{O}(0.1)$, there would be significant evidence in future neutron EDM experiments, which will be more sensitive than any other experiments. And if there is no evidence of a nonzero neutron EDM, the improved limit on the neutron EDM will set strict constraints on the CP-violation mixing angle: the upper limit of $|\alpha_2|$ will reach $\mathcal{O}(10^{-2})$ in the Type III model and $\mathcal{O}(10^{-3})$ in the Type II model. To explain the matter-antimatter asymmetry, $|\arg(c_{t,1})| \gtrsim 10^{-2}$ is

[14]To obtain an effective limit, the uncertainty must not be too large, e.g., similar to or even larger than the central value. As a comparison, the EDMs for diamagnetic atoms are also good candidates to probe new CP violation [120–122]. However, based on the results in Refs. [56,67,102,123], the EDM for the ^{199}Hg atom is $d^{\text{II}}_{\text{Hg}}/s_{2\alpha_2} \simeq (-1.7^{+2.3}_{-2.5})\times10^{-27}\ e\cdot\text{cm}$ and $d^{\text{III}}_{\text{Hg}}/s_{2\alpha_2} \simeq (-1.3^{+1.9}_{-0.8})\times10^{-27}\ e\cdot\text{cm}$ for Scenario (a) with $m_2 = 500$ GeV in the Type II and III models, respectively. The results cross zero within the 1σ level due to large theoretical uncertainties, meaning that it is impossible to set constraints directly on α_2 through the EDM of ^{199}Hg (or similar atoms) in the low-t_β region.

required [74–77]. Thus, if future neutron EDM experiments still show null results to an accuracy $\sim 10^{-27}\ e\cdot\mathrm{cm}$, the Type II model will not be able to explain the matter-antimatter asymmetry, due to the very strict constraint on α_2.

IV. CURRENT COLLIDER CONSTRAINTS

Any BSM model must face LHC tests. In our 2HDM with soft *CP* violation, as mentioned, we treat H_1 as the 125 GeV Higgs boson. In this scenario then, the latter mixes with the other (pseudo)scalar states and its couplings will be modified from the corresponding SM values. However, these modified couplings are constrained by global fits of the so-called Higgs signal-strength measurements. In addition, the scalar sector is extended in a 2HDM, so that direct searches for these new particles at the LHC will also set further constraints on this BSM scenario. In this respect, we discuss only the Type II and III 2HDMs, in which the cancellation behavior in the electron EDM still allows a large *CP* phase in Yukawa interactions.

A. Global fit of Higgs signal strengths

The Higgs boson H_1 is produced at the LHC mainly through four channels: gluon fusion (ggF), vector-boson fusion (VBF), and associated production with a vector boson ($V+H_1$, here $V=W,\ Z$) or a top-quark pair ($t\bar{t}+H_1$) [124–127]. The decay channels $H\to b\bar{b},\tau^+\tau^-$, $\gamma\gamma, WW^*$, and ZZ^* have already been discovered. We define the signal strength $\mu_{i,f}$ corresponding to production channel i and decay channel f as follows:

$$\mu_{i,f}\equiv\frac{\sigma_i}{\sigma_{i,\mathrm{SM}}}\cdot\frac{\Gamma_f}{\Gamma_{f,\mathrm{SM}}}\cdot\frac{\Gamma_{\mathrm{tot,SM}}}{\Gamma_{\mathrm{tot}}},\tag{59}$$

where σ_i denotes the production cross section of the production channel i among those listed above, Γ_f denotes the decay width of channel f, and Γ_{tot} denotes the total decay width of H_1. Quantities with the index "SM" denote the values predicted by the SM. Such signal strengths for different channels have been measured by the ATLAS [128–131] and CMS [132–134] collaborations; we list them in Table V.

TABLE V. Signal strength measurements by the ATLAS (left) and CMS (right) collaborations at $\sqrt{s}=13$ TeV. The luminosity is $\leq 139\ \mathrm{fb}^{-1}$ for the ATLAS measurements and $\leq 137\ \mathrm{fb}^{-1}$ for the CMS measurements.

	ggF	VBF	$V+H$	$t\bar{t}+H$
$H\to b\bar{b}$	⋯	$3.01^{+1.67}_{-1.61}$	$1.19^{+0.27}_{-0.25}$	$0.79^{+0.60}_{-0.59}$
$H\to\tau^+\tau^-$	$0.96^{+0.59}_{-0.52}$	$1.16^{+0.58}_{-0.53}$	⋯	$1.38^{+1.13}_{-0.96}$
$H\to\gamma\gamma$	$0.96^{+0.14}_{-0.14}$	$1.39^{+0.40}_{-0.35}$	$1.09^{+0.58}_{-0.54}$	$1.38^{+0.32}_{-0.30}$
$H\to WW^*$	$1.08^{+0.19}_{-0.19}$	$0.59^{+0.36}_{-0.35}$	⋯	$1.56^{+0.42}_{-0.40}$
$H\to ZZ^*$	$1.04^{+0.16}_{-0.15}$	$2.68^{+0.98}_{-0.83}$	$0.68^{+1.20}_{-0.78}$	⋯

	ggF	VBF	$V+H$	$t\bar{t}+H$
$H\to b\bar{b}$	$2.45^{+2.53}_{-2.35}$	⋯	$1.06^{+0.26}_{-0.25}$	$1.13^{+0.33}_{-0.30}$
$H\to\tau^+\tau^-$	$0.39^{+0.38}_{-0.39}$	$1.05^{+0.30}_{-0.29}$	$2.2^{+1.1}_{-1.0}$	$0.81^{+0.74}_{-0.67}$
$H\to\gamma\gamma$	$1.09^{+0.15}_{-0.14}$	$0.77^{+0.37}_{-0.29}$	⋯	$1.62^{+0.52}_{-0.43}$
$H\to WW^*$	$1.28^{+0.20}_{-0.19}$	$0.63^{+0.65}_{-0.61}$	$1.64^{+1.36}_{-1.14}$	$0.93^{+0.48}_{-0.45}$
$H\to ZZ^*$	$0.98^{+0.12}_{-0.11}$	$0.57^{+0.46}_{-0.36}$	$1.10^{+0.96}_{-0.74}$	$0.25^{+1.03}_{-0.25}$

As intimated, in the 2HDM, H_1 couplings to SM particles are modified due to the mixing with other (pseudo)scalars and thus the aforementioned signal strengths are modified. The production cross sections satisfy [135–137]

$$\frac{\sigma_{\mathrm{VBF}}}{\sigma_{\mathrm{VBF,SM}}}=\frac{\sigma_{V+H}}{\sigma_{V+H,\mathrm{SM}}}=c_{V,1}^2,\tag{60}$$

$$\frac{\sigma_{gg\mathrm{F}}}{\sigma_{ggF,\mathrm{SM}}}=\left|\mathrm{Re}(c_{t,1})+\mathrm{i}\frac{\mathcal{B}_1(\frac{z_{H_1t}}{4})}{\mathcal{A}_1(\frac{z_{H_1t}}{4})}\mathrm{Im}(c_{t,1})\right|^2\simeq[\mathrm{Re}(c_{t,1})]^2+2.3[\mathrm{Im}(c_{t,1})]^2,\tag{61}$$

$$\frac{\sigma_{t\bar{t}+H}}{\sigma_{t\bar{t}+H,\mathrm{SM}}}\simeq[\mathrm{Re}(c_{t,1})]^2+0.37[\mathrm{Im}(c_{t,1})]^2,\tag{62}$$

while the decay widths satisfy [135,136]

$$\frac{\Gamma_{ZZ^*}}{\Gamma_{ZZ^*,\mathrm{SM}}}=\frac{\Gamma_{WW^*}}{\Gamma_{WW^*,\mathrm{SM}}}=c_{V,1}^2,\tag{63}$$

$$\frac{\Gamma_{f\bar{f}}}{\Gamma_{f\bar{f},\mathrm{SM}}}=|c_{f,1}|^2,\ (f=c,b,\tau),\tag{64}$$

$$\frac{\Gamma_{gg}}{\Gamma_{gg,\mathrm{SM}}}=\left|\mathrm{Re}(c_{t,1})+\mathrm{i}\frac{\mathcal{B}_1(\frac{z_{H_1t}}{4})}{\mathcal{A}_1(\frac{z_{H_1t}}{4})}\mathrm{Im}(c_{t,1})\right|^2\simeq[\mathrm{Re}(c_{t,1})]^2+2.3[\mathrm{Im}(c_{t,1})]^2,\tag{65}$$

$$\frac{\Gamma_{\gamma\gamma}}{\Gamma_{\gamma\gamma,\mathrm{SM}}}=\left|\frac{\frac{c_{+,1}v^2}{2m_+^2}\mathcal{A}_0(\frac{z_{1,+}}{4})+c_{V,1}\mathcal{A}_2(\frac{z_{H_1W}}{4})+\frac{4}{3}[\mathrm{Re}(c_{t,1})\mathcal{A}_1(\frac{z_{H_1t}}{4})+\mathrm{iIm}(c_{t,1})\mathcal{B}_1(\frac{z_{H_1t}}{4})]}{\frac{4}{3}\mathcal{A}_1(\frac{z_{H_1t}}{4})+\mathcal{A}_2(\frac{z_{H_1W}}{4})}\right|^2$$
$$\simeq[1.28c_{V,1}-0.28\mathrm{Re}(c_{t,1})-0.02]^2+0.19[\mathrm{Im}(c_{t,1})]^2.\tag{66}$$

TABLE VI. Predictions of the main BRs of the SM Higgs boson with mass 125 GeV.

$BR^{SM}_{b\bar{b}}$	$BR^{SM}_{\tau^+\tau^-}$	$BR^{SM}_{c\bar{c}}$	$BR^{SM}_{WW^*}$	$BR^{SM}_{ZZ^*}$	BR^{SM}_{gg}
58.2%	6.3%	2.9%	21.4%	2.6%	8.2%

TABLE VII. The $\chi^2_{\rm min}$/d.o.f. for the Type II and Type III models using ATLAS data, CMS data, and their combination, respectively.

$\chi^2_{\rm min}$/d.o.f.	ATLAS	CMS	ATLAS + CMS
Type II	11.8/13	12.2/15	24.2/31
Type III	12.7/13	11.9/15	24.8/31

The loop functions $\mathcal{A}_{0,1,2}$ and $\mathcal{B}_1$ are listed in Appendix D. Here, $c_{V,1} = c_{\alpha_1} c_{\alpha_2}$ holds for all types of models, while $c_{f,1}$ depend on the model type and are listed in Appendix A. The $t\bar{t} + H_1$ cross section ratio in Eq. (62) is only valid for the LHC at $\sqrt{s} = 13$ TeV. For the $\gamma\gamma$ decay (66), the charged-Higgs-loop contribution is small compared with the top-quark and W loops, and we choose the case $m_\pm = 600$ GeV for illustration. The total width satisfies

$$\frac{\Gamma_{\rm tot}}{\Gamma_{\rm tot,SM}} = \sum_f {\rm BR}^{\rm SM}_f \cdot \frac{\Gamma_f}{\Gamma_{f,\rm SM}}. \tag{67}$$

BR^{SM}_f is the SM prediction of the branching ratio (BR) of the SM Higgs boson decay to the final state f, and thus all of the modifications are normalized to the SM values. For the 125 GeV SM Higgs boson, we list the theoretical predictions of the BRs of the main decay channels in Table VI [127].

We perform χ^2 fits, where

$$\chi^2 \equiv \sum_{i,f} \left(\frac{\mu^{\rm exp}_{i,f} - \mu^{\rm th}_{i,f}}{\delta\mu^2_{i,f}} \right)^2, \tag{68}$$

where $\mu^{\rm th}_{i,f}$ is the theoretically predicted signal strength, $\mu^{\rm exp}_{i,f}$ is the experimentally measured one, and $\delta\mu_{i,f}$ is the associated uncertainty. The possible small correlations across production and decay channels are ignored. For a 2HDM, χ^2 depends only on $\beta, \alpha_{1,2}$. We perform global fits for the Type II and III models, in which $\alpha_2 \sim \mathcal{O}(0.1)$ is still allowed. The minimal χ^2 (denoted by $\chi^2_{\rm min}$) obtained from ATLAS and CMS data as well as the combined one are listed in Table VII. The fitting, normalized to the degrees of freedom (d.o.f.), is good enough because the models approach the SM limit when $\alpha_{1,2} \to 0$. If one then defines $\delta\chi^2 \equiv \chi^2 - \chi^2_{\rm min}$, this is useful to find the allowed parameter regions of the two 2HDM realizations considered. Our numerical study shows that the results depend weakly on β. We choose $\beta = 0.76$ [corresponding to $m_{2,3} \sim 500$ GeV in Scenario (a)] as an example and show the allowed region from combined ATLAS and CMS results in the $\alpha_2 - \alpha_1$ plane in Fig. 8. For both Types II and III, the global fit requires $|\alpha_2| \lesssim 0.33$ in the region $\beta \sim$ (0.7–1). For the Type II model, this constraint is weaker when compared with that from the neutron EDM. Nevertheless, it can set a new constraint on $|\alpha_2|$ for the Type III model. The allowed range for $|\alpha_1|$ in the latter is wider than the one in the Type II model, in fact. In both models, α_1 is favored when close to 0, and thus, in the following discussion, we usually fix $\alpha_1 = 0.02$, a value which is not far from the best-fit points in most cases. In Fig. 9, we show instead the allowed regions in the α_1-β plane for fixed $\alpha_2 = 0.1$, 0.2

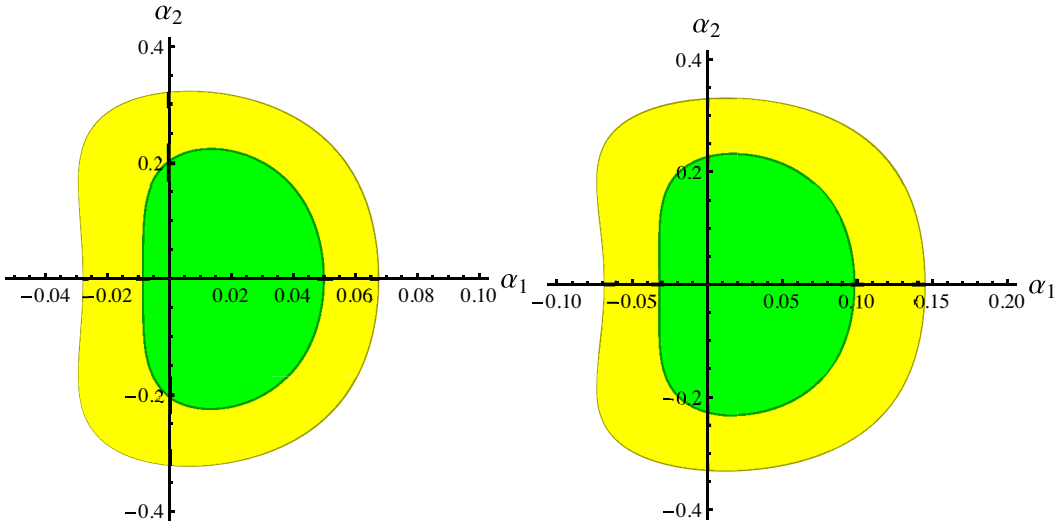

FIG. 8. Allowed regions in the α_2-α_1 plane obtained by using the combined results from the ATLAS and CMS collaborations, with fixed $\beta = 0.76$ for Type II (left) and Type III (right). Green regions are allowed at 68% C.L. ($\delta\chi^2 \leq 2.3$) and yellow regions are allowed at 95% C.L. ($\delta\chi^2 \leq 6.0$).

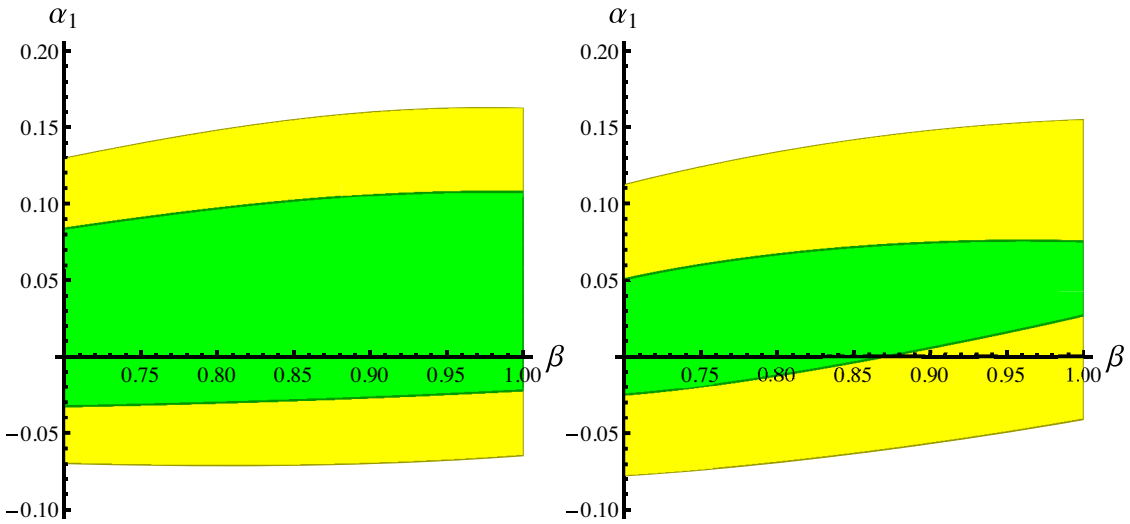

FIG. 9. Allowed regions in the α_1-β plane obtained by using the combined results from the ATLAS and CMS collaborations, with fixed $\alpha_2 = 0.1$ (left) and 0.2 (right), in the Type III model. Green regions are allowed at 68% C.L. ($\delta\chi^2 \leq 2.3$) and yellow regions are allowed at 95% C.L. ($\delta\chi^2 \leq 6.0$).

in the Type III model. The dependence on β is indeed weak, but it increases somewhat when α_2 gets larger, as shown in the figure.

B. LHC direct searches for heavy scalars: Through the *ZZ* final state

In the 2HDM there are four additional scalars—$H_{2,3}$ and $H^{\pm}$—beyond the SM-like one H_1. Thus, we must also check the direct searches for these (pseudo)scalars at the LHC. Notice that $H_{2,3}$ dominantly decay to $t\bar{t}$ and we show their decay widths and BRs in Appendix E. The $H_{2,3} \to 2H_1$ decays are ignored because such channels are suppressed in the allowed parameter region isolated so far. In Scenario (b), $H_3 \to ZH_2$ decay is also open if $m_3 - m_2 > m_Z$. In addition, H^- dominantly decays to $\bar{t}b$.

In this section we discuss the process $gg \to H_{2,3} \to ZZ$. Theoretically, this process is sensitive to the couplings between $H_{2,3}$ and the gauge vector bosons, and hence sensitive to α_2. Experimentally, this process is the most sensitive channel in searches for heavy neutral scalars. The current LHC limit for $m_2 = 500$ GeV is $\sigma_{gg\to H_{2,3}\to ZZ} \lesssim 0.1$ pb at 95% C.L. [138] at $\sqrt{s} = 13$ TeV with about 40 fb^{-1} of luminosity. We first consider the resonance cross section of the $gg \to H_{2,3} \to ZZ$ process. For Scenario (a), in which $H_{2,3}$ are close in mass such that $|m_2 - m_3| \simeq \mathcal{O}(\text{GeV}) \ll \Gamma_{2,3} \simeq 20$ GeV for $m_2 \simeq 500$ GeV (where we have denoted the widths of the two heavy Higgs states by $\Gamma_{2,3}$), we must consider the interference between the H_2 and H_3 production processes. To the one-loop order, we have for the resonance cross section

$$\sigma_{ZZ}^{\text{res}} = \sigma_S + \sigma_P, \tag{69}$$

where σ_S is the contribution from $\text{Re}(c_{t,2,3})$ corresponding to the *CP*-conserving part, and σ_P is the contribution from $\text{Im}(c_{t,2,3})$ corresponding to the *CP*-violating part. Their *ZZ* invariant mass distributions are then separately given by

$$\frac{d\sigma_S}{dq} = \int dx_1 dx_2 f_g(x_1) f_g(x_2) \delta\left(x_1 x_2 - \frac{q^2}{s}\right) \hat{\sigma}_S(q) \times \frac{2q^3 m_2 \Gamma_0(q)}{\pi s} \left| \sum_{i=2,3} \frac{c_{V,i}\text{Re}(c_{t,i})}{q^2 - m_i^2 - \text{i}m_i\Gamma_i} \right|^2, \tag{70}$$

$$\frac{d\sigma_P}{dq} = \int dx_1 dx_2 f_g(x_1) f_g(x_2) \delta\left(x_1 x_2 - \frac{q^2}{s}\right) \hat{\sigma}_P(q) \times \frac{2q^3 m_2 \Gamma_0(q)}{\pi s} \left| \sum_{i=2,3} \frac{c_{V,i}\text{Im}(c_{t,i})}{q^2 - m_i^2 - \text{i}m_i\Gamma_i} \right|^2. \tag{71}$$

In the equations above, $f_g(x)$ denotes the gluon parton distribution function (PDF) which, in our numerical study, is chosen to be the MSTW2008 set [139]. The function [135,136]

$$\Gamma_0(q) = \frac{q^3}{32\pi v^2}\left(1 - \frac{4m_Z^2}{q^2}\right)\left(1 - \frac{4m_Z^2}{q^2} + \frac{12m_Z^4}{q^4}\right) \tag{72}$$

is the decay width to the *ZZ* final state of a would-be SM Higgs boson with mass q. The functions [135,136]

$$\hat{\sigma}_S(q) = \frac{G_F \alpha_s^2}{288\sqrt{2}\pi} \left| \frac{3}{4} \mathcal{A}_1\left(\frac{q^2}{4m_t^2}\right) \right|^2, \tag{73}$$

$$\hat{\sigma}_P(q) = \frac{G_F \alpha_s^2}{288\sqrt{2}\pi} \left| \frac{3}{4} \mathcal{B}_1\left(\frac{q^2}{4m_t^2}\right) \right|^2 \tag{74}$$

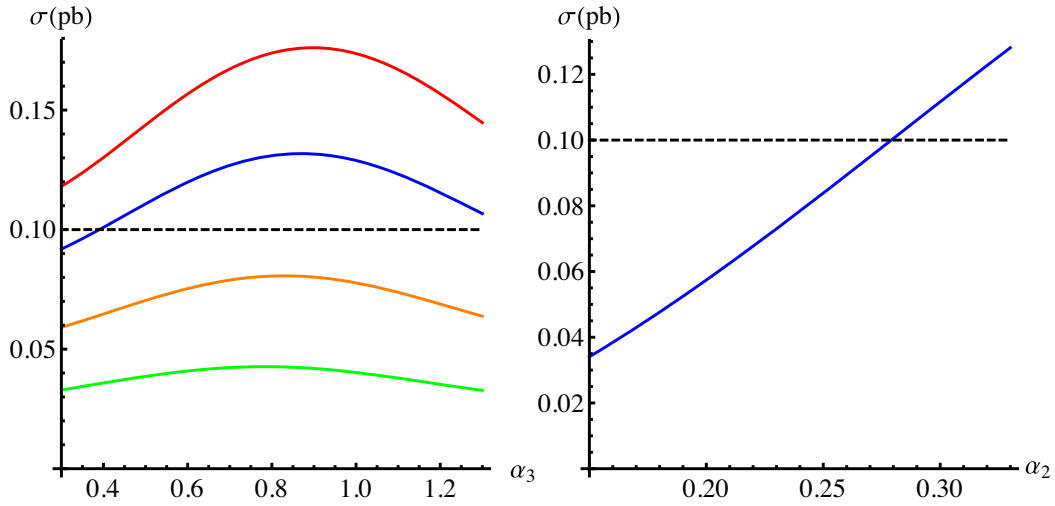

FIG. 10. Cross sections $\sigma_{ZZ}^{\rm tot} \approx \sigma_{ZZ}^{\rm res}$ as a function of the mixing angles $\alpha_{2,3}$ in the Type III model. In the left panel we show the cross section depending on α_3 in Scenario (a), fixing $\beta = 0.76$ and $\alpha_1 = 0.02$. From top to bottom, the four lines show results with $\alpha_2 = 0.33$, 0.27, 0.2, 0.14, respectively. In the right panel we show the cross section depending on α_2 in Scenario (b), fixing $\beta = 0.76$ and $\alpha_1 = 0.02$, with α_3 chosen as $\alpha_3^+ (\simeq 1.5 \times 10^{-2} \alpha_2)$ which corresponds to $m_3 \simeq 650$ GeV.

are the parton-level cross sections of a pure scalar (pseudoscalar) state with couplings $c_t = 1$(i). The loop functions $\mathcal{A}_1$ and $\mathcal{B}_1$ are listed in Appendix D.

The SM $gg \to ZZ$ production arises through the box diagrams, which leads to the interference effects with the resonance production. We denote $\sigma_{ZZ}^{\rm int}$ as the cross section induced by interference between resonance and the SM background. To the one-loop level, our numerical calculations show that if $|\alpha_2| \sim \mathcal{O}(0.1)$, we have $|\sigma_{ZZ}^{\rm int}/\sigma_{ZZ}^{\rm res}| \sim \mathcal{O}(10^{-3})$ [140–143], meaning that we can safely ignore the interference effects and consider only the resonance production.[15] Thus, the total cross section (without the SM background) is approximately the resonance cross section,

$$\sigma_{ZZ}^{\rm tot} \approx \sigma_{ZZ}^{\rm res} = \int_{m_{2,3}-\Delta q/2}^{m_{2,3}-\Delta q/2} dq \left(\frac{d\sigma_S}{dq} + \frac{d\sigma_P}{dq} \right). \quad (75)$$

For $m_2 \simeq 500$ GeV, we choose $\Delta q = 50$ GeV as the mass window where interference between $H_{2,3}$ is accounted for.

Numerically, we show the cross sections depending on the mixing angles in Fig. 10 by fixing $m_2 = 500$ GeV in the Type III model. The left panel is for Scenario (a) and the right panel is for Scenario (b) for the α_3^+ case. In both scenarios, we can see that $\alpha_2 \lesssim 0.27$ is favored when $m_2 = 500$ GeV. For Scenario (a), when we choose $\alpha_2 = 0.27$, $\alpha_3 \lesssim 0.4$ or $\gtrsim 1.2$ is favored, which still keeps $H_{2,3}$ nearly degenerate in mass. However, in the cases with $\alpha_2 \lesssim 0.2$ or $m_2 \gtrsim 600$ GeV, there are no further constraints on α_3. For Scenario (b), α_3 is fixed by other parameters. In the α_3^- case, $c_{2,V}$ is suppressed (close to α_1), and thus it faces no further constraints here. In the Type II model, we can obtain the same cross section as in the Type III model with the same parameters. In the Type II model, due to the stricter neutron EDM constraint on α_2, the considered parameter space is always allowed by the collider data. Thus, in the following phenomenological analysis we generally choose $\alpha_2 = 0.27$ (unless stated otherwise) as a benchmark point, corresponding to the largest allowed CP-violation effects in the Type III model with $m_2 = 500$ GeV.

C. LHC direct searches for heavy scalars: Through $t\bar{t}$ and other final states

As mentioned, $H_{2,3}$ dominantly decay to a $t\bar{t}$ final state and the current LHC limit for $m_2 = 500$ GeV is about $\sigma_{pp \to H_{2,3} \to t\bar{t}} \lesssim 7$ pb at 95% C.L. [144] at $\sqrt{s} = 13$ TeV and 36 fb^{-1} of luminosity. In contrast to the ZZ channel, the interference with the SM background is very important in the $t\bar{t}$ channel [145,146], which strongly decreases the signal cross section compared with the pure resonance production cross section, so long as nonresonant Higgs diagrams can be subtracted [147]. The total cross section can be divided into

$$\sigma_{gg \to t\bar{t}} = \sigma_{\rm SM} + \sigma_{\rm res} + \sigma_{\rm int} = \sigma_{\rm SM} + \delta\sigma_{t\bar{t}}. \quad (76)$$

[15]Different from the $t\bar{t}$ production below, here the interference effects in ZZ production is very small compared to the resonance production. This is because (i) the SM amplitude generated through box diagrams contains a loop suppression, and (ii) the interference only happens between the SM and the CP-conserving part of the resonance amplitude $\mathcal{A}_S \propto s_{\alpha_2}^2$ in both scenarios ($\sigma_S \propto |\mathcal{A}_S|^2$). However, for the CP-violating part the amplitude $\mathcal{A}_P \propto s_{\alpha_2} c_{\alpha_2}$, and thus $\sigma_P \propto |\mathcal{A}_P|^2$ contributes dominantly to the total cross section $\sigma_{ZZ}^{\rm tot} \approx \sigma_{ZZ}^{\rm res}$.

Here, $\sigma_{\rm SM}$ denotes the SM background cross section of the $gg \to t\bar{t}$ process, while $\sigma_{\rm res}$ and $\sigma_{\rm int}$ denote the resonant and interference cross section, respectively. Furthermore, $\delta\sigma_{t\bar{t}}$ is the cross section difference between the 2HDM and SM, i.e.,

$$\delta\sigma_{t\bar{t}} \equiv \sigma_{\rm res} + \sigma_{\rm int} = \int dx_1 dx_2 f_g(x_1) f_g(x_2)(\hat{\sigma}_{\rm res} + \hat{\sigma}_{\rm int}), \tag{77}$$

where $\hat{\sigma}$ denotes the parton-level cross section as a function of the $t\bar{t}$ invariant mass q. Following the results in Refs. [145,146], we have

$$\begin{aligned}\hat{\sigma}_{\rm res} &= \hat{\sigma}_{{\rm res},S} + \hat{\sigma}_{{\rm res},P} \\ &= \frac{3\alpha_s^2 G_F^2 m_t^2 q^4}{4096\pi^3}\left[\beta_t^3\left(\left|\sum\nolimits_{i=2,3}\frac{[{\rm Re}(c_{t,i})]^2\mathcal{A}_1(\frac{q^2}{4m_t^2})}{q^2 - m_i^2 - {\rm i}m_i\Gamma_i}\right|^2\right.\right. \\ &\quad \left. + \left|\sum\nolimits_{i=2,3}\frac{[{\rm Re}(c_{t,i}){\rm Im}(c_{t,i})]\mathcal{B}_1(\frac{q^2}{4m_t^2})}{q^2 - m_i^2 - {\rm i}m_i\Gamma_i}\right|^2\right) \\ &\quad + \beta_t\left(\left|\sum\nolimits_{i=2,3}\frac{[{\rm Re}(c_{t,i}){\rm Im}(c_{t,i})]\mathcal{A}_1(\frac{q^2}{4m_t^2})}{q^2 - m_i^2 - {\rm i}m_i\Gamma_i}\right|^2\right. \\ &\quad \left.\left. + \left|\sum\nolimits_{i=2,3}\frac{[{\rm Im}(c_{t,i})]^2\mathcal{B}_1(\frac{q^2}{4m_t^2})}{q^2 - m_i^2 - {\rm i}m_i\Gamma_i}\right|^2\right)\right], \end{aligned} \tag{78}$$

$$\begin{aligned}\hat{\sigma}_{\rm int} &= \hat{\sigma}_{{\rm int},S} + \hat{\sigma}_{{\rm int},P} \\ &= -\int_{-1}^{1} dc_\theta \frac{\alpha_s G_F m_t^2}{64\sqrt{2}\pi(1-\beta_t^2 c_\theta^2)} \\ &\quad \times {\rm Re}\left[\beta_t^3 \sum_{i=2,3}\frac{[{\rm Re}(c_{t,i})]^2\mathcal{A}_1(\frac{q^2}{4m_t^2})}{q^2 - m_i^2 - {\rm i}m_i\Gamma_i}\right. \\ &\quad \left. + \beta_t \sum_{i=2,3}\frac{[{\rm Im}(c_{t,i})]^2\mathcal{B}_1(\frac{q^2}{4m_t^2})}{q^2 - m_i^2 - {\rm i}m_i\Gamma_i}\right]. \end{aligned} \tag{79}$$

Here, $q^2 = x_1 x_2 s$, $\beta_t = \sqrt{1 - 4m_t^2/q^2}$ is the velocity of the top quark in the $t\bar{t}$ center-of-mass frame. In our numerical study, we set q in the range $m_2 - \Delta' q/2 < q < m_2 + \Delta' q/2$, where we choose the mass window $\Delta' q = 100$ GeV for $m_2 = 500$ GeV. We choose the MSTW2008 PDF [139] as above. We show the cross sections for some benchmark points in both Scenario (a) and Scenario (b) in Table VIII. The numerical results show that, for all benchmark points we consider, the interference with the SM background significantly breaks the resonance structure of $H_{2,3}$ and decreases the cross sections to around (and even below) 0,

TABLE VIII. Cross sections $\delta\sigma_{t\bar{t}}$ at the LHC with $\sqrt{s} = 13$ TeV, fixing $m_2 = 500$ GeV and $\alpha_1 = 0.02$. Further, for the Type II model (denoted as $\delta\sigma_{t\bar{t}}^{\rm II}$) we fix $\alpha_2 = 0.14$, while for the Type III model (denoted as $\delta\sigma_{t\bar{t}}^{\rm III}$) we fix $\alpha_2 = 0.27$. The left table is for Scenario (a), in which we fix $\beta = 0.76$ and choose $\alpha_3 = 0.4,\ 0.8,\ 1.2$ from top to bottom. The right table is for Scenario (b), in which we fix $m_3 = 650$ GeV, considering two cases, $\beta = 0.77$, $\alpha_3 = \alpha_3^+$ and $\beta = 0.885$, $\alpha_3 = \alpha_3^-$, again from top to bottom.

α_3	$\delta\sigma_{t\bar{t}}^{\rm II}$(pb)	$\delta\sigma_{t\bar{t}}^{\rm III}$(pb)
0.4	0.04	−0.40
0.8	0.39	−0.11
1.2	0.25	−0.07

α_3	$\delta\sigma_{t\bar{t}}^{\rm II}$(pb)	$\delta\sigma_{t\bar{t}}^{\rm III}$(pb)
α_3^+	−0.43	−0.67
α_3^-	0.72	0.53

which means that the $t\bar{t}$ resonant search at the LHC cannot set limits on this model.[16]

The $H_{2,3}$ states can also be produced in association with a $t\bar{t}$ pair at the LHC, and thus we should also check this constraint for our favored benchmark points. Since $H_{2,3}$ mainly decay into a $t\bar{t}$ pair, the whole production and decay process will modify the cross section of the $pp \to t\bar{t}t\bar{t}$ process (which we denote by σ_{4t}), whose current LHC limit is about 22.5 fb at 95% C.L. [150] at $\sqrt{s} = 13$ TeV with 137 fb^{-1} of integrated luminosity by the CMS Collaboration.[17] The interference effects between SM and BSM contributions are expected to be significant [152]. We estimate this cross section in the 2HDM considering all interference effects by using MadGraph5_aMC@NLO [153,154]. We show the numerical results in Table IX for some benchmark points, all allowed by current LHC limits.

Finally, we should also check the direct LHC limits on the charged Higgs boson $H^\pm$. As mentioned above, $b \to s\gamma$ decay favors a heavy $H^\pm$ state with mass $m_\pm \gtrsim 600$ GeV [81,84]. For $m_\pm = 600$ GeV, the current LHC limit is about 0.1 pb at 95% C.L. [155,156] at $\sqrt{s} = 13$ with 36 fb^{-1} of luminosity. For large t_β, the interference effect is negligible [157]. However, in the Type II and Type III

[16]In some experimental analyses [148,149], the interference effects between (pseudo)scalar resonance and the SM background were taken into account. Yet, the results cannot be simply rescaled to our *CP*-violating scenario, because the existence of *CP* violation will modify the shape of the $t\bar{t}$ invariant mass compared with the *CP*-conserving case. We still need further studies on such scenarios.

[17]Recently, the ATLAS Collaboration also presented their measurement $\sigma_{4t} = 24^{+7}_{-6}$ fb at $\sqrt{s} = 13$ TeV with 137 fb^{-1} of integrated luminosity [151]. It is consistent with the CMS result and SM prediction within the 2σ level, but the constraint is a bit weaker as $\sigma_{4t} \lesssim 38$ fb at 95% C.L.

TABLE IX. Cross sections σ_{4t} at the LHC with $\sqrt{s} = 13$ TeV, fixing $m_2 = 500$ GeV and $\alpha_1 = 0.02$. Further, for the Type II model (denoted as $\sigma_{4t}^{\rm II}$) we fix $\alpha_2 = 0.14$, while for the Type III model (denoted as $\sigma_{4t}^{\rm III}$) we fix $\alpha_2 = 0.27$. The left table is for Scenario (a), in which we fix $\beta = 0.76$ and choose $\alpha_3 = 0.4$, 0.8, 1.2 from top to bottom. The right table is for Scenario (b), in which we fix $m_3 = 650$ GeV, considering two cases, $\beta = 0.77$, $\alpha_3 = \alpha_3^+$ and $\beta = 0.885$, $\alpha_3 = \alpha_3^-$, again from top to bottom.

α_3	$\sigma_{4t}^{\rm II}$(fb)	$\sigma_{4t}^{\rm III}$(fb)
0.4	19.9	17.9
0.8	20.8	18.7
1.2	20.8	19.3

α_3	$\sigma_{4t}^{\rm II}$(fb)	$\sigma_{4t}^{\rm III}$(fb)
α_3^+	15.9	14.3
α_3^-	10.4	9.4

models with CP violation as considered above, $t_\beta \sim 1$ is favored. For $m_\pm \simeq 600$ GeV, its width $\Gamma_\pm \gtrsim 30$ GeV, which leads to significant interference effects. Again, we estimate the cross section considering all interference effects using MadGraph5_aMC@NLO [153,154]. If we denote by $\delta\sigma_\pm$ the cross section modification (including both the resonant and interference effects) to the SM $t\bar{t}b\bar{b}$ process, our numerical estimation shows that

$$\delta\sigma_\pm = -0.38 \text{ pb} < 0 \tag{80}$$

for $m_\pm = 600$ GeV and $\beta = 0.76$. This means that the interference effect significantly decreases the $H^\pm$ production cross section in this parameter region, and thus the latter is not constrained by current LHC experiments.

D. Summary of collider constraints

The 125 GeV Higgs (H_1) signal strength measurements lead to a constraint $|\alpha_2| \lesssim 0.33$, which depends weakly on β. The LHC direct searches for heavy neutral scalars decaying to the ZZ final state set a stricter constraint $|\alpha_2| \lesssim 0.27$ for $m_2 = 500$ GeV in both Scenarios (a) and (b). When $m_2 \gtrsim$ (550–600) GeV, the constraint from direct searches becomes weaker than that from the global fit of the H_1 signal strengths. In further analysis, we prefer to choose $\alpha_2 = 0.27$, which is the largest allowed value for $m_2 = 500$ GeV.[18] We have also checked the constraints from $t\bar{t}$, $t\bar{t}t\bar{t}$, and charged Higgs boson searches, in which the interference effects are very important. All benchmark points that we have considered are allowed by current LHC measurements. In the remainder of this work, we focus on the phenomenology of CP violation in $t\bar{t}H_1$ associated production. We will instead consider the production and decay phenomenology of the heavy (pseudo)scalars $H_{2,3}$ in a forthcoming paper.

V. LHC PHENOMENOLOGY OF CP VIOLATION IN $t\bar{t}H_1$ PRODUCTION

In this section we study the production of the lightest neutral Higgs boson H_1 in association with a $t\bar{t}$ pair at the LHC. We discuss the phenomenological setup used in our analysis, address the observables that can be used to probe the CP nature of the $t\bar{t}H_1$ coupling (both inclusive and differential), and close the section by demonstrating the sensitivity results for a selected benchmark point for the final state consisting of two charged leptons, $n \geq 4$ jets, and missing transverse energy $E_T^{\rm miss}$ which is associated with neutrinos from W decays.

A. Phenomenological setup

Events are generated at leading order (LO) using MadGraph5_aMC@NLO [153,154]. Cross sections of signal processes are calculated using a UFO model file [159] corresponding to a Type II 2HDM[19] with flavor conservation [160] slightly modified to account for CP-violation effects in vertices involving both the neutral (H_i, with $i = 1, 2, 3$) and charged ($H^\pm$) Higgs boson states. Here, we employ the LO version of the Mmhtlo68cl PDF sets [161]. For both the signal and background processes, we have used the nominal value for the (identical) renormalization and factorization scales to be equal to half the scalar sum of the transverse mass of all final-state particles on an event-by-event basis, i.e.,

$$\mu_R = \mu_F = \frac{1}{2}\sum_{i=1}^{N}\sqrt{m_i^2 + p_{T,i}^2}\,. \tag{81}$$

In the computation of the parton-level cross sections we have employed the G_μ scheme, where the input parameters are G_F, $\alpha_{\rm em}$, and m_Z, the numerical values of which are given by

$$G_F = 1.16639 \times 10^{-5} \text{ GeV}^{-2}, \qquad \alpha_{\rm em}^{-1}(0) = 137,$$
$$\text{and} \quad m_Z = 91.188 \text{ GeV}. \tag{82}$$

The values for m_W and $\sin^2\theta_W$ are computed from the above inputs. For the pole masses of the fermions, we have taken

$$m_t = 172.5 \text{ GeV}, \qquad m_b = 4.7 \text{ GeV}. \tag{83}$$

Uncertainties due to the scale and PDF variations are computed using SysCalc [162]. In order to keep full spin correlations at both the production and decay stages of the

[18]Recently, the CMS Collaboration presented the latest direct constraint on CP violation in the $\tau^+\tau^- H_1$ interaction [158]. They obtained the CP phase $|\arg(c_{\tau,1})| \lesssim 0.6$ at 95% C.L., corresponding to $|\alpha_2| \lesssim 0.6$ in the Type II or III 2HDM with $t_\beta \simeq 1$. This is much weaker than our indirect constraint.

[19]It can also be used for a Type III 2HDM.

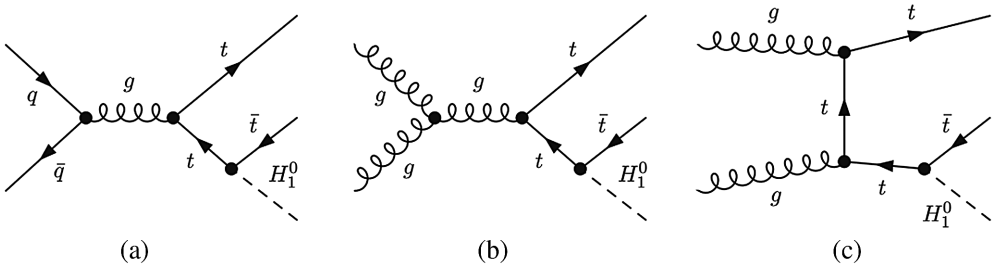

FIG. 11. Representative Feynman diagrams corresponding to $t\bar{t}H_1$ production at LO. They consist of production through (a) $q\bar{q}$ annihilation and (b)–(c) ggF.

top quarks, we have employed MadSpin [163]. PYTHIA8 [164] is used to perform parton showering and hadronization (albeit without including multiple parton interactions) of the events, eventually producing a set of event files in HepMC format [165]. The HepMC files are passed to Rivet (version 2.7.1) [166] for a particle-level analysis. In the latter, jets are clustered using the anti-k_T algorithm using FastJets [167,168].[20]

The particle-level events are selected if they contain two charged leptons, a high jet multiplicity of four to six jets (where at least four of them are b tagged) and missing transverse energy which corresponds to the SM neutrino from the decays of W gauge bosons. Only prompt electrons and muons directly connected to the W boson are accepted, i.e., we do not select those coming from τ decays. Electrons are selected if they pass the basic selection requirement of $p_T^e > 30$ GeV and $|\eta^e| < 2.5$ (excluding the ones that fall in the end-cap or transition regions of the calorimeter, i.e., with $1.37 < |\eta^e| < 1.52$), while muons are selected if they satisfy the conditions $p_T^\mu > 27$ GeV and $|\eta^\mu| < 2.4$. Jets are clustered with jet radius $D = 0.4$ and selected if they satisfy $p_T^j > 30$ GeV and $|\eta^j| < 2.4$. For b tagging, we use the so-called ghost-association technique [175,176]. In this method, a jet is b tagged if all of the jet particles i within $\Delta R(\text{jet}, i) < 0.3$ of a given anti-k_T jet satisfy $p_T^i > 5$ GeV. We assume a b-tagging efficiency of 80% independent of the transverse momentum of the jet. For top-quark reconstruction, we use the PseudoTop definition [177] (more details along with validation plots can be found in Appendix F). Finally, we require that the invariant mass of $b\bar{b}$ system forming the H_1 candidate should be around the H_1 mass, $|m_{b\bar{b}} - m_1| < 15$GeV, and the transverse energy of the $b\bar{b}$ system forming the H_1 candidate is larger than 50 GeV.

B. Inclusive $t\bar{t}H_1$ cross section

The parton-level Feynman diagrams for $t\bar{t}H_1$ production at LO are depicted in Fig. 11. The cross section has two contributions: (i) $q\bar{q}$ annihilation [Fig. 11(a)], which is expected to dominate in the region of medium and large $x = \tilde{p}_i/P$, where $\tilde{p}_i$ and P are the longitudinal momenta of the parton i and the proton, respectively; and (ii) from gg fusion (ggF) [Figs. 11(b)–11(c)], dominating at low x. For the calculation of the cross section, we employ MadGraph5_aMC@NLO [153,154] with the Mmhtlo68cl and Mmhtnlo68cl PDF sets [161] in the four-flavor scheme. Systematic uncertainties are divided into two categories: scale and PDF. The scale uncertainties are obtained by varying the renormalization and factorization scales by a factor of 2 around their nominal value, i.e.,

$$(\mu_R, \mu_F) = \{(1,1),(1,0.5),(1,2),(0.5,1),(0.5,0.5),(0.5,2),(2,1),(2,0.5),(2,2)\}(\mu_R^0, \mu_F^0), \tag{84}$$

with

$$\mu_F^0 = \mu_R^0 = \frac{1}{2}\sum_i \sqrt{p_{T,i}^2 + m_i^2}\,. \tag{85}$$

Furthermore, PDF uncertainties are estimated using the Hessian method [178].

In Table X we show the results of the cross section both at both LO and next-to-leading order (NLO) in the SM. We can see that the NLO corrections imply a K-factor of about 1.17 in the case when no cuts are applied on the Higgs boson transverse momentum and for the case where $p_T^H > 50$ GeV. The K-factor slightly increases to 1.25 when a more stringent cut ($p_T^H > 200$ GeV) is applied. Furthermore, the theoretical uncertainties are dominated by those associated with scale variations, which significantly decrease when we go from LO to NLO. PDF uncertainties are subleading and mildly dependent on the Higgs p_T cut. Finally, we notice that the ggF contribution is dominant, accounting for ≃68 (≃71.5%) at LO (NLO) of the total cross section in the case with $p_T^H > 50$ GeV, and slightly decreasing to ≃59% (≃67%) for the $p_T^H > 200$ GeV case.

In the complex 2HDM, the $t\bar{t}H_1$ coupling is given by

$$\mathcal{L}_{t\bar{t}H_1} = -\frac{m_t}{v}(c_{t,1}\bar{t}_L t_R H_1 + \text{H.c.}), \tag{86}$$

where $c_{t,1} = c_{\alpha_2} s_{\beta+\alpha_1}/s_\beta - \mathrm{i} s_{\alpha_2}/t_\beta$ is the $t\bar{t}H_1$ coupling modifier which is independent on the Yukawa realization of

[20]Results were found to be stable when we replaced PYTHIA8 with HERWIG6.5 [169–172] and the anti-k_T algorithm with the Cambridge-Aachen one [173,174].

TABLE X. Parton-level cross sections for the production of $t\bar{t}H_1$ final states at the LHC at LO and NLO. The results are shown along with the theoretical uncertainties due to scale variations (first errors) and PDF uncertainties (second errors). The cross sections were computed for the cases of no cuts on the Higgs boson p_T (first row), for $p_T^H > 50$ GeV (second row), and for $p_T^H > 200$ GeV (third row).

	$\sigma_{\rm LO}$ [fb]	$\sigma_{\rm NLO}$ [fb]
No cuts	$398.9^{+32.7\%}_{-22.9\%}(\text{scale})^{+1.91\%}_{-1.54\%}(\text{PDF})$	$470.6^{+5.8\%}_{-9.0\%}(\text{scale})^{+2.2\%}_{-2.1\%}(\text{PDF})$
$p_T^H > 50$ GeV	$325.2^{+32.8\%}_{-22.9\%}(\text{scale})^{+1.96\%}_{-1.56\%}(\text{PDF})$	$382.8^{+5.4\%}_{-8.8\%}(\text{scale})^{+2.3\%}_{-2.1\%}(\text{PDF})$
$p_T^H > 200$ GeV	$55.6^{+33.9\%}_{-23.5\%}(\text{scale})^{+2.44\%}_{-1.81\%}(\text{PDF})$	$69.8^{+8.3\%}_{-10.6\%}(\text{scale})^{+2.9\%}_{-2.6\%}(\text{PDF})$

the 2HDM. The $t\bar{t}H_1$ production cross section behaves as shown in Eq. (62). The presence of the pseudoscalar part in the $t\bar{t}H_1$ coupling can drastically changes the value of the cross section, as can be seen in Fig. 12.

C. *CP*-violation observables in the $t\bar{t}H_1$ channel

In this section we give an overview of the different observables that we have used in this study to pin down the spin and *CP* properties of the SM-like Higgs boson produced in association with a $t\bar{t}$ pair.

First, one can directly study the spin-spin correlations of the $t\bar{t}$ pair by measuring the differential distribution in $\cos\theta_{\ell^a}\cos\theta_{\ell^b}$ of the emerging leptons,

$$\frac{1}{\sigma}\frac{\mathrm{d}^2\sigma}{\mathrm{d}\cos\theta_{\ell^a}\mathrm{d}\cos\theta_{\ell^b}} = \frac{1}{4}(1+\alpha_{\ell^a}P_a\cos\theta_{\ell^a}+\alpha_{\ell^b}P_b\cos\theta_{\ell^b} + \alpha_{\ell^a}\alpha_{\ell^b}C_{ab}\cos\theta_{\ell^a}\cos\theta_{\ell^b}), \quad (87)$$

where α_ℓ is the spin-analyzing power of the charged lepton and $\theta_{\ell^{a,b}} = \measuredangle(\hat{\ell}^{a,b}, \hat{S}_{a,b})$, where $\hat{\ell}^{a,b}$ is the direction of flight of the charged lepton in the top-quark rest frame and $\hat{S}_{a,b}$ is the spin quantization axis in the basis a. Furthermore, C_{ab} is the correlation coefficient which is related to the expectation value of $\cos\theta_{\ell^a}\cos\theta_{\ell^b}$ using Eq. (87). In the following, we consider three different bases: the helicity basis ($a = k$), the transverse basis ($a = n$), and the r basis; see, e.g., Refs. [19,179] for more details about the definitions of the spin bases and Refs. [180,181] for reported measurements of these observables in $t\bar{t}$ production. It was found that the $t\bar{t}$ spin-spin correlations in the transverse and r bases are good probes of *CP* violation, e.g., through the anomalous chromomagnetic and chromoelectric top-quark couplings [179].[21]

Furthermore, we consider the opening angle between the two oppositely charged leptons produced in the decays of the top (anti)quarks, which is defined by

$$\cos\varphi_{\ell_a\ell_b} = \frac{\hat{p}_{\ell^+}\cdot\hat{p}_{\ell^-}}{|\hat{p}_{\ell^+}||\hat{p}_{\ell^-}|}, \quad (88)$$

where $\hat{p}_{\ell^+}$ ($\hat{p}_{\ell^-}$) is the direction of the flight of the charged lepton ℓ^+ (ℓ^-) in the parent top (anti)quark rest frame.

The azimuthal angle $\Delta\phi_{\ell^+\ell^-} = |\phi_{\ell^+} - \phi_{\ell^-}|$ is a clean observable to measure the spin-spin correlations between the top and antitop quarks. The momenta of the charged leptons are usually measured in the laboratory frame [182,183]. This observable shows a high sensitivity to the degree of correlations between the top (anti)quarks in $t\bar{t}$ production. However, since we are considering the $t\bar{t}H_1$ production mode, the presence of the Higgs boson may wash out the sensitivity of $\Delta\phi$ to the correlations, though we have not found this to be the case.

In addition to the aforementioned observables, we also study the sensitivity of the following angle [22]:

$$\cos\theta_{\ell H_1} = \frac{(\hat{p}_{\ell^+}\times\hat{p}_{H_1})\cdot(\hat{p}_{\ell^-}\times\hat{p}_{H_1})}{|(\hat{p}_{\ell^+}\times\hat{p}_{H_1})||(\hat{p}_{\ell^-}\times\hat{p}_{H_1})|}, \quad (89)$$

where $\hat{p}_{\ell^+}$, $\hat{p}_{\ell^-}$, and $\hat{p}_{H_1}$ are the directions of flight of the positively and negatively charged leptons and the reconstructed Higgs boson in the laboratory frame. The $\theta_{\ell H_1}$ angle defines the angle spanned by the charged lepton momenta projected onto the plane perpendicular to the Higgs boson's direction of flight. This observable can be redefined to yield better dependence on the *CP*-violating effects in the $t\bar{t}H_1$ coupling. We define the new observable as

$$\cos\tilde{\theta}_{\ell H_1} = \lambda\cos\theta_{\ell H_1}, \quad (90)$$

with $\lambda = \mathrm{sign}((\vec{p}_b - \vec{p}_{\bar{b}})\cdot(\vec{p}_{\ell^-}\times\vec{p}_{\ell^+}))$.

One can obtain the polarization of the (anti)top quark by integrating Eq. (87) over the angle θ_ℓ^a (or θ_ℓ^b),

$$\frac{1}{\sigma}\frac{\mathrm{d}\sigma}{\mathrm{d}\cos\theta^a_{\ell^\pm}} = \frac{1}{2}(1+\alpha_{\ell^\pm}P^a_{t,\bar{t}}\cos\theta^a_{\ell^\pm}), \quad (91)$$

which applies to all of the spin quantization axes used here.

It was also found that the energy distributions of the top-quark decay products carry some information on the polarization state of the top (anti)quark [184–192]. We follow the same definitions used in Refs. [186,188] and

[21] In $t\bar{t}H_1$ production, the contribution of ggF is about 70% of the total cross section. Hence, the initial state is mostly Bose symmetric. Following the recommendations of Ref. [179], the value of $\cos\theta_\ell$ is multiplied by the sign of the scattering angle $\vartheta = \hat{\mathbf{p}}\cdot\hat{\mathbf{p}}_t$, where $\hat{\mathbf{p}}_t = \mathbf{p}_t/|\mathbf{p}_t|$ is the top-quark direction of flight in the $t\bar{t}$ rest frame and $\hat{\mathbf{p}} = (0,0,1)$.

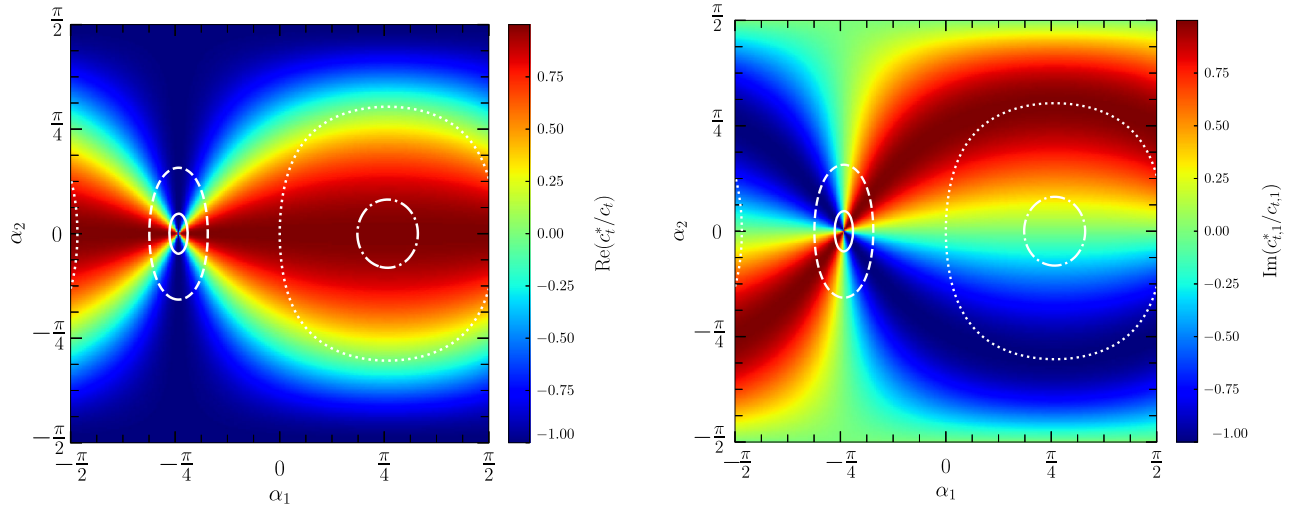

FIG. 12. The real (left) and imaginary (right) parts of the ratio $c_{t,1}^*/c_{t,1}$ projected on the mixing angles α_1 and α_2 upon fixing $\beta = 0.76$. The solid, dashed, dotted, and dot-dashed lines show the contours where $\sigma_{\mathrm{2HDM}}(pp \to t\bar{t}H_1)/\sigma_{\mathrm{SM}}(pp \to t\bar{t}H_1)$ is 0.01,0.1,1, and 2, respectively.

study the ratios of the different energies. We give the first two observables as follows:

$$u = \frac{E_\ell}{E_\ell + E_b}, \qquad z = \frac{E_b}{E_t}, \tag{92}$$

where E_ℓ, E_b, and E_t are the energies of the charged lepton, b jet, and top quark in the laboratory frame. Finally, we consider the energy of the charged leptons in the laboratory frame,

$$x_\ell = \frac{2E_\ell}{m_t}, \tag{93}$$

where $m_t = 172.5$ GeV is the pole mass of the top quark.

We complement this analysis by including the sensitivity of some laboratory-frame observables introduced in Ref. [30]. We found that the observable denoted by ω_6 has a higher sensitivity than the others (defined in Ref. [30] by $\omega_{b,\ell}^{X,Y}$). We define this angle as

$$\cos\omega_6 = \frac{[(\vec{p}_{\ell^-} \times \vec{p}_{\ell^+}) \cdot (\vec{p}_b + \vec{p}_{\bar{b}})][(\vec{p}_{\ell^-} - \vec{p}_{\ell^+}) \cdot (\vec{p}_b + \vec{p}_{\bar{b}})]}{|\vec{p}_{\ell^-} \times \vec{p}_{\ell^+}||\vec{p}_b + \vec{p}_{\bar{b}}||\vec{p}_{\ell^-} - \vec{p}_{\ell^+}||\vec{p}_b + \vec{p}_{\bar{b}}|}. \tag{94}$$

In Fig. 13 we show some observables used in our analysis for the $t\bar{t}H$ in the SM, and in the 2HDM with $\alpha_2 = 0.27$ (green) and $\alpha_2 = \pi/2$. The latter case is shown for comparison only. We can see from Fig. 13 that the shapes of all of these observables are slightly changed as we go from the SM to the 2HDM with $\alpha_2 = 0.27$. The only difference between the two cases resides in the total normalization, which depends on the cross section.

D. Results

In this subsection we show the results of the sensitivity of the observables defined in the previous section. In order to quantify the sensitivity of the various spin observables to the benchmark points, we compute forward-backward asymmetries. An asymmetry $\mathcal{A}_\mathcal{O}$ on the observable $\mathcal{O}$ is defined as

$$\mathcal{A}_\mathcal{O} = \frac{N(\mathcal{O} > \mathcal{O}_c) - N(\mathcal{O} < \mathcal{O}_c)}{N(\mathcal{O} > \mathcal{O}_c) + N(\mathcal{O} < \mathcal{O}_c)} \equiv \frac{N^+ - N^-}{N^+ + N^-}, \tag{95}$$

where $\mathcal{O}_c$ is a reference point for the observable $\mathcal{O}$ with respect to which the asymmetry is evaluated. For the observable $|\Delta\phi_{\ell^+\ell^-}|$, we choose $\mathcal{O}_c = \pi/2$. While for other angular (energy) observables, we choose $\mathcal{O}_c = 0$ ($\mathcal{O}_c = 0.5$).

To quantify deviations from the SM expectations, we compute the χ^2 as

$$\chi^2 = \frac{(\mathcal{A}_\mathcal{O} - \mathcal{A}_\mathcal{O}^{\mathrm{SM}})^2}{\sigma_\mathcal{O}^2}, \tag{96}$$

where $\sigma_\mathcal{O}$ is the uncertainty on the measurement of the asymmetry in the SM. We assume that the N^+ and N^- are correlated, i.e., measured in the same run of an experiment. In this case, the uncertainty on the asymmetry is given by

$$\sigma_\mathcal{O}^2 = \frac{4N^+N^-}{N^3}, \tag{97}$$

where $N = A \times \epsilon\sigma \times \mathcal{L}$. Here, $A \times \epsilon$ is the acceptance times the efficiency of the signal process after full selection, and σ is the cross section times the BRs, i.e.,

$$\sigma = \sigma(t\bar{t}H_1) \times \mathrm{BR}(H_1 \to b\bar{b}) \times \mathrm{BR}(t \to b\ell\nu)^2. \tag{98}$$

In Table XI we show the expected deviations from the SM expectation at $\mathcal{L} = 3000$ fb^{-1}.

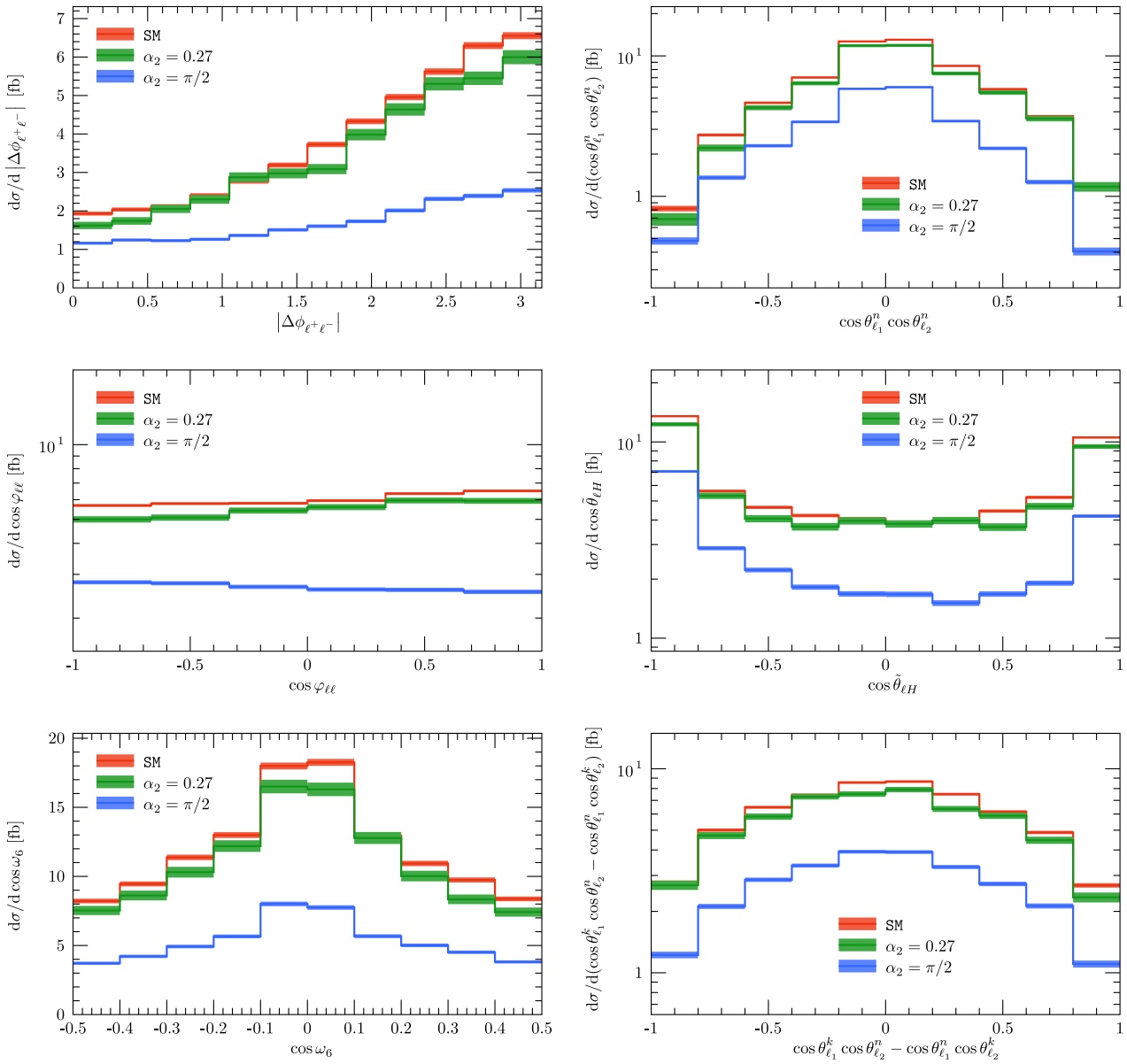

FIG. 13. Differential distributions for some selected observables. Top panels: the differential cross section versus $|\Delta\phi_{\ell^+\ell^-}|$ (left) in the laboratory frame and versus $\cos\theta^n_\ell \cos\theta^n_\ell$ (right), where $\cos\theta_\ell$ is defined in the top-quark rest frame. Middle panels: the differential cross sections versus the cosine of the opening angle between the two charged leptons' direction of flight (left) and versus $\cos\tilde{\theta}_{\ell H}$ (right). Bottom panels: the differential cross section as a function of $\cos\omega_6$ (left) and as a function of the antisymmetric combination of $\cos\theta^k_\ell \cos\theta^n_\ell$ (right). Red lines are for the SM, blue lines are for the signal benchmark point with $\alpha_2 = 0.27$, and green lines are for the pure pseudoscalar case $\alpha_2 = \pi/2$ as a comparison, which is of course excluded. The differential distributions are normalized to their total cross sections.

We can see that, for $\alpha_2 = 0.27$, the χ^2 can be larger than 1 for seven observables: $\cos\varphi_{\ell\ell}, x_\ell, c^k_\ell c^n_\ell - c^n_\ell c^k_\ell, c^r_\ell c^n_\ell - c^n_\ell c^r_\ell$, $|\Delta\phi_{\ell^+\ell^-}|, \cos\tilde{\theta}_{\ell H}$, and $\cos\omega_6$. After combining all of the observables in Table XI, the χ^2 can reach about 19.2. However, the naive χ^2 combination may become obsolete, or misleading. In order to improve this combination, we compute the p-value, given by

$$p = \int_{\chi^2_{\min}}^{\infty} f(x, N_{\text{d.o.f.}})\mathrm{d}x, \tag{99}$$

where $f(x, N_{\text{d.o.f.}})$ is the χ^2 probability distribution function for $N_{\text{d.o.f.}}$ degrees of freedom,[22] and $\chi^2_{\min} \equiv \chi^2_{\alpha_2=0.27}$. The p-value quantifies to what extent the null hypothesis (SM CP-conserving case) is excluded. p-values smaller than 0.05 imply that the null hypothesis is excluded. We show the p-value as a function of α_2 in Table XI. In Table XI, the

[22]The number of degrees of freedom ($N_{\text{d.o.f.}}$) is the number of observables used in the fit minus the number of free parameters (i.e., here we have one free parameter, α_2).

TABLE XI. The asymmetries for the SM and 2HDM with $\alpha_2 = 0.27$. The values of χ^2 quantifying the deviations from the SM expectations are shown in the fourth column. The p-values for different asymmetries [defined in Eq. (99)] are given in the fifth column. The computations are performed for an integrated luminosity of 3000 fb^{-1}. The shorthand notations $c^r_{\ell^+} = \cos\theta^k_{\ell^+}, \cdots$ are used. Details about the calculations are discussed in the text.

Observable	$\mathcal{A}_{\mathrm{SM}}$	$\mathcal{A}_{\alpha_2=0.27}$	χ^2	p-value
Polarization observables				
$\cos\theta^k_\ell$	4.12×10^{-3}	5.32×10^{-3}	6.34×10^{-3}	0.937
$\cos\theta^n_\ell$	4.74×10^{-3}	4.79×10^{-3}	8.34×10^{-6}	0.997
$\cos\theta^r_\ell$	-6.54×10^{-4}	-9.31×10^{-3}	0.33	0.565
$\cos\varphi_{\ell\ell}$	3.77×10^{-2}	6.01×10^{-2}	2.21	0.136
u	0.232	0.237	0.10	0.751
x_ℓ	−0.832	−0.822	1.26	0.259
z	−0.387	−0.401	0.93	0.332
`Combined`				6.19×10^{-2}
Spin-spin correlation observables				
$\cos\theta_{\ell H}$	-7.84×10^{-2}	-6.68×10^{-2}	0.59	0.43
$\cos\theta^k_\ell \cos\theta^k_\ell$	6.79×10^{-3}	1.49×10^{-2}	0.28	0.59
$\cos\theta^n_\ell \cos\theta^n_\ell$	7.09×10^{-2}	7.69×10^{-2}	0.15	0.69
$\cos\theta^r_\ell \cos\theta^r_\ell$	2.98×10^{-2}	3.01×10^{-2}	1.74×10^{-4}	0.98
$c^k_\ell c^n_\ell - c^n_\ell c^k_\ell$	-8.16×10^{-3}	1.22×10^{-2}	1.83	0.17
$c^k_\ell c^n_\ell + c^n_\ell c^k_\ell$	-6.28×10^{-3}	-1.97×10^{-2}	0.79	0.37
$c^k_\ell c^r_\ell - c^r_\ell c^k_\ell$	3.15×10^{-3}	-7.98×10^{-3}	0.54	0.46
$c^k_\ell c^r_\ell + c^k_\ell c^k_\ell$	-3.25×10^{-2}	-3.99×10^{-2}	0.24	0.62
$c^r_\ell c^n_\ell - c^n_\ell c^r_\ell$	-8.88×10^{-4}	-1.73×10^{-2}	1.18	0.27
$c^r_\ell c^n_\ell + c^n_\ell c^r_\ell$	-2.53×10^{-3}	9.31×10^{-3}	0.61	0.43
$\lvert\Delta\phi_{\ell^+\ell^-}\rvert$	0.39	0.35	5.81	1.59×10^{-2}
`Combined`				1.21×10^{-2}
CP-odd laboratory-frame observables				
$\cos\tilde{\theta}_{\ell H}$	-1.2×10^{-2}	3.99×10^{-3}	1.14	0.28
$\cos\omega_6$	-6.11×10^{-3}	1.38×10^{-2}	1.75	0.18
`Combined`				8.89×10^{-2}
All combinations				1.87×10^{-2}

label `Combined` refers to the combination of different asymmetries for each category when removing observables with $\chi^2 < 1$: (i) in the polarization observables, `Combined` refers to the combination of $\cos\varphi_{\ell\ell}$ and x_ℓ, (ii) while in the spin-spin correlation observables, `Combined` refers to the combination of $c^k_\ell c^n_\ell - c^n_\ell c^k_\ell$, $c^r_\ell c^n_\ell - c^n_\ell c^r_\ell$, and $|\Delta\phi_{\ell^+\ell^-}|$. We can see the important role played by the spin-spin correlations asymmetries, for which the p-value is about 1.59×10^{-2}. The results depends weakly on β and α_1 in our favored region ($t_\beta \sim 1$ and $\alpha_1 \sim 0$) because the observables are sensitive only to the $t\bar{t}H_1$ *CP*-violating phase $\simeq s_{\alpha_2}/t_\beta$ in this region. It is worth mentioning that the results can be further improved by using different approaches. On the one hand, the weighted fits (as used in Ref. [30]) may improve the results since another important factor that we did not take advantage of is the total cross section for a given value of α_2. On the other hand, methods based on machine learning may play an important role in the determination of the maximum allowed *CP*-violating phase in the $t\bar{t}H_1$ coupling [193].

VI. CONCLUSIONS

In this work we have analyzed soft *CP*-violating effects in both EDMs and LHC phenomenology in a 2HDM with soft *CP* violation. In this scenario, the mixing angle α_2 is the key parameter measuring the size of *CP* violation since the *CP*-violating phases in $H_1 f\bar{f}$ Yukawa vertices are proportional to s_{α_2}.

We have considered all four standard types of Yukawa couplings—named Type I–IV models—in our analysis. In Type I and IV models there is no cancellation mechanism in electron EDM calculations, leading to a very strict constraint on the *CP*-violating phase $|\arg c_{t/\tau,1}| \lesssim 8.2 \times 10^{-4}$, which renders all *CP*-violating effects unobservable in further collider studies for these two models.

For Type II and III models we have discussed two scenarios: (a) $H_{2,3}$ are close in mass while α_3 is away from 0 or $\pi/2$, and (b) $H_{2,3}$ have a large mass splitting while α_3 must be close to 0 or $\pi/2$. The cancellation behavior in the electron EDM leads to a larger allowed region for α_2 in both scenarios. In these two models, t_β is favored to be

close to 1, whose location depends weakly on the masses of the heavy (pseudo)scalars, with a strong correlation with α_1. The electron EDM alone cannot set constraints on α_2 directly. In the Type II model, $|\alpha_2| \lesssim 0.09$ is estimated from the neutron EDM constraint if we consider only the central value estimation, and this constraint can be as weak as $\lesssim 0.15$ if the theoretical uncertainty in neutron EDM estimation is also considered. In the Type III model, no constraint can be drawn from the neutron EDM and $|\alpha_2| \lesssim 0.27$ is estimated from LHC constraints if $m_2 \simeq 500$ GeV. Such results mean that in Type III models [for both Scenarios (a) and (b)] the CP-violation phase $|\arg(c_{t,1})| \simeq |s_{\alpha_2}/t_\beta|$ can reach as large as $\simeq 0.28$, which leads us to consider further phenomenology of the model. This result is independent of α_3, and depends weakly on α_1 in its allowed region (close to zero). Other LHC direct searches do not set further limits for the 2HDM.

Our analysis shows the importance of further neutron EDM measurements to an accuracy of $\mathcal{O}(10^{-27}\ e \cdot \mathrm{cm})$. An α_2 with a value $\sim\mathcal{O}(0.1)$ will lead to significant nonzero results in such experiments. If CP violation in the Higgs sector exists, as we have discussed, the first evidence of it is expected to appear in the neutron EDM measurements. Conversely, if there is still a null result for the neutron EDM, direct constraints on $|\alpha_2|$ can be pushed to about 4×10^{-3} in the Type II model and 2×10^{-2} in the Type III model. Such a strict constraint can exclude the Type II model as an explanation of the matter-antimatter asymmetry in the Universe. Thus, we conclude that, for models in which a cancellation mechanism can appear in the electron EDM, the neutron EDM measurements are good supplements to finding evidence of CP violation or setting constraints on the CP-violating angle directly.

We have also performed a phenomenological study of soft CP violation in the 2HDM for the case of $t\bar{t}H_1$ associated production at the LHC with a luminosity of 3000 fb^{-1}. With fixed β and $\alpha_{1,2}$, its properties are independent of the mixing angle α_3 and the masses of the heavy (pseudo)scalars $H_{2,3}$ and $H^\pm$. Upon choosing the benchmark point $\beta = 0.76$, $\alpha_1 = 0.02$, and $\alpha_2 = 0.27$ [corresponding to the case $m_{2,3} \simeq 500$ GeV with the maximal CP-violation phase $\arg(c_{t,1}) \simeq 0.28$ in the Type III model], we constructed top (anti)quark spin-dependent observables and tested their deviations from the SM. Among these, the azimuthal angle between the two leptons from fully leptonic $t\bar{t}$ decays, $\Delta\phi_{\ell^+\ell^-}$, is the most sensitive observable, with $\chi^2 = 5.81$. On the other hand, by combining asymmetries constructed from seven spin-dependent observables, we found that the p-value is about 1.87×10^{-2}, meaning that the null hypothesis (the CP-conserving case) can be excluded by the use of these observables and one can probe the maximum allowed CP-violating phase in the $t\bar{t}H_1$ coupling obtained for $\alpha_2 = 0.27$. Thus, the LHC experiments can provide a complementary cross-check of the EDM results.

Finally, we note that we did not perform a phenomenological study of the heavy (pseudo)scalars ($H_{2,3}$ or $H^\pm$) in this paper. In this case, interference effects with the SM backgrounds may become very important and thus a dedicated treatment is needed, which we postpone to a forthcoming paper.

ACKNOWLEDGMENTS

We thank Abdesslam Arhrib, Jianqi Chen, Nodoka Yamanaka, Fa Peng Huang, Qi-Shu Yan, Hao Zhang, and Shou-hua Zhu for helpful discussion. We also thank Abdesslam Arhrib for collaboration at the beginning of this project. The work of K. C. and Y. N. M. was supported in part by the MoST of Taiwan under Grant No. 107-2112-M-007-029-MY3. The work of A. J. was supported by the National Research Foundation of Korea under Grant No. NRF-2019R1A2C1009419. A. J. would like to thank the CERN Theory Department and the HECAP Section of the Abdus Salam International Centre for Theoretical Physics for their hospitality where part of this work was done. S. M. is supported in part through the NExT Institute and the STFC CG ST/L000296/1 award.

APPENDIX A: YUKAWA COUPLINGS

Following the parametrization in Eq. (18), we list the Yukawa couplings in the mass eigenstate basis explicitly [78–80] in terms of the mixing angles $\beta, \alpha_{1,2,3}$. By denoting the Yukawa coupling $c_{f,i}$ in the Type X 2HDM (X = I–IV) as $c^X_{f,i}$, we have the following:

$$c^{\mathrm{I\text{–}IV}}_{U_i,1} = \frac{c_{\alpha_2} s_{\beta+\alpha_1}}{s_\beta} - \mathrm{i}\frac{s_{\alpha_2}}{t_\beta}, \tag{A1}$$

$$c^{\mathrm{I\text{–}IV}}_{U_i,2} = \frac{c_{\beta+\alpha_1} c_{\alpha_3} - s_{\beta+\alpha_1} s_{\alpha_2} s_{\alpha_3}}{s_\beta} - \mathrm{i}\frac{c_{\alpha_2} s_{\alpha_3}}{t_\beta}, \tag{A2}$$

$$c^{\mathrm{I\text{–}IV}}_{U_i,3} = -\frac{c_{\beta+\alpha_1} s_{\alpha_3} + s_{\beta+\alpha_1} s_{\alpha_2} c_{\alpha_3}}{s_\beta} - \mathrm{i}\frac{c_{\alpha_2} c_{\alpha_3}}{t_\beta}, \tag{A3}$$

$$\begin{aligned} c^{\mathrm{I,III}}_{D_i,1} &= \frac{c_{\alpha_2} s_{\beta+\alpha_1}}{s_\beta} + \mathrm{i}\frac{s_{\alpha_2}}{t_\beta}, \\ c^{\mathrm{II,IV}}_{D_i,1} &= \frac{c_{\alpha_2} c_{\beta+\alpha_1}}{c_\beta} - \mathrm{i} s_{\alpha_2} t_\beta, \end{aligned} \tag{A4}$$

$$\begin{aligned} c^{\mathrm{I,III}}_{D_i,2} &= \frac{c_{\beta+\alpha_1} c_{\alpha_3} - s_{\beta+\alpha_1} s_{\alpha_2} s_{\alpha_3}}{s_\beta} + \mathrm{i}\frac{c_{\alpha_2} s_{\alpha_3}}{t_\beta}, \\ c^{\mathrm{II,IV}}_{D_i,2} &= -\frac{s_{\beta+\alpha_1} c_{\alpha_3} + c_{\beta+\alpha_1} s_{\alpha_2} s_{\alpha_3}}{c_\beta} - \mathrm{i} c_{\alpha_2} s_{\alpha_3} t_\beta, \end{aligned} \tag{A5}$$

$$\begin{aligned} c^{\mathrm{I,III}}_{D_i,3} &= -\frac{c_{\beta+\alpha_1} s_{\alpha_3} + s_{\beta+\alpha_1} s_{\alpha_2} c_{\alpha_3}}{s_\beta} + \mathrm{i}\frac{c_{\alpha_2} c_{\alpha_3}}{t_\beta}, \\ c^{\mathrm{II,IV}}_{D_i,3} &= \frac{s_{\beta+\alpha_1} s_{\alpha_3} - c_{\beta+\alpha_1} s_{\alpha_2} c_{\alpha_3}}{c_\beta} - \mathrm{i} c_{\alpha_2} c_{\alpha_3} t_\beta, \end{aligned} \tag{A6}$$

$$c_{\ell_i,1}^{\mathrm{I,IV}} = \frac{c_{\alpha_2} s_{\beta+\alpha_1}}{s_\beta} + \mathrm{i}\frac{s_{\alpha_2}}{t_\beta},$$
$$c_{\ell_i,1}^{\mathrm{II,III}} = \frac{c_{\alpha_2} c_{\beta+\alpha_1}}{c_\beta} - \mathrm{i} s_{\alpha_2} t_\beta, \tag{A7}$$

$$c_{\ell_i,2}^{\mathrm{I,IV}} = \frac{c_{\beta+\alpha_1} c_{\alpha_3} - s_{\beta+\alpha_1} s_{\alpha_2} s_{\alpha_3}}{s_\beta} + \mathrm{i}\frac{c_{\alpha_2} s_{\alpha_3}}{t_\beta},$$
$$c_{\ell_i,2}^{\mathrm{II,III}} = -\frac{s_{\beta+\alpha_1} c_{\alpha_3} + c_{\beta+\alpha_1} s_{\alpha_2} s_{\alpha_3}}{c_\beta} - \mathrm{i} c_{\alpha_2} s_{\alpha_3} t_\beta, \tag{A8}$$

$$c_{\ell_i,3}^{\mathrm{I,IV}} = -\frac{c_{\beta+\alpha_1} s_{\alpha_3} + s_{\beta+\alpha_1} s_{\alpha_2} c_{\alpha_3}}{s_\beta} + \mathrm{i}\frac{c_{\alpha_2} c_{\alpha_3}}{t_\beta},$$
$$c_{\ell_i,3}^{\mathrm{II,III}} = \frac{s_{\beta+\alpha_1} s_{\alpha_3} - c_{\beta+\alpha_1} s_{\alpha_2} c_{\alpha_3}}{c_\beta} - \mathrm{i} c_{\alpha_2} c_{\alpha_3} t_\beta. \tag{A9}$$

APPENDIX B: SCALAR COUPLINGS

The scalar couplings in the potential can be expressed using the physical parameters as [78–80]

$$\lambda_1 = \frac{1}{c_\beta^2 v^2}[c_{\beta+\alpha_1}^2 c_{\alpha_2}^2 m_1^2 + (c_{\beta+\alpha_1} s_{\alpha_2} s_{\alpha_3} + s_{\beta+\alpha_1} c_{\alpha_3})^2 m_2^2 + (c_{\beta+\alpha_1} s_{\alpha_2} c_{\alpha_3} - s_{\beta+\alpha_1} s_{\alpha_3})^2 m_3^2 - s_\beta^2 \mu^2], \tag{B1}$$

$$\lambda_2 = \frac{1}{s_\beta^2 v^2}[s_{\beta+\alpha_1}^2 c_{\alpha_2}^2 m_1^2 + (c_{\beta+\alpha_1} c_{\alpha_3} - s_{\beta+\alpha_1} s_{\alpha_2} s_{\alpha_3})^2 m_2^2 + (s_{\beta+\alpha_1} s_{\alpha_2} c_{\alpha_3} + c_{\beta+\alpha_1} s_{\alpha_3})^2 m_3^2 - c_\beta^2 \mu^2], \tag{B2}$$

$$\lambda_3 = \frac{1}{s_{2\beta} v^2}[s_{2(\beta+\alpha_1)}(c_{\alpha_2}^2 m_1^2 + (s_{\alpha_2}^2 s_{\alpha_3}^2 - c_{\alpha_3}^2) m_2^2 + (s_{\alpha_2}^2 c_{\alpha_3}^2 - s_{\alpha_3}^2) m_3^2) + s_{\alpha_2} s_{2\alpha_3} c_{2(\beta+\alpha_1)}(m_3^2 - m_2^2)] + \frac{2m_\pm^2 - \mu^2}{v^2}, \tag{B3}$$

$$\lambda_4 = \frac{1}{v^2}(s_{\alpha_2}^2 m_1^2 + c_{\alpha_2}^2 s_{\alpha_3}^2 m_2^2 + c_{\alpha_2}^2 c_{\alpha_3}^2 m_3^2 + \mu^2 - 2m_\pm^2), \tag{B4}$$

$$\lambda_5 = \frac{1}{v^2}(\mu^2 - s_{\alpha_2}^2 m_1^2 - c_{\alpha_2}^2 s_{\alpha_3}^2 m_2^2 - c_{\alpha_2}^2 c_{\alpha_3}^2 m_3^2) - \frac{\mathrm{i}}{s_{2\beta} v^2}[c_\beta(c_{\beta+\alpha_1} s_{2\alpha_2} m_1^2 - (c_{\beta+\alpha_1} s_{2\alpha_2} s_{\alpha_3}^2 + s_{\beta+\alpha_1} c_{\alpha_2} s_{2\alpha_3}) m_2^2 + (s_{\beta+\alpha_1} c_{\alpha_2} s_{2\alpha_3} - c_{\beta+\alpha_1} s_{2\alpha_2} c_{\alpha_3}^2) m_3^2) + s_\beta(s_{\beta+\alpha_1} s_{2\alpha_2} m_1^2 + (c_{\beta+\alpha_1} c_{\alpha_2} s_{2\alpha_3} - s_{\beta+\alpha_1} s_{2\alpha_2} s_{\alpha_3}^2) m_2^2 - (c_{\beta+\alpha_1} c_{\alpha_2} s_{2\alpha_3} + s_{\beta+\alpha_1} s_{2\alpha_2} c_{\alpha_3}^2) m_3^2)]. \tag{B5}$$

By considering the-bounded-from-below conditions as [51]

$$\lambda_1 > 0, \qquad \lambda_2 > 0, \qquad \lambda_3 > -\sqrt{\lambda_1 \lambda_2}, \qquad \lambda_3 + \lambda_4 - |\lambda_5| > -\sqrt{\lambda_1 \lambda_2}, \tag{B6}$$

$\mu^2 \lesssim (450\ \mathrm{GeV})^2$ is favored and thus we choose $\mu^2 = (450\ \mathrm{GeV})^2$ in the analysis.

The couplings between neutral and charged scalars $c_{i,\pm}$ are [80]

$$c_{i,\pm} = c_\beta(s_\beta^2(\lambda_1 - \lambda_4 - \mathrm{Re}(\lambda_5)) + c_\beta^2 \lambda_3) R_{i1} + s_\beta(c_\beta^2(\lambda_2 - \lambda_4 - \mathrm{Re}(\lambda_5)) + s_\beta^2 \lambda_3) R_{i2} + s_\beta c_\beta \mathrm{Im}(\lambda_5) R_{i3}, \tag{B7}$$

where R is the matrix in Eq. (11). These couplings are useful in the calculations of fermionic EDMs from the contribution of a charged Higgs boson.

APPENDIX C: LOOP INTEGRATIONS FOR EDMS

The loop functions in the calculation of the Barr-Zee diagrams are [53–55,57–59,63]

$$f(z) = \frac{z}{2}\int_0^1 dx \frac{1 - 2x(1-x)}{x(1-x) - z} \ln\left(\frac{x(1-x)}{z}\right), \tag{C1}$$

$$g(z) = \frac{z}{2}\int_0^1 dx \frac{1}{x(1-x) - z} \ln\left(\frac{x(1-x)}{z}\right), \tag{C2}$$

$$h(z) = \frac{z}{2}\int_0^1 dx \frac{1}{x(1-x) - z}\left[\frac{z}{x(1-x) - z} \ln\left(\frac{x(1-x)}{z}\right) - 1\right], \tag{C3}$$

$$F(x,y)=\frac{yf(x)-xf(y)}{y-x};\qquad G(x,y)=\frac{yg(x)-xg(y)}{y-x}, \tag{C4}$$

$$H_i^a(z)=z\int_0^1 dx\frac{(1-x)^2(x-4+x(z_{\pm,W}-z_{WH_i}^{-1}))}{x+(1-x)z_{WH_i}-x(1-x)z}\ln\left(\frac{x+(1-x)z_{WH_i}}{x(1-x)z}\right), \tag{C5}$$

$$H_i^b(z)=2z\int_0^1 dx\frac{x(1-x)^2}{x+(1-x)z_{\pm,i}-x(1-x)z}\ln\left(\frac{x+(1-x)z_{\pm,i}}{x(1-x)z}\right). \tag{C6}$$

Denoting

$$\begin{aligned}&a_x=x(1-x),\qquad b=a_x/z_a,\qquad A=x+y/z_a,\qquad B=A-a_x,\qquad B'=A-a_y,\\&C=\frac{A}{B}\ln\frac{A}{a_x}-1,\qquad C'=\frac{a_x}{B}\ln\frac{A}{a_x}-1,\qquad C''=\frac{a_y}{B'}\ln\frac{A}{a_y}-1,\end{aligned} \tag{C7}$$

the loop functions in the non-Barr-Zee-type diagrams with a W boson are [55]

$$(D_W^a)_i=-\frac{1}{2}\int_0^1 dx\int_0^{1-x}dy\frac{x}{B}\left[\frac{2C}{B}(3A-2xy)-3+\frac{2xy}{a_x}\right], \tag{C8}$$

$$(D_W^b)_i=\int_0^1 dx\int_0^{1-x}dyx\left[C'\left(\frac{3A-2xy}{B^2}+\frac{1+\frac{3x}{2a_x}(1-2y+B)}{B}\right)+\frac{3A-2xy}{2a_xB}\right], \tag{C9}$$

$$(D_W^c)_i=\int_0^1 dx\int_0^{1-x}dy\frac{x^2y}{a_x(1-y-b)}\left[\frac{b}{1-y-b}\ln\frac{1-y}{b}-1\right], \tag{C10}$$

$$(D_W^d)_i=-\frac{1}{8}\int_0^1 dx\int_0^{1-x}dy\left[\frac{1}{Bz_{WH_i}}\left(1-\frac{2Ca_x}{B}\right)+\frac{x}{B}\left(1-\frac{2CA}{B}\right)\right], \tag{C11}$$

$$(D_W^e)_i=\frac{1}{8}\int_0^1 dx\int_0^{1-x}dy\frac{x}{a_x}\times\left[\frac{C'}{B^2}(xa_x(2x-1)+Bx(3x-1)-2B^2)-2+\frac{x(2x-1)}{2B}\right]. \tag{C12}$$

The loop functions in the non-Barr-Zee-type diagrams with a Z boson are instead [55]

$$(D_Z^a)_i=\int_0^1 dx\int_0^{1-x}dy\frac{2x}{a_x}\left[1+C'\left(1+\frac{x(1-x-y)}{2B}\right)\right], \tag{C13}$$

$$(D_Z^b)_i=\int_0^1 dx\int_0^{1-x}dy\frac{x^2y}{a_x(1-y-b)}\left[\frac{b}{1-y-b}\ln\frac{1-y}{b}-1\right], \tag{C14}$$

$$(D_Z^c)_i=\int_0^1 dx\int_0^{1-x}dy\frac{1}{a_y}\left[y-x+C''\left(y-x+\frac{y^2(1-x-y)}{B'}\right)\right]. \tag{C15}$$

In the functions $(D_W^p)_i$ we have $z_a\equiv z_{WH_i}$, while in the functions $(D_Z^p)_i$ we have $z_a\equiv z_{ZH_i}$. Last, the loop function for the Weinberg operator is [58]

$$W(z)=4z^2\int_0^1 dv\int_0^1 du\frac{(1-v)(uv)^3}{[zv(1-uv)+(1-u)(1-v)]^2}. \tag{C16}$$

APPENDIX D: LOOP INTEGRATIONS FOR HIGGS PRODUCTION AND DECAY

The loop functions for Higgs production and decay are [135,136]

$$\mathcal{A}_0(x) = \frac{x - I(x)}{x^2}, \tag{D1}$$

$$\mathcal{A}_1(x) = -\frac{x + (x-1)I(x)}{x^2}, \tag{D2}$$

$$\mathcal{A}_2(x) = \frac{2x^2 + 3x + 3(2x-1)I(x)}{x^2}, \tag{D3}$$

$$\mathcal{B}_1(x) = -2\frac{I(x)}{x}, \tag{D4}$$

where

$$I(z) = \begin{cases} \arcsin^2(\sqrt{z}), & z \le 1, \\ -\frac{1}{4}\left[\ln\left(\frac{1+\sqrt{1-z^{-1}}}{1-\sqrt{1-z^{-1}}}\right) - i\pi\right]^2, & z > 1. \end{cases} \tag{D5}$$

APPENDIX E: DECAY OF HEAVY (PSEUDO)SCALARS

For heavy neutral (pseudo)scalars, we consider the decay channels $H_{2,3} \to t\bar{t}, WW, ZZ$, and ZH_1. The partial decay widths are given by

$$\Gamma_{H_i\to t\bar{t}} = \frac{3m_i m_t^2}{8\pi v^2}\left[[\mathrm{Re}(c_{t,i})]^2\left(1-\frac{4m_t^2}{m_i^2}\right)^{\frac{3}{2}} + [\mathrm{Im}(c_{t,i})]^2\left(1-\frac{4m_t^2}{m_i^2}\right)^{\frac{1}{2}}\right], \tag{E1}$$

$$\Gamma_{H_i\to WW} = \frac{m_i^3 c_{V,i}^2}{16\pi v^2}\sqrt{1-\frac{4m_W^2}{m_i^2}}\left(1-\frac{4m_W^2}{m_i^2}+\frac{12m_W^4}{m_i^4}\right), \tag{E2}$$

$$\Gamma_{H_i\to ZZ} = \frac{m_i^3 c_{V,i}^2}{32\pi v^2}\sqrt{1-\frac{4m_Z^2}{m_i^2}}\left(1-\frac{4m_Z^2}{m_i^2}+\frac{12m_Z^4}{m_i^4}\right), \tag{E3}$$

$$\Gamma_{H_i\to ZH_1} = \frac{m_i^3 c_{V,k}^2}{32\pi v^2}\mathcal{F}_{VS}\left(\frac{m_Z^2}{m_i^2}, \frac{m_i^2}{m_i^2}\right). \tag{E4}$$

Here $k \neq i$ or 1, and the functions

$$\mathcal{F}_{VS}(x,y) = (1 + x^2 + y^2 - 2x - 2y - 2xy)^{\frac{3}{2}}. \tag{E5}$$

In Scenario (b), since $H_{2,3}$ have a large mass splitting, we should also consider the $H_3 \to ZH_2$ decay. Its partial width is

$$\Gamma_{H_3\to ZH_2} = \frac{m_3^3 c_{V,1}^2}{32\pi v^2}\mathcal{F}_{VS}\left(\frac{m_Z^2}{m_3^2}, \frac{m_2^2}{m_3^2}\right). \tag{E6}$$

Thus, numerically the total decay widths $\Gamma_{2,3}$ can reach about 20 GeV if $m_{2,3} \simeq 500$ GeV, and they both dominantly decay to $t\bar{t}$. In Scenario (b), if $m_2 = 500$ GeV and $m_3 = 650$ GeV, $\mathrm{Br}_{H_3\to ZH_2}$ can reach about 10%.

The charged Higgs boson H^+ decays mainly to $t\bar{b}$ in the small-t_β region. Ignoring the coupling term proportional to m_b, we have

$$\Gamma_{H^+\to t\bar{b}} = \frac{3m_\pm}{8\pi v^2}\left(\frac{m_t}{t_\beta}\right)^2\left(1-\frac{m_t^2}{m_\pm^2}\right)^2. \tag{E7}$$

Besides this, H^+ also has subdominant decay channels, like W^+H_i [80], yielding

$$\Gamma_{H^+\to W^+H_i} = \frac{m_\pm^3(1-c_{V,i}^2)}{16\pi v^2}\mathcal{F}_{VS}\left(\frac{m_W^2}{m_\pm^2}, \frac{m_i^2}{m_\pm^2}\right). \tag{E8}$$

For $\beta = 0.76$ and $m_\pm = 600$ GeV, $\Gamma_{H^+\to t\bar{b}} = 33$ GeV, while the sum for all three neutral scalars $\sum_i \Gamma_{H^+\to W^+H_i} \lesssim 5$ GeV for $|\alpha_2| \lesssim 0.27$.

APPENDIX F: TOP-QUARK RECONSTRUCTION

For $t\bar{t}$ spin-spin correlation and polarization observables in the top-quark rest frame, it is mandatory to fully reconstruct the top (anti)quark four-momentum. In this regard, we employ the PseudoTop definition [177] widely used by the ATLAS and CMS collaborations for, e.g., validation of Monte Carlo event generators. We slightly modify the Rivet implementation of the CMS measurement of the $t\bar{t}$ differential cross section at $\sqrt{s} = 8$ TeV [194]. We minimize the quantity

$$K^2 = (M_{\tilde{t}_\ell} - m_t)^2 + (M_{j_1j_2} - m_W)^2 + (M_{\tilde{t}_h} - m_t)^2 + (M_{\tilde{p}_{H_1}} - m_{H_1})^2, \tag{F1}$$

to select the hadronic and leptonic (anti)top quarks and SM-like Higgs boson decaying into $b\bar{b}$. In Eq. (F1), m_t, m_W, and m_H are the masses of the top quark, W boson, and Higgs boson, respectively, while $\tilde{t}_\ell$ ($\tilde{t}_h$) is the momentum of the (anti)top quark constructed in the leptonic(hadronic) decays of the W boson, where $\tilde{p}_{H_1}$ is the four-momentum of the Higgs boson candidate. In the reconstruction procedure, all jets and leptons in the event are considered provided they satisfy the selection criteria, which is highlighted in Sec. V A. Validation plots for the PseudoTop reconstruction method in $t\bar{t}H_1(\to b\bar{b})$ (green) and the QCD-mediated $t\bar{t}b\bar{b}$ (red) are shown in Fig. 14.

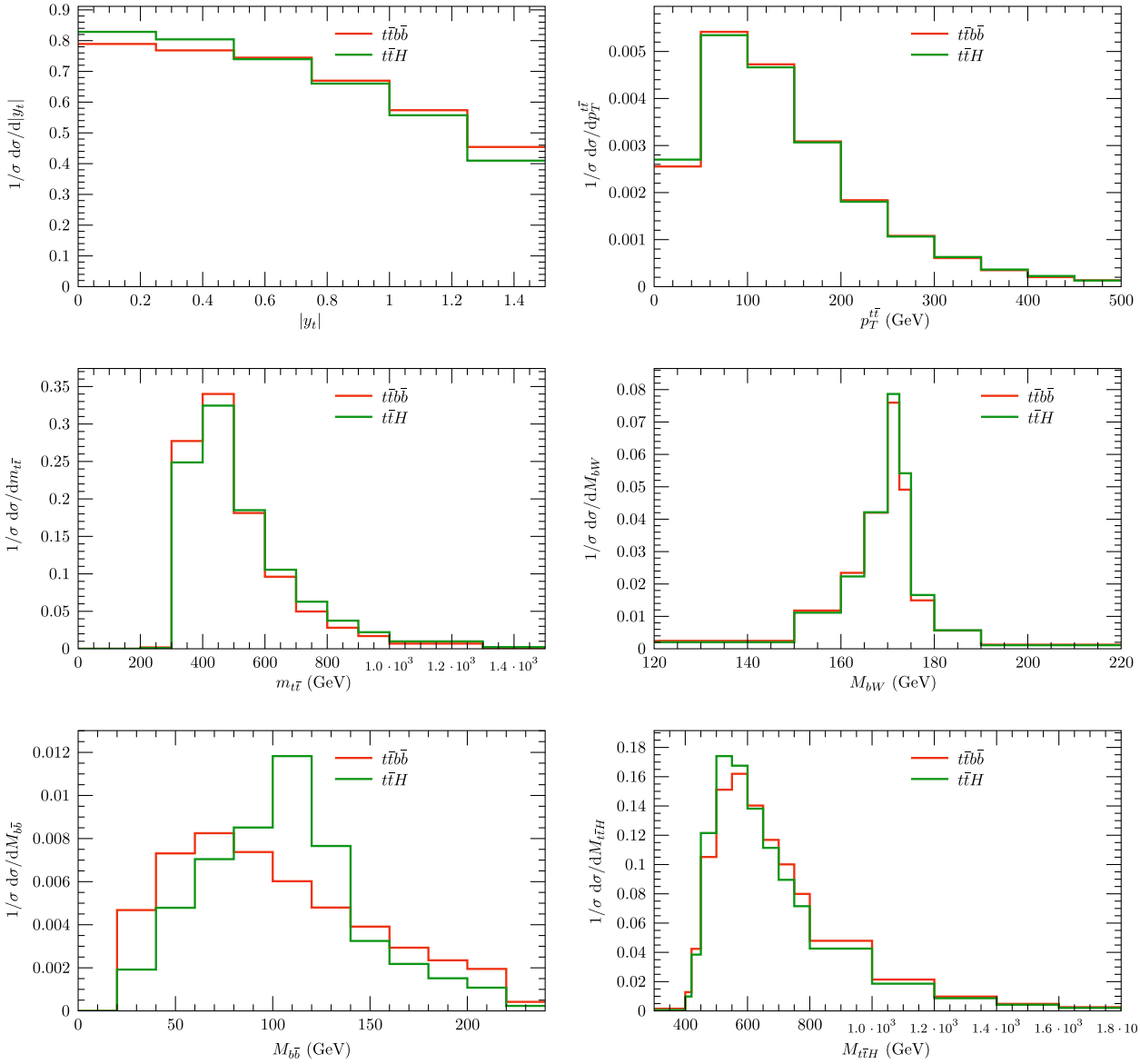

FIG. 14. Validation plots for the PseudoTop reconstruction method in $t\bar{t}H_1(\to b\bar{b})$ (green) and the QCD-mediated $t\bar{t}b\bar{b}$ (red). Here, we show the absolute value of the rapidity of the top quark (upper left), the transverse momentum of the $t\bar{t}$ system (upper right), the invariant mass of the $t\bar{t}$ system (middle left), that of the reconstructed top (anti)quark (middle right), that of the Higgs boson (lower left), and that of the $t\bar{t}H_1$ system (lower right).

[1] J. H. Christenson, J. W. Cronin, V. L. Fitch, and R. Turlay, Evidence for the 2π Decay of the K_2^0 Meson, Phys. Rev. Lett. **13**, 138 (1964).

[2] M. Tanabashi *et al.* (Particle Data Group Collaboration), Review of particle physics, Phys. Rev. D **98**, 030001 (2018).

[3] R. Aaij *et al.* (LHCb Collaboration), Observation of *CP* Violation in Charm Decays, Phys. Rev. Lett. **122**, 211803 (2019).

[4] M. Kobayashi and T. Maskawa, *CP* violation in the renormalizable theory of weak interaction, Prog. Theor. Phys. **49**, 652 (1973).

[5] A. G. Cohen, D. B. Kaplan, and A. E. Nelson, Spontaneous baryogenesis at the weak phase transition, Phys. Lett. B **263**, 86 (1991).

[6] A. G. Cohen, D. B. Kaplan, and A. E. Nelson, Progress in electroweak baryogenesis, Annu. Rev. Nucl. Part. Sci. **43**, 27 (1993).

[7] D. E. Morrissey and M. J. Ramsey-Musolf, Electroweak baryogenesis, New J. Phys. **14**, 125003 (2012).

[8] I. B. Khriplovich and S. K. Lamoreaux, *CP* violation without strangeness: Electric dipole moments of particles, atoms, and molecules (Springer, Berlin, Germany, 1997).

[9] M. Pospelov and A. Ritz, Electric dipole moments as probes of new physics, Ann. Phys. (Amsterdam) **318**, 119 (2005).

[10] J. Engel, M. J. Ramsey-Musolf, and U. van Kolck, Electric dipole moments of nucleons, nuclei, and atoms: The Standard Model and beyond, Prog. Part. Nucl. Phys. **71**, 21 (2013).

[11] N. Yamanaka, B. K. Sahoo, N. Yoshinaga, T. Sato, K. Asahi, and B. P. Das, Probing exotic phenomena at the interface of nuclear and particle physics with the electric dipole moments of diamagnetic atoms: A unique window to hadronic and semi-leptonic *CP* violation, Eur. Phys. J. A **53**, 54 (2017).

[12] M. S. Safronova, D. Budker, D. DeMille, D. F. J. Kimball, A. Derevianko, and C. W. Clark, Search for new physics with atoms and molecules, Rev. Mod. Phys. **90**, 025008 (2018).

[13] T. Chupp, P. Fierlinger, M. Ramsey-Musolf, and J. Singh, Electric dipole moments of atoms, molecules, nuclei, and particles, Rev. Mod. Phys. **91**, 015001 (2019).

[14] V. Andreev *et al.* (ACME Collaboration), Improved limit on the electric dipole moment of the electron, Nature (London) **562**, 355 (2018).

[15] C. A. Baker *et al.*, An Improved Experimental Limit on the Electric Dipole Moment of the Neutron, Phys. Rev. Lett. **97**, 131801 (2006).

[16] J. M. Pendlebury *et al.*, Revised experimental upper limit on the electric dipole moment of the neutron, Phys. Rev. D **92**, 092003 (2015).

[17] C. Abel *et al.* (nEDM Collaboration), Measurement of the Permanent Electric Dipole Moment of the Neutron, Phys. Rev. Lett. **124**, 081803 (2020).

[18] C. R. Schmidt and M. E. Peskin, A probe of *CP* Violation in Top Quark Pair Production at Hadron Supercolliders, Phys. Rev. Lett. **69**, 410 (1992).

[19] G. Mahlon and S. J. Parke, Angular correlations in top quark pair production and decay at hadron colliders, Phys. Rev. D **53**, 4886 (1996).

[20] P. S. Bhupal Dev, A. Djouadi, R. M. Godbole, M. M. Muhlleitner, and S. D. Rindani, Determining the *CP* Properties of the Higgs Boson, Phys. Rev. Lett. **100**, 051801 (2008).

[21] X.-G. He, G.-N. Li, and Y.-J. Zheng, Probing Higgs boson *CP* Properties with $t\bar{t}H$ at the LHC and the 100 TeV pp collider, Int. J. Mod. Phys. A **30**, 1550156 (2015).

[22] F. Boudjema, R. M. Godbole, D. Guadagnoli, and K. A. Mohan, Lab-frame observables for probing the top-Higgs interaction, Phys. Rev. D **92**, 015019 (2015).

[23] M. R. Buckley and D. Goncalves, Boosting the Direct *CP* Measurement of the Higgs-Top Coupling, Phys. Rev. Lett. **116**, 091801 (2016).

[24] S. Amor Dos Santos *et al.*, Probing the *CP* nature of the Higgs coupling in $t\bar{t}h$ events at the LHC, Phys. Rev. D **96**, 013004 (2017).

[25] D. Azevedo, A. Onofre, F. Filthaut, and R. Goncalo, *CP* tests of Higgs couplings in $t\bar{t}h$ semileptonic events at the LHC, Phys. Rev. D **98**, 033004 (2018).

[26] W. Bernreuther, L. Chen, and I. García, M. Perelló, R. Poeschl, F. Richard, E. Ros, and M. Vos, *CP*-violating top quark couplings at future linear e^+e^- colliders, Eur. Phys. J. C **78**, 155 (2018).

[27] K. Hagiwara, H. Yokoya, and Y.-J. Zheng, Probing the *CP* properties of top Yukawa coupling at an e^+e^- collider, J. High Energy Phys. 02 (2018) 180.

[28] K. Ma, Enhancing *CP* measurement of the Yukawa interactions of top-quark at e^-e^+ collider, Phys. Lett. B **797**, 134928 (2019).

[29] M. Cepeda *et al.* (HL/HE WG2 group Collaboration), Higgs physics at the HL-LHC and HE-LHC, CERN Yellow Rep. Monogr. **7**, 221 (2019), arXiv:1902.00134.

[30] D. A. Faroughy, J. F. Kamenik, and N. Košnik, and A. Smolkovič, Probing the *CP* nature of the top quark Yukawa at hadron colliders, J. High Energy Phys. 02 (2020) 085.

[31] Q.-H. Cao, K.-P. Xie, H. Zhang, and R. Zhang, A new observable for measuring *CP* property of top-Higgs interaction, arXiv:2008.13442.

[32] K. Desch, A. Imhof, Z. Was, and M. Worek, Probing the *CP* nature of the Higgs boson at linear colliders with tau spin correlations: The case of mixed scalar-pseudoscalar couplings, Phys. Lett. B **579**, 157 (2004).

[33] S. Berge, W. Bernreuther, and J. Ziethe, Determining the *CP* Parity of Higgs Bosons at the LHC in Their Tau Decay Channels, Phys. Rev. Lett. **100**, 171605 (2008).

[34] R. Harnik, A. Martin, T. Okui, R. Primulando, and F. Yu, Measuring *CP* violation in $h \to \tau^+\tau^-$ at colliders, Phys. Rev. D **88**, 076009 (2013).

[35] S. Berge, W. Bernreuther, and H. Spiesberger, Higgs *CP* properties using the τ decay modes at the ILC, Phys. Lett. B **727**, 488 (2013).

[36] S. Berge, W. Bernreuther, and S. Kirchner, Determination of the Higgs *CP*-mixing angle in the tau decay channels at the LHC including the Drell–Yan background, Eur. Phys. J. C **74**, 3164 (2014).

[37] S. Berge, W. Bernreuther, and S. Kirchner, Prospects of constraining the Higgs boson's *CP* nature in the tau decay channel at the LHC, Phys. Rev. D **92**, 096012 (2015).

[38] A. Askew, P. Jaiswal, T. Okui, H. B. Prosper, and N. Sato, Prospect for measuring the *CP* phase in the $h\tau\tau$ coupling at the LHC, Phys. Rev. D **91**, 075014 (2015).

[39] K. Hagiwara, K. Ma, and S. Mori, Probing *CP* Violation in $h \to \tau^-\tau^+$ at the LHC, Phys. Rev. Lett. **118**, 171802 (2017).

[40] R. Józefowicz, E. Richter-Was, and Z. Was, Potential for optimizing the Higgs boson *CP* measurement in $H \to \tau\tau$ decays at the LHC including machine learning techniques, Phys. Rev. D **94**, 093001 (2016).

[41] G. Aad *et al.* (ATLAS Collaboration), Observation of a new particle in the search for the Standard Model Higgs boson with the ATLAS detector at the LHC, Phys. Lett. B **716**, 1 (2012).

[42] S. Chatrchyan *et al.* (CMS Collaboration), Observation of a new boson at a mass of 125 GeV with the CMS Experiment at the LHC, Phys. Lett. B **716**, 30 (2012).

[43] G. Aad *et al.* (ATLAS and CMS Collaborations), Combined Measurement of the Higgs Boson Mass in pp Collisions at $\sqrt{s} = 7$ and 8 TeV with the ATLAS and CMS Experiments, Phys. Rev. Lett. **114**, 191803 (2015).
[44] G. Li, Y.-n. Mao, C. Zhang, and S.-h. Zhu, Testing *CP* violation in the scalar sector at future e^+e^- colliders, Phys. Rev. D **95**, 035015 (2017).
[45] Y.-n. Mao, Spontaneous *CP*-violation in the simplest little Higgs model and its future collider tests: The scalar sector, Phys. Rev. D **97**, 075031 (2018).
[46] Y.-n. Mao, Spontaneous *CP*-violation in the simplest little Higgs model, Proc. Sci., ICHEP2018 (**2019**) 003.
[47] L. Bento, G. C. Branco, and P. A. Parada, A minimal model with natural suppression of strong *CP* violation, Phys. Lett. B **267**, 95 (1991).
[48] T. D. Lee, A theory of spontaneous T violation, Phys. Rev. D **8**, 1226 (1973).
[49] T. D. Lee, *CP* nonconservation and spontaneous symmetry breaking, Phys. Rep. **9**, 143 (1974).
[50] H. Georgi, A model of soft *CP* violation, Hadronic J. **1**, 155 (1978).
[51] G. C. Branco, P. M. Ferreira, L. Lavoura, M. N. Rebelo, M. Sher, and J. P. Silva, Theory and phenomenology of two-Higgs-doublet models, Phys. Rep. **516**, 1 (2012).
[52] S. Weinberg, Gauge Theory of *CP* Violation, Phys. Rev. Lett. **37**, 657 (1976).
[53] S. M. Barr and A. Zee, Electric Dipole Moment of the Electron and of the Neutron, Phys. Rev. Lett. **65**, 21 (1990).
[54] D. Chang, W.-Y. Keung, and T. C. Yuan, Two loop bosonic contribution to the electron electric dipole moment, Phys. Rev. D **43**, R14 (1991).
[55] R. G. Leigh, S. Paban, and R. M. Xu, Electric dipole moment of electron, Nucl. Phys. **B352**, 45 (1991).
[56] M. Jung and A. Pich, Electric dipole moments in two-Higgs-doublet models, J. High Energy Phys. 04 (2014) 076.
[57] T. Abe, J. Hisano, T. Kitahara, and K. Tobioka, Gauge invariant Barr-Zee type contributions to fermionic EDMs in the two-Higgs doublet models, J. High Energy Phys. 01 (2014) 106.
[58] J. Brod, U. Haisch, and J. Zupan, Constraints on *CP*-violating Higgs couplings to the third generation, J. High Energy Phys. 11 (2013) 180.
[59] K. Cheung, J. S. Lee, E. Senaha, and P.-Y. Tseng, Confronting Higgcision with electric dipole moments, J. High Energy Phys. 06 (2014) 149.
[60] C.-Y. Chen, S. Dawson, and Y. Zhang, Complementarity of LHC and EDMs for Exploring Higgs *CP* Violation, J. High Energy Phys. 06 (2015) 056.
[61] V. Keus, S. F. King, S. Moretti, and K. Yagyu, *CP* Violating Two-Higgs-Doublet Model: Constraints and LHC Predictions, J. High Energy Phys. 04 (2016) 048.
[62] D. Fontes and J. C. Romão, R. Santos, and J. P. Silva, Large pseudoscalar Yukawa couplings in the complex 2HDM, J. High Energy Phys. 06 (2015) 060.
[63] W. Altmannshofer, J. Brod, and M. Schmaltz, Experimental constraints on the coupling of the Higgs boson to electrons, J. High Energy Phys. 05 (2015) 125.
[64] C.-Y. Chen, H.-L. Li, and M. Ramsey-Musolf, *CP*-violation in the two Higgs doublet model: From the LHC to EDMs, Phys. Rev. D **97**, 015020 (2018).
[65] D. Fontes and M. Mühlleitner, J. C. Romão, R. Santos, J. P. Silva, and J. Wittbrodt, The C2HDM revisited, J. High Energy Phys. 02 (2018) 073.
[66] E. J. Chun, J. Kim, and T. Mondal, Electron EDM and Muon anomalous magnetic moment in two-Higgs-doublet models, J. High Energy Phys. 12 (2019) 068.
[67] S. Inoue, M. J. Ramsey-Musolf, and Y. Zhang, *CP*-violating phenomenology of flavor conserving two Higgs doublet models, Phys. Rev. D **89**, 115023 (2014).
[68] Y.-n. Mao and S.-h. Zhu, Lightness of Higgs boson and spontaneous *CP* violation in the Lee model, Phys. Rev. D **90**, 115024 (2014).
[69] L. Bian, T. Liu, and J. Shu, Cancellations Between Two-Loop Contributions to the Electron Electric Dipole Moment with a *CP*-Violating Higgs Sector, Phys. Rev. Lett. **115**, 021801 (2015).
[70] Y.-n. Mao and S.-h. Zhu, Lightness of a Higgs boson and spontaneous *CP*-violation in the Lee Model: An alternative scenario, Phys. Rev. D **94**, 055008 (2016).
[71] L. Bian and N. Chen, Higgs pair productions in the *CP*-violating two-Higgs-doublet model, J. High Energy Phys. 09 (2016) 069.
[72] L. Bian and N. Chen, Cancellation mechanism in the predictions of electric dipole moments, Phys. Rev. D **95**, 115029 (2017).
[73] D. Egana-Ugrinovic and S. Thomas, Higgs boson contributions to the electron electric dipole moment, arXiv:1810.08631.
[74] K. Fuyuto, W.-S. Hou, and E. Senaha, Cancellation mechanism for the electron electric dipole moment connected with the baryon asymmetry of the Universe, Phys. Rev. D **101**, 011901 (2020).
[75] J. Shu and Y. Zhang, Impact of a *CP* Violating Higgs Sector: From LHC to Baryogenesis, Phys. Rev. Lett. **111**, 091801 (2013).
[76] G. W. S. Hou, ElectroWeak baryogenesis via top transport, Proc. Sci., EPS-HEP2017 (**2017**) 444.
[77] K. Fuyuto, W.-S. Hou, and E. Senaha, Electroweak baryogenesis driven by extra top Yukawa couplings, Phys. Lett. B **776**, 402 (2018).
[78] A. W. El Kaffas, W. Khater, O. M. Ogreid, and P. Osland, Consistency of the two Higgs doublet model and *CP* violation in top production at the LHC, Nucl. Phys. **B775**, 45 (2007).
[79] P. Osland, P. N. Pandita, and L. Selbuz, Trilinear Higgs couplings in the two Higgs doublet model with *CP* violation, Phys. Rev. D **78**, 015003 (2008).
[80] A. Arhrib, E. Christova, H. Eberl, and E. Ginina, *CP* violation in charged Higgs production and decays in the complex two Higgs doublet model, J. High Energy Phys. 04 (2011) 089.
[81] A. Abdesselam *et al.* (Belle Collaboration), Measurement of the inclusive $B \to X_{s+d}\gamma$ branching fraction, photon energy spectrum and HQE parameters, in *Proceedings, 38th International Conference on High Energy Physics (ICHEP 2016): Chicago, IL, USA, 2016* (2016), https://inspirehep.net/literature/1479946.

[82] T. Hermann, M. Misiak, and M. Steinhauser, $\bar{B} \to X_s\gamma$ in the two Higgs doublet model up to next-to-next-to-leading order in QCD, J. High Energy Phys. 11 (2012) 036.

[83] M. Misiak *et al.*, Updated NNLO QCD Predictions for the Weak Radiative B-Meson Decays, Phys. Rev. Lett. **114**, 221801 (2015).

[84] M. Misiak and M. Steinhauser, Weak radiative decays of the B meson and bounds on $M_{H^\pm}$ in the two-Higgs-doublet model, Eur. Phys. J. C **77**, 201 (2017).

[85] M. E. Peskin and T. Takeuchi, A New Constraint on a Strongly Interacting Higgs Sector, Phys. Rev. Lett. **65**, 964 (1990).

[86] M. E. Peskin and T. Takeuchi, Estimation of oblique electroweak corrections, Phys. Rev. D **46**, 381 (1992).

[87] J. de Blas, M. Ciuchini, E. Franco, S. Mishima, M. Pierini, L. Reina, and L. Silvestrini, Electroweak precision observables and Higgs-boson signal strengths in the Standard Model and beyond: Present and future, J. High Energy Phys. 12 (2016) 135.

[88] W. Grimus, L. Lavoura, O. M. Ogreid, and P. Osland, A precision constraint on multi-Higgs-doublet models, J. Phys. G **35**, 075001 (2008).

[89] W. Grimus, L. Lavoura, O. M. Ogreid, and P. Osland, The oblique parameters in multi-Higgs-doublet models, Nucl. Phys. **B801**, 81 (2008).

[90] H. E. Haber and D. O'Neil, Basis-independent methods for the two-Higgs-doublet model III: The *CP*-conserving limit, custodial symmetry, and the oblique parameters S, T, U, Phys. Rev. D **83**, 055017 (2011).

[91] T. Chupp and M. Ramsey-Musolf, Electric dipole moments: A global analysis, Phys. Rev. C **91**, 035502 (2015).

[92] C. Cesarotti, Q. Lu, Y. Nakai, A. Parikh, and M. Reece, Interpreting the electron EDM constraint, J. High Energy Phys. 05 (2019) 059.

[93] N. Yamanaka, Analysis of the electric dipole moment in the R-parity violating supersymmetric Standard Model, Ph.D. thesis, Research Center for Nuclear Physics of Osaka University, 2013.

[94] A. Crivellin, A. Kokulu, and C. Greub, Flavor-phenomenology of two-Higgs-doublet models with generic Yukawa structure, Phys. Rev. D **87**, 094031 (2013).

[95] S. M. Barr, Measurable T and P Odd Electron-Nucleon Interactions from Higgs Boson Exchange, Phys. Rev. Lett. **68**, 1822 (1992).

[96] W. Dekens, J. de Vries, M. Jung, and K. K. Vos, The phenomenology of electric dipole moments in models of scalar leptoquarks, J. High Energy Phys. 01 (2019) 069.

[97] K. Cheung, W.-Y. Keung, Y.-n. Mao, and C. Zhang, Constraining *CP*-violating electron-gluonic operators, J. High Energy Phys. 07 (2019) 074.

[98] X.-D. Ji, A QCD Analysis of the Mass Structure of the Nucleon, Phys. Rev. Lett. **74**, 1071 (1995).

[99] H.-Y. Cheng and C.-W. Chiang, Revisiting scalar and pseudoscalar couplings with nucleons, J. High Energy Phys. 07 (2012) 009.

[100] R. J. Hill and M. P. Solon, Standard Model anatomy of WIMP dark matter direct detection II: QCD analysis and hadronic matrix elements, Phys. Rev. D **91**, 043505 (2015).

[101] Y.-B. Yang, A. Alexandru, T. Draper, J. Liang, and K.-F. Liu (xQCD Collaboration), πN and strangeness sigma terms at the physical point with chiral fermions, Phys. Rev. D **94**, 054503 (2016).

[102] K. Yanase, N. Yoshinaga, K. Higashiyama, and N. Yamanaka, Electric dipole moment of ^{199}Hg atom from *P*, *CP*-odd electron-nucleon interaction, Phys. Rev. D **99**, 075021 (2019).

[103] N. Yamanaka, S. Hashimoto, T. Kaneko, and H. Ohki (JLQCD Collaboration), Nucleon charges with dynamical overlap fermions, Phys. Rev. D **98**, 054516 (2018).

[104] S. Weinberg, Larger Higgs Exchange Terms in the Neutron Electric Dipole Moment, Phys. Rev. Lett. **63**, 2333 (1989).

[105] D. A. Dicus, Neutron electric dipole moment from charged Higgs exchange, Phys. Rev. D **41**, 999 (1990).

[106] E. Braaten, C.-S. Li, and T.-C. Yuan, The Evolution of Weinberg's Gluonic *CP* Violation Operator, Phys. Rev. Lett. **64**, 1709 (1990).

[107] G. Degrassi, E. Franco, S. Marchetti, and L. Silvestrini, QCD corrections to the electric dipole moment of the neutron in the MSSM, J. High Energy Phys. 11 (2005) 044.

[108] S. Aoki *et al.*, Review of lattice results concerning low-energy particle physics, Eur. Phys. J. C **77**, 112 (2017).

[109] S. Aoki *et al.* (Flavour Lattice Averaging Group Collaboration), FLAG review 2019, Eur. Phys. J. C **80**, 113 (2020).

[110] J. Hisano, J. Y. Lee, N. Nagata, and Y. Shimizu, Reevaluation of neutron electric dipole moment with QCD sum rules, Phys. Rev. D **85**, 114044 (2012).

[111] D. A. Demir, M. Pospelov, and A. Ritz, Hadronic EDMs, the Weinberg operator, and light gluinos, Phys. Rev. D **67**, 015007 (2003).

[112] U. Haisch and A. Hala, Sum rules for *CP*-violating operators of Weinberg type, J. High Energy Phys. 11 (2019) 154.

[113] B. Yoon, T. Bhattacharya, V. Cirigliano, and R. Gupta, Neutron electric dipole moments with clover fermions, Proc. Sci., LATTICE2019 (**2019**) 243 [arXiv:2003.05390].

[114] C. McNeile, A. Bazavov, C. T. H. Davies, R. J. Dowdall, K. Hornbostel, G. P. Lepage, and H. D. Trottier, Direct determination of the strange and light quark condensates from full lattice QCD, Phys. Rev. D **87**, 034503 (2013).

[115] C. A. Baker *et al.*, CryoEDM: A cryogenic experiment to measure the neutron electric dipole moment, J. Phys. Conf. Ser. **251**, 012055 (2010).

[116] R. Picker, How the minuscule can contribute to the big picture: The neutron electric dipole moment project at TRIUMF, J. Phys. Soc. Conf. Proc. **13**, 010005 (2017).

[117] N. Ayres, Data and systematic error analysis for the neutron electric dipole moment experiment at the Paul Scherrer Institute and search for axionlike dark matter, Ph.D. thesis, Sussex University, 2018-12-14.

[118] C. Abel *et al.*, The n2EDM experiment at the Paul Scherrer Institute, EPJ Web Conf. **219**, 02002 (2019).

[119] M. Ahmed *et al.* (nEDM Collaboration), A new cryogenic apparatus to search for the neutron electric dipole moment, J. Instrum. **14**, P11017 (2019).

[120] B. Graner, Y. Chen, E. Lindahl, and B. Heckel, Reduced Limit on the Permanent Electric Dipole Moment of Hg199, Phys. Rev. Lett. **116**, 161601 (2016).

[121] M. Bishof *et al.*, Improved limit on the ^{225}Ra electric dipole moment, Phys. Rev. C **94**, 025501 (2016).

[122] N. Sachdeva *et al.*, New Limit on the Permanent Electric Dipole Moment of ^{129}Xe Using ^{3}He Comagnetometry and SQUID Detection, Phys. Rev. Lett. **123**, 143003 (2019).

[123] M. Pospelov, Best values for the *CP* odd meson nucleon couplings from supersymmetry, Phys. Lett. B **530**, 123 (2002).

[124] *Handbook of LHC Higgs Cross Sections: 1. Inclusive Observables*, edited by S. Dittmaier, C. Mariotti, G. Passarino and R. Tanaka (LHC Higgs Cross Section Working Group) (CERN, Geneva, 2011), Report No. CERN-2011-002.

[125] S. Dittmaier *et al.*, Handbook of LHC Higgs cross sections: 2. Differential distributions, arXiv:1201.3084.

[126] J. R. Andersen *et al.* (LHC Higgs Cross Section Working Group Collaboration), Handbook of LHC Higgs cross sections: 3. Higgs properties, arXiv:1307.1347.

[127] D. de Florian *et al.* (LHC Higgs Cross Section Working Group Collaboration), Handbook of LHC Higgs Cross Sections: 4. Deciphering the Nature of the Higgs Sector, arXiv:1610.07922.

[128] G. Aad *et al.* (ATLAS Collaboration), Combined measurements of Higgs boson production and decay using up to 80 fb^{-1} of proton-proton collision data at $\sqrt{s} = 13$ TeV collected with the ATLAS experiment, Phys. Rev. D **101**, 012002 (2020).

[129] L. Cadamuro (ATLAS and CMS Collaborations), Higgs boson couplings and properties, Proc. Sci., LHCP2019 (**2019**) 101.

[130] ATLAS Collaboration, Measurement of Higgs boson production in association with a $t\bar{t}$ pair in the diphoton decay channel using 139 fb^{-1} of LHC data collected at $\sqrt{s} = 13$ TeV by the ATLAS experiment, Technical Report No. ATLAS-CONF-2019-004, CERN, Geneva, 2019.

[131] M. Aaboud *et al.* (ATLAS Collaboration), Observation of Higgs boson production in association with a top quark pair at the LHC with the ATLAS detector, Phys. Lett. B **784**, 173 (2018).

[132] CMS Collaboration, Combined Higgs boson production and decay measurements with up to 137 fb-1 of proton-proton collision data at $\sqrt{s} = 13$ TeV, Technical Report No. CMS-PAS-HIG-19-005, CERN, Geneva, 2020.

[133] A. M. Sirunyan *et al.* (CMS Collaboration), Combined measurements of Higgs boson couplings in proton-proton collisions at $\sqrt{s} = 13$ TeV, Eur. Phys. J. C **79**, 421 (2019).

[134] A. M. Sirunyan *et al.* (CMS Collaboration), Observation of Higgs Boson Decay to Bottom Quarks, Phys. Rev. Lett. **121**, 121801 (2018).

[135] A. Djouadi, The anatomy of electro-weak symmetry breaking. I: The Higgs boson in the standard model, Phys. Rep. **457**, 1 (2008).

[136] A. Djouadi, The anatomy of electro-weak symmetry breaking. II. The Higgs bosons in the minimal supersymmetric model, Phys. Rep. **459**, 1 (2008).

[137] H.-L. Li, P.-C. Lu, Z.-G. Si, and Y. Wang, Associated production of Higgs boson and $t\bar{t}$ at LHC, Chin. Phys. C **40**, 063102 (2016).

[138] ATLAS Collaboration, Search for heavy ZZ resonances in the $\ell^+\ell^-\ell^+\ell^-$ and $\ell^+\ell^-\nu\bar{\nu}$ final states using proton–proton collisions at $\sqrt{s} = 13$ TeV with the ATLAS detector, Technical Report No. ATLAS-CONF-2017-058, CERN, Geneva, 2017.

[139] A. D. Martin, W. J. Stirling, R. S. Thorne, and G. Watt, Parton distributions for the LHC, Eur. Phys. J. C **63**, 189 (2009).

[140] E. W. N. Glover and J. J. van der Bij, Z boson pair production via gluon fusion, Nucl. Phys. **B321**, 561 (1989).

[141] A. Pilaftsis, Resonant *CP* violation induced by particle mixing in transition amplitudes, Nucl. Phys. **B504**, 61 (1997).

[142] M. Berger and C. Kao, Production of Z boson pairs via gluon fusion in the minimal supersymmetric model, Phys. Rev. D **59**, 075004 (1999).

[143] N. Kauer, Signal-background interference in $gg \to H \to VV$, Proc. Sci., RADCOR2011 (**2011**) 027.

[144] M. Aaboud *et al.* (ATLAS Collaboration), Search for heavy particles decaying into top-quark pairs using lepton-plus-jets events in proton-proton collisions at $\sqrt{s} = 13$ TeV with the ATLAS detector, Eur. Phys. J. C **78**, 565 (2018).

[145] D. Dicus, A. Stange, and S. Willenbrock, Higgs decay to top quarks at hadron colliders, Phys. Lett. B **333**, 126 (1994).

[146] A. Djouadi, J. Ellis, A. Popov, and J. Quevillon, Interference effects in $t\bar{t}$ production at the LHC as a window on new physics, J. High Energy Phys. 03 (2019) 119.

[147] S. Moretti and D. A. Ross, On the top-antitop invariant mass spectrum at the LHC from a Higgs boson signal perspective, Phys. Lett. B **712**, 245 (2012).

[148] M. Aaboud *et al.* (ATLAS Collaboration), Search for Heavy Higgs Bosons A/H Decaying to a Top Quark Pair in pp Collisions at $\sqrt{s} = 8$ TeV with the ATLAS Detector, Phys. Rev. Lett. **119**, 191803 (2017).

[149] A. M. Sirunyan *et al.* (CMS Collaboration), Search for heavy Higgs bosons decaying to a top quark pair in proton-proton collisions at $\sqrt{s} = 13$ TeV, J. High Energy Phys. 04 (2020) 171.

[150] CMS Collaboration, Search for standard model production of four top quarks in final states with same-sign and multiple leptons in proton-proton collisions at $\sqrt{s} = 13$ TeV, Technical Report No. CMS-PAS-TOP-18-003, CERN, Geneva, 2019.

[151] G. Aad *et al.* (ATLAS Collaboration), Evidence for $t\bar{t}t\bar{t}$ production in the multilepton final state in proton-proton collisions at $\sqrt{s} = 13$ TeV with the ATLAS detector, arXiv:2007.14858.

[152] Q.-H. Cao, S.-L. Chen, Y. Liu, R. Zhang, and Y. Zhang, Limiting top quark-Higgs boson interaction and Higgs-boson width from multitop productions, Phys. Rev. D **99**, 113003 (2019).

[153] J. Alwall, M. Herquet, F. Maltoni, O. Mattelaer, and T. Stelzer, MadGraph5: Going beyond, J. High Energy Phys. 06 (2011) 128.

[154] J. Alwall, R. Frederix, S. Frixione, V. Hirschi, F. Maltoni, O. Mattelaer, H.-S. Shao, T. Stelzer, P. Torrielli, and M. Zaro, The automated computation of tree-level and next-to-leading order differential cross sections, and their matching to parton shower simulations, J. High Energy Phys. 07 (2014) 079.

[155] A. M. Sirunyan *et al.* (CMS Collaboration), Search for a charged Higgs boson decaying into top and bottom quarks in events with electrons or muons in proton-proton collisions at $\sqrt{s} = 13$ TeV, J. High Energy Phys. 01 (2020) 096.

[156] CMS Collaboration, Search for charged Higgs bosons decaying into top and a bottom quark in the fully hadronic final state at 13 TeV, Technical Report No. CMS-PAS-HIG-18-015, CERN, Geneva, 2019.

[157] A. Arhrib, D. Azevedo, R. Benbrik, H. Harouiz, S. Moretti, R. Patrick *et al.*, Signal versus background interference in $H^+ \to t\bar{b}$ signals for MSSM benchmark scenarios, arXiv:1905.02635.

[158] CMS Collaboration, Analysis of the *CP* structure of the Yukawa coupling between the Higgs boson and τ leptons in proton-proton collisions at $\sqrt{s} = 13$ TeV, Technical Report No. CMS-PAS-HIG-20-006, CERN, Geneva, 2020.

[159] C. Degrande, C. Duhr, B. Fuks, D. Grellscheid, O. Mattelaer, and T. Reiter, UFO—The Universal FeynRules output, Comput. Phys. Commun. **183**, 1201 (2012).

[160] C. Degrande, Automatic evaluation of UV and R2 terms for beyond the Standard Model Lagrangians: A proof-of-principle, Comput. Phys. Commun. **197**, 239 (2015).

[161] L. A. Harland-Lang, A. D. Martin, P. Motylinski, and R. S. Thorne, Parton distributions in the LHC era: MMHT 2014 PDFs, Eur. Phys. J. C **75**, 204 (2015).

[162] A. Kalogeropoulos and J. Alwall, The SysCalc code: A tool to derive theoretical systematic uncertainties, arXiv:1801.08401.

[163] P. Artoisenet, R. Frederix, O. Mattelaer, and R. Rietkerk, Automatic spin-entangled decays of heavy resonances in Monte Carlo simulations, J. High Energy Phys. 03 (2013) 015.

[164] T. Sjöstrand, S. Ask, J. R. Christiansen, R. Corke, N. Desai, P. Ilten, S. Mrenna, S. Prestel, C. O. Rasmussen, and P. Z. Skands, An introduction to PYTHIA 8.2, Comput. Phys. Commun. **191**, 159 (2015).

[165] M. Dobbs and J. B. Hansen, The HepMC C++ Monte Carlo event record for High Energy Physics, Comput. Phys. Commun. **134**, 41 (2001).

[166] A. Buckley, J. Butterworth, L. Lönnblad, D. Grellscheid, H. Hoeth, J. Monk, H. Schulz, and F. Siegert, Rivet user manual, Comput. Phys. Commun. **184**, 2803 (2013).

[167] M. Cacciari, G. P. Salam, and G. Soyez, The anti-k(t) jet clustering algorithm, J. High Energy Phys. 04 (2008) 063.

[168] M. Cacciari, G. P. Salam, and G. Soyez, FastJet User Manual, Eur. Phys. J. C **72**, 1896 (2012).

[169] G. Corcella, I. G. Knowles, G. Marchesini, S. Moretti, K. Odagiri, P. Richardson *et al.*, HERWIG 6.5 release note, arXiv:hep-ph/0210213.

[170] G. Corcella, I. G. Knowles, G. Marchesini, S. Moretti, K. Odagiri, P. Richardson *et al.*, HERWIG 6.4 release note, arXiv:hep-ph/0201201.

[171] G. Corcella, I. G. Knowles, G. Marchesini, S. Moretti, K. Odagiri, P. Richardson *et al.*, HERWIG 6.3 release note, arXiv:hep-ph/0107071.

[172] G. Corcella, I. G. Knowles, G. Marchesini, S. Moretti, K. Odagiri, P. Richardson, M. H. Seymour, and B. R. Webber, HERWIG 6: An event generator for hadron emission reactions with interfering gluons (including supersymmetric processes), J. High Energy Phys. 01 (2001) 010.

[173] M. Wobisch and T. Wengler, Hadronization corrections to jet cross-sections in deep inelastic scattering, in Monte Carlo generators for HERA physics, in *Proceedings, Workshop, Hamburg, Germany, 1998–1999* (1998), pp. 270–279, https://inspirehep.net/literature/484872.

[174] Y. L. Dokshitzer, G. D. Leder, S. Moretti, and B. R. Webber, Better jet clustering algorithms, J. High Energy Phys. 08 (1997) 001.

[175] M. Cacciari and G. P. Salam, Pileup subtraction using jet areas, Phys. Lett. B **659**, 119 (2008).

[176] M. Cacciari, G. P. Salam, and G. Soyez, The catchment area of jets, J. High Energy Phys. 04 (2008) 005.

[177] CMS Collaboration, Object definitions for top quark analyses at the particle level, Technical Report Nos. CMS-NOTE-2017-004, CERN-CMS-NOTE-2017-004, CERN, Geneva, 2017.

[178] J. Pumplin, D. Stump, R. Brock, D. Casey, J. Huston, J. Kalk, H. L. Lai, and W. K. Tung, Uncertainties of predictions from parton distribution functions. 2. The Hessian method, Phys. Rev. D **65**, 014013 (2001).

[179] W. Bernreuther and Z.-G. Si, Top quark spin correlations and polarization at the LHC: Standard model predictions and effects of anomalous top chromo moments, Phys. Lett. B **725**, 115 (2013); **744**, 413(E) (2015).

[180] M. Aaboud *et al.* (ATLAS Collaboration), Measurements of top quark spin observables in $t\bar{t}$ events using dilepton final states in $\sqrt{s} = 8$ TeV pp collisions with the ATLAS detector, J. High Energy Phys. 03 (2017) 113.

[181] A. M. Sirunyan *et al.* (CMS Collaboration), Measurement of the top quark polarization and $t\bar{t}$ spin correlations using dilepton final states in proton-proton collisions at $\sqrt{s} = 13$ TeV, Phys. Rev. D **100**, 072002 (2019).

[182] ATLAS Collaboration, Measurements of top-quark pair spin correlations in the $e\mu$ channel at $\sqrt{s} = 13$ TeV using pp collisions in the ATLAS detector, Technical Report No. ATLAS-CONF-2018-027, CERN, Geneva, 2018.

[183] CMS Collaboration, Measurements of differential cross sections for $t\bar{t}$ production in proton-proton collisions at $\sqrt{s} = 13$ TeV using events containing two leptons, Technical Report No. CMS-PAS-TOP-17-014, CERN, Geneva, 2018.

[184] R. M. Godbole, L. Hartgring, I. Niessen, and C. D. White, Top polarisation studies in $H^- t$ and Wt production, J. High Energy Phys. 01 (2012) 011.

[185] S. D. Rindani and P. Sharma, Probing anomalous tbW couplings in single-top production using top polarization at the large hadron collider, J. High Energy Phys. 11 (2011) 082.

[186] A. Prasath V, R. M. Godbole, and S. D. Rindani, Longitudinal top polarisation measurement and anomalous Wtb coupling, Eur. Phys. J. C **75**, 402 (2015).

[187] R. M. Godbole, G. Mendiratta, and S. Rindani, Looking for bSM physics using top-quark polarization and decay-lepton kinematic asymmetries, Phys. Rev. D **92**, 094013 (2015).

[188] A. Jueid, Probing anomalous Wtb couplings at the LHC in single t-channel top quark production, Phys. Rev. D **98**, 053006 (2018).

[189] A. Arhrib, A. Jueid, and S. Moretti, Top quark polarization as a probe of charged Higgs bosons, Phys. Rev. D **98**, 115006 (2018).

[190] R. Godbole, M. Guchait, C. K. Khosa, J. Lahiri, S. Sharma, and A. H. Vijay, Boosted top quark polarization, Phys. Rev. D **100**, 056010 (2019).

[191] A. Arhrib, A. Jueid, and S. Moretti, Searching for heavy charged Higgs bosons through top quark polarization, Int. J. Mod. Phys. A **35**, 2041011 (2020).

[192] S. Chatterjee, R. Godbole, and T. S. Roy, Jets with electrons from boosted top quarks, J. High Energy Phys. 01 (2020) 170.

[193] J. Ren, L. Wu, and J. M. Yang, Unveiling CP property of top-Higgs coupling with graph neural networks at the LHC, Phys. Lett. B **802**, 135198 (2020).

[194] V. Khachatryan *et al.* (CMS Collaboration), Measurement of the differential cross section for top quark pair production in pp collisions at $\sqrt{s} = 8$ TeV, Eur. Phys. J. C **75**, 542 (2015).